March 2019

DIRECT PRINTING OF CONDUCTIVE INKS FOR ORGANIC ELECTRONICS AND WEARABLE MICROFLUIDICS

Aditi Naik
University of Massachusetts Amherst

DIRECT PRINTING OF CONDUCTIVE INKS FOR ORGANIC ELECTRONICS AND WEARABLE MICROFLUIDICS

A Dissertation Presented

by

ADITI R. NAIK

Submitted to the Graduate School of the
University of Massachusetts Amherst in partial fulfillment
of the requirements for the degree of

DOCTOR OF PHILOSOPHY

February 2019

Polymer Science & Engineering

DIRECT PRINTING OF CONDUCTIVE INKS FOR ORGANIC ELECTRONICS AND WEARABLE MICROFLUIDICS

A Dissertation Presented

by

ADITI R. NAIK

Approved as to style and content by:

_____
James J. Watkins, Chair

_____
Sarah L. Perry, Member

_____
Kenneth R. Carter, Member

_____
E. Bryan Coughlin, Department Head
Polymer Science & Engineering

ACKNOWLEDGMENTS

There are several individuals whom I would like to thank for their contributions to the work discussed in this dissertation. This research has not been an individual pursuit, but instead a result of the cooperation, creativity, and friendship of numerous people.

First, I would like to show my greatest appreciation to my advisor, Professor James Watkins, for his guidance on research projects, advice on career pathways, and encouragement over the years. Specially, I am grateful for the opportunity to grow as a researcher and scientist, while working in the areas of point-of-care devices, flexible electronics, and nanotechnology. In fact, these were the very topics that I wrote about in my admissions essay, and I feel fortunate to have contributed to this field of research. I am also very thankful for the opportunity to travel internationally, present at various conferences, and collaborate with several industrial partners. Furthermore, I would like to acknowledge the generous funding provided by Professor Watkins for my graduate studies through the National Foundation for Science, Center for Hierarchical Manufacturing, and Nano-Bio Manufacturing Consortium.

Similarly, I would like to express my gratitude to my thesis committee members. I am most grateful to Professor Alejandro Briseño for his sincere encouragement and mentorship, particularly for his help with laboratory work during my first three years and his guidance with academic writing over the past two years. His enthusiasm for research is truly contagious, and he has assisted me immensely with my experimental design, data collection, and material characterization. I would particularly like to thank Professor Sarah Perry for her attentiveness as a committee member and her expertise in microfluidic systems. I have learned a great deal of practical and experimental knowledge

from her microfluidics course, where I also appreciated the chance to present guest lectures. Lastly, I would like to thank Professor Kenneth Carter for his insightful comments, good humor, and welcoming attitude. It has been an honor and delight to have him on my committee.

I would also like to acknowledge my previous research advisors who inspired me to pursue a graduate degree. First and foremost, I would like to thank Professor Margaret Frey at Cornell for accepting me into her research group, introducing me to polymeric materials, and encouraging me to present my work at all opportunities. I can sincerely say that without her positive influence during my undergraduate years, I would not have chosen a career in research. Next, I am very grateful to Professor Shane Catledge from the University of Alabama at Birmingham for his mentorship during my REU summer. It was through his guidance that I learned of the importance of point-of-care devices. Lastly, I would like to thank Professor Jan Lagerwall for hosting me at the University of Luxembourg for an adventurous summer working on encapsulated liquid crystals.

The work discussed in this dissertation was only possible due to the ingenuity and dedication of several incredible researchers and collaborators. First, the printed graphene research was a result of the skill and resourcefulness of several members in the Briseño group, including Jae Joon (JJ) Kim, D. Leonardo (Leo) Gonzalez Arellano, and Özlem Usluer. Special thanks for JJ for spending additional time guiding me through the manuscript preparation and submission process. I would also like to acknowledge Ethan Secor, Professor Mark Hersam, and Professor Antonio Facchetti from Northwestern for providing essential materials for this work. Many thanks to Daniel Acevedo and Professor Ryan Hayward for expanding on this research to create solution-based devices.

Secondly, I would like to express my gratitude to Brenda Warren whose perceptive comments and persistence were invaluable to the electrowetting valve research. I am also grateful to Azar Alizadeh, Andrew Burns, and Ralf Lenigk for their guidance in creating wearable and integrated valves and allowing me to perform experiments at the GE Global Research Center. I would like to thank Xiyu Hu for her patience and wish her best of luck with her research. Thirdly, I would like to extend my deepest thanks to Yiliang Zhou for his development of the solution-based sensors and, more importantly, for his friendship and humor over the years. Special thanks to Anita Dey and Professor Jonathan Rothstein for the synthetic skin development and assessment, and Jeffrey Morse for his guidance when working with industrial collaborators. Fourthly, I have appreciated working alongside Dongpo Song on the creation of porous composite materials and have learned a great deal about conducting meaningful research from him. Lastly, I am grateful to all past and present Watkins Group members. I appreciate the time we have spent discussing research and experiments, traveling for conferences, and lingering over group lunch.

I would also like to extend my sincere thanks to the faculty and staff of the Polymer Science & Engineering department. I feel very fortunate to have had the opportunity to complete my Ph.D. at this world-class research center. In particular, I would like to thank John Nicholson for his help with all-manner of cleanroom instrumentation and advice on nanofabrication techniques. Special thanks to Alexander Ribbe and Louis Raboin for their patience and guidance in the electron microscopy facility and for teaching an excellent course on advanced microscopy methods. I would also like to thank all staff members in the front office, especially Lisa Groth, for their kindness over the years. Furthermore, I would like to express my gratitude to Jo-Ann

Bourguignon and MaryAnn Mish for handling all research-related paperwork and scheduling for the Watkins Group. In particular, I would like to thank Jo-Ann for her welcoming and joyful presence in my life.

I am incredibly grateful to all my friends for making graduate school such a memorable experience. First, I would like to thank all members of the PSE Class of 2013. From our recruiting weekend until today, thank you for all the celebrations, dinners, and drinks. I would like to individually thank the following friends for their kindness: Irene Howell, Gayathri Kopanati, Hyeyoung Kim, Shruti Rattan, Ben Yavitt, Tetsu Ouchi, Cristiam Santa, Sema Demirci, YuYing Tang, Connor Evans, Olga Linker, Sebastian Lips, Soonmi Kim, Piril Ertem, and Vanessa Sanchez. I cannot begin to express my thanks to Laura Lanier, who served alongside me as Coordinator for the high-school ASPIRE program for over three years. In particular, I am deeply indebted to Arianne Bazilio for her mentorship, encouragement, and advice on all matters.

Special thanks to Kara Martin (and Patrick), Erica Hartman, and Soeun Kim for being wonderful roommates over the years. Vielen Dank to Christian Malm for being a most excellent synthetic lab partner and hosting me for a remarkable Christmastime tour of Germany. Teşekkürler to Feyza Dundar and her family for inviting me to Turkey for an unforgettable wedding celebration. Furthermore, I would like to thank Feyza and Leo for all the laughter and great memories in A236. Most of all, I would like to thank Brandon Russell for making life feel so special over the past two years.

Finally, this achievement would not be possible without the twenty-eight years of encouragement, guidance, and patience from my family. Therefore, I would like to express my deepest love and gratitude to my parents, Rajiv and Vibha; my older brother,

Kedar; and my grandparents. Throughout my life, each of them has challenged me to remain curious about the world around me. One could not ask for more inspirational and positive role models, and it is because of them that I am able to stand where I am today.

ABSTRACT

DIRECT PRINTING OF CONDUCTIVE INKS FOR ORGANIC ELECTRONICS AND WEARABLE MICROFLUIDICS

FEBRUARY 2019

ADITI R. NAIK, B.S., CORNELL UNIVERSITY

M.S., UNIVERSITY OF MASSACHUSETTS AMHERST

Ph.D., UNIVERSITY OF MASSACHUSETTS AMHERST

Directed by: Professor James J. Watkins

This dissertation examines the direct printing of conductive inks on polymeric substrates for applications in organic electronics, microfluidic valving systems, and wearable sweat sensors. The inexpensive production of solution-based electrodes with high electrical conductivity is necessary to enable the next-generation of printed, flexible, and organic electronics. Specifically, the optimization and printing of liquid-phase graphene ink and nanoparticle-based silver ink by soft nanoimprint lithography and inkjet-printing is discussed to achieve printed functional devices. Using scalable low-cost patterning systems, these flexible applications are compatible with roll-to-roll processing, enabling large-scale manufacturing. This research expands the knowledge of high-resolution printing optimization for the direct patterning of organic electronics and development of sweat-based microfluidics for point-of-care diagnostic devices.

Chapter 1 describes the introduction of liquid bridge-mediated transfer printing of graphene ink for customizable electrodes and interconnects. Flexible, printed, and organic electronics are hindered by low transistor integration density due inherent size resolutions of traditional printing technology. In comparison, soft nanoimprint

lithography-based methods offer an alternative high-throughput method and roll-to-roll compatible patterning of electrodes. Graphene ink is directly printed using an ethanol liquid bridge to produce uniform and precise electrodes, squares, dots, and line arrays on a variety of substrates, illustrating the versatility of transfer printing. Furthermore, single-crystal transistors were fabricated using printed graphene electrodes with both n-type and p-type semiconductors, revealing excellent transfer and output characteristics in ambient conditions. Organic inverters were also produced by integration of n-type and p-type devices, demonstrating high gain values and symmetric switching. This work extends the high-resolution applications of solution-based graphene ink for the field of organic printed electronics.

The second chapter focuses on the development of robust electrowetting valves for sweat-based wearable microfluidic devices. Despite important advances in wearable sweat sensors, there are few reports regarding the integration of valving mechanisms into these devices. This incorporation of microfluidic valves for time-stamped sweat collection or multiple reagent reservoirs would enable the capability of complex analysis for improved personal health monitoring. Electrowetting valves offer compelling opportunities for portable, disposable, low-cost, and flexible valving systems with low power requirements for actuation. The fabrication and assessment of wearable electrowetting valves using a hydrophilic substrate for capillary-driven flow and medical-grade skin adhesive for conformal body contact is introduced. Moreover, these electrowetting valves for sweat-based microfluidics outperformed the electrowetting valves discussed in previous literature in terms of valve hold time and electrode spacing.

These solution-based and low voltage valves broaden the applications of electrowetting valves for point-of-care diagnostics in the area of noninvasive personal sweat monitoring.

Finally, Chapter 3 evaluates the performance of a microfluidic sweat sensing platform developed using scalable printed electronics and low-cost adhesive-based microfluidics. Sweat contains valuable information regarding electrolytes, amino acids, small molecules, and proteins levels within the body. Harnessed as a diagnostic tool, sweat would enable individuals to gain a deeper understanding of overall health status through personalized and wearable monitoring. Specifically, an inexpensive skin-compatible microfluidic platform is developed for continuous glucose monitoring through sweat. Solution-based electrochemical sensor electrodes are optimized for inkjet-printing and electrodeposition conditions. Additionally, an elastomeric polymer skin is fabricated, imitating human eccrine sweat gland size and distribution. This synthetic skin is integrated with the microfluidic glucose sensor to deliver artificial perspiration through the device at physiologically relevant sweating flow rates. Lastly, the sensor performance demonstrated glucose detection at levels measureable in human sweat for diabetic patients.

TABLE OF CONTENTS

Page

LIST OF FIGURES

Figure Page

CHAPTER 1

PRINTED GRAPHENE ELECTRODES FOR ORGANIC ELECTRONICS

The scalable fabrication of high-resolution electrodes and interconnects is necessary to enable advanced, high-performance, printed, and flexible electronics. We demonstrate the direct printing of graphene patterns with feature widths from 300 μm to ~310 nm by liquid-bridge-mediated nanotransfer molding. This solution-based technique enables residue-free printing of graphene patterns on a variety of substrates with surface energies between ~43 and 73 mN m^{-1}. Using printed graphene source and drain electrodes, high-performance organic field-effect transistors (OFETs) are fabricated with single-crystal rubrene (p-type) and fluorocarbon-substituted dicyanoperylene-3,4:9,10-bis(dicarboximide) (PDIF-CN_2) (n-type) semiconductors. Measured mobilities range from 0.2 to 2.1 $cm^2\ V^{-1}\ s^{-1}$ for rubrene and 0.1 to 0.6 $cm^2\ V^{-1}\ s^{-1}$ for PDIF-CN_2. Complementary inverter circuits are fabricated from these single-crystal OFETs with gains as high as ~50, as shown in Figure 1. Finally, these high-resolution graphene patterns are compatible with scalable processing, offering compelling opportunities for inexpensive printed electronics with increased performance and integration density.

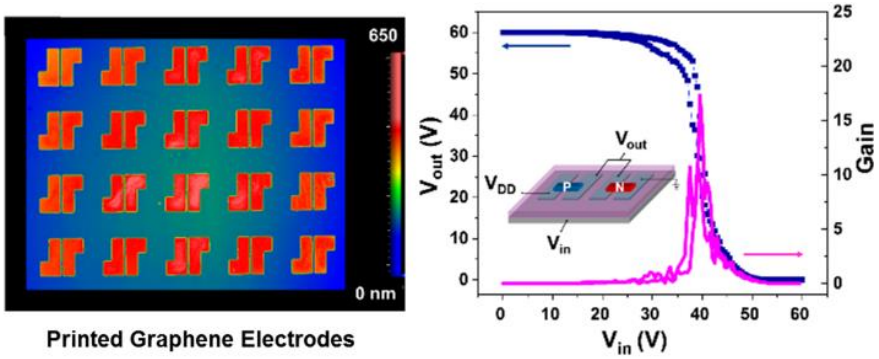

Figure 1. Printed Graphene Electrodes for Organic Inverters. (Left) Optical profilometry of graphene electrodes, (Right) Inverter schematic and performance characteristics of p-type and n-type single-crystal semiconductors on graphene electrodes.

1.1 Introduction

Flexible, printed, and organic electronics are predicted to dominate a $73.4 billion market by 2027, demonstrating rapid growth from the recent $29 billion market in 2017. This market advancement will be largely driven by organic light-emitting diodes (OLEDs) for display applications, *e.g.* monitors, televisions, laptops, smartphones. The second largest contributor will be the conductive inks developed for direct and solution-processable patterning of interconnects used in printed electronics. These conductive inks are mainly derived from metal nanoparticles or infused with carbon nanomaterials and valued for their mechanical flexibility and low resistivity. Flexible electronics are also poised for tremendous growth, particularly in the fields of integrated logic devices and reliable sensors; however, these areas still require extensive research and development prior to commercialization.[1]

A critical challenge for large-scale production of flexible, printed, and organic electronics for low-cost, high-performance applications remains the realization of inexpensive and high-throughput fabrication.[2] For rigid silicon-based electronics, expensive nanofabrication facilities are built for individual processing of integrated circuit chips. Each chip is produced by extensive manufacturing through separate lithography, deposition, and etching fabrication units housed within a cleanroom environment. Similarly, organic electronics are commonly produced by high-pressure vacuum-based thermal evaporation and deposition of metals and organic small molecules within an inert glove box environment.[3] In contrast, truly low-cost and rapid device fabrication can be achieved by roll-to-roll processing, also known as web processing. This technology originated from the coating and paper industries where several

manufacturing steps are performed on a single roll of material at fast production speeds. For electronics, roll-to-roll processing would allow for multiple processing steps ideal for solution-based methods, *e.g.* printing, coating, deposition, *etc.*, to occur on a single roll of plastic or metal foil as shown in Figure 2 below.[4] Therefore, it is imperative to translate expensive organic electronics fabrication to solution-based, roll-to-roll amendable methods.

Figure 2. Roll-to-roll manufacturing. (Left) Watkins group roll-to-roll coater. (Right) Fabrication of high-resolution nanoimprinted polymer structures by roll-to-roll processing.

1.2 Organic Field-Effect Transistors

The transistor is the key component of modern electronics, which serves as an electric valve to control and direct the flow of electrons. Developed by John Bardeen, Walter Brattain, and William Shockley in 1947 at AT&T's Bell Labs, the first transistor was produced using germanium as a semiconductor with gold contacts. Bardeen, Brattain, and Shockley were later awarded the Nobel Prize in 1956 in Physics for their ground-breaking work on semiconductors and transistors. The term "transistor" was first coined by John Pierce, as a combination of the words: tranconductance and varistor, and selected through an internal vote within Bell Lab employees.[5] Scientific advances led to

the integration density of transistors doubling every year, a trend that was termed "Moore's Law" by Intel cofounder Gordon Moore, as shown in Figure 3a.[6] Presently, silicon-based transistors are pushing the 10 nm node, resulting in the most high-performance electronics to date; however, it is difficult to integrate silicon into flexible electronic devices due to silicon's inherently brittle nature and lack of flexibility.

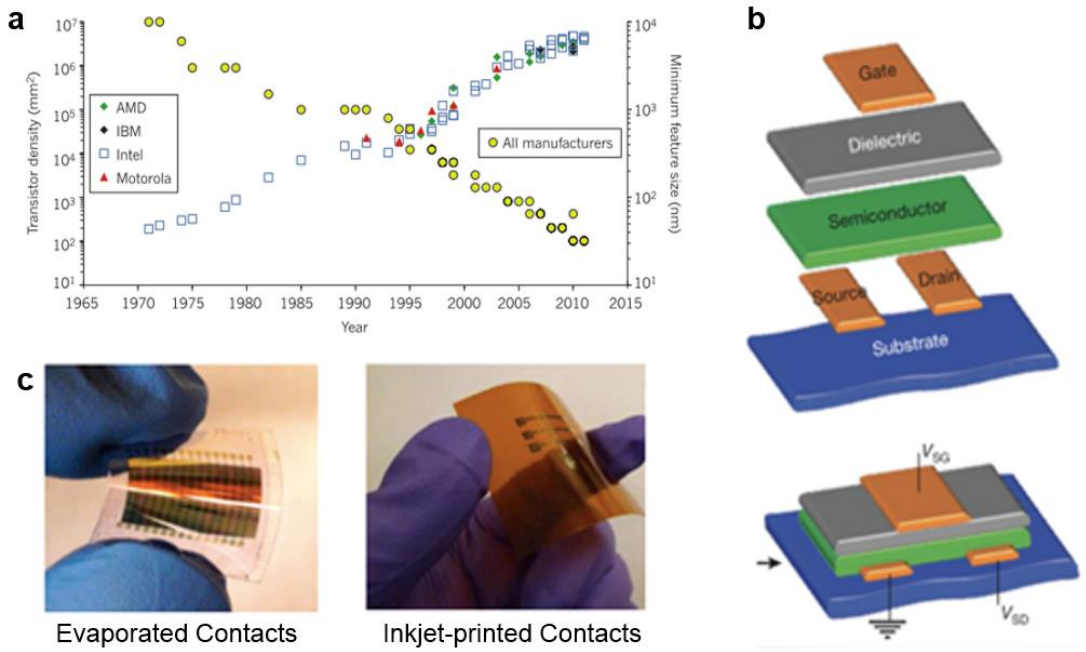

Figure 3. Design of Flexible Organic Transistors. (a) Moore's law demonstrating current silicon-based transistor feature size.[7] Flexible transistors currently have channel lengths ~50um, comparable to silicon-based transistor size before pre-1970s. (b) Schematic of flexible, organic field-effect transistor device.[8] (c) Evaporated gold electrodes for OFET[9] (left), and inkjet-printed silver electrodes for OFET[10] (right).

Therefore, researchers have focused on improving the organic field-effect transistor (OFET), which is based on organic small molecules or polymers to allow for truly flexible and even transparent transistors. The OFET is composed of conductive source and drain electrodes connected by a semiconductor material, which can control electric current by switching between an ON and OFF state. Above the semiconductor sits the dielectric layer, which allows for the electric polarization of charges, which is

controlled by the conductive gate electrode, as shown in Figure 3b.[11] Over the past 25 years, incredible advances in the field of OFET research have improved device performance by 3-4 orders of magnitude and led to a greater understanding of transport phenomena within organic semiconductors.[11]

A brief introduction to the operation of an OFET begins with a discussion of charge density modulation within the semiconductor layer, which is probed through three observable external quantities, shown in Figure 4a.[12] An applied voltage, known as the source-drain voltage (V_{ds}), is applied to the source electrode, resulting in charge injection from the electrode into the semiconductor material. Efficient charge injection is dependent on the relationship between the work function of the conductive electrode and the molecular orbital energy levels of the semiconductor material. This remains a critical issue for OFETs, since poor charge injection will result in decreased performance and increased contact resistance.[13] Significant research has improved hole-transporting p-type semiconductors as well as electron-transporting n-type semiconductors. Next, the charge density within the semiconductor or active layer is modulated by an applied gate-source voltage (V_G) through the insulator layer. The choice of the dielectric material is important as it influences the operating voltage of the OFET device. A poorly deposited dielectric layer may introduce pinhole defects, leading to undesired leakage currents between the gate electrode and source or drain electrodes.[14] Finally, drain-source current (I_{ds}) refers to the current which passes through the active layer and is collected by the drain electrode. The I_{ds} of a device can be largely affected by unwanted charge traps at the semiconductor-dielectric interface and are especially a challenge for solution-based OFETs.[15]

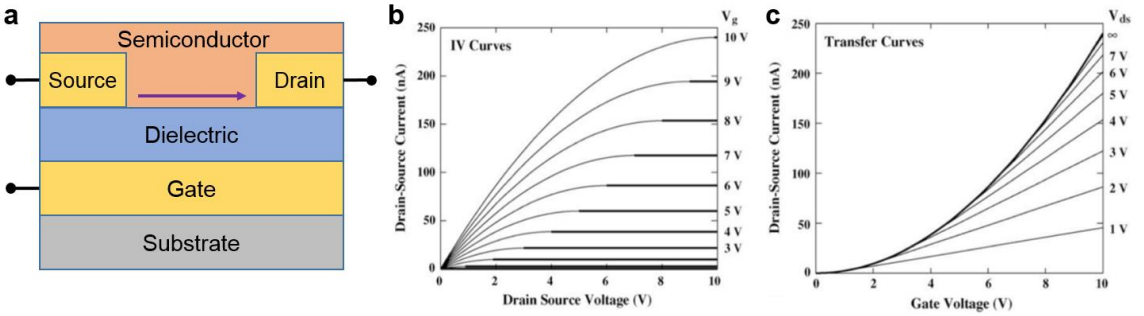

Figure 4. OFET Performance. (a) Schematic of components and current flow within an OFET. Representative (b) output curves of I_{ds} versus V_G demonstrating the linear regime at low V_G and (c) transfer curves of I_{ds} versus V_{ds}.[12]

Using these three measurable quantities (I_{ds}, V_{ds}, V_G), the following three important performance characteristics: electron mobility (μ), voltage threshold (V_T), and switching current ratio ($I_{ON/OFF}$) can be calculated. The basic relationship between these parameters are described in the subsequent two equations, which are fully derived and explained in several book chapters and tutorials.[12,16]

$$\text{Linear Regime: } I_{ds} = \frac{W}{L}\,\mu C_i\left(V_G - V_T - \frac{V_{ds}}{2}\right)V_{ds} \qquad [1]$$

$$\text{Saturation Regime: } I_{ds} = \frac{W}{2L}\,\mu C_i\left(V_G - V_T\right)^2 \qquad [2]$$

Additionally, the device channel length (L), width (W), and capacitance per unit area (C_i) must be known. The OFET operates in the saturation regime when the I_{ds} reaches a plateau when plotted against V_{ds}, as shown by the bolded lines of increasing V_G on a representative output curve in Figure 4b, and in the linear regime prior to this occurrence at low V_{ds} values. If the I_{ds} is plotted instead against the V_G at increasing V_{ds}, this is known as the transfer curve (see Figure 4c). The V_T describes the voltage needed to produce a conducting channel through the active layer, effectively turning the device ON, while the $I_{ON/OFF}$ demonstrates the ratio of I_{ds} between the ON and OFF states of the

device. Finally, μ can be experimentally obtained through calculating the slope in Equations 1 or 2 above.[14]

During the fabrication of organic electronics, particularly organic transistors, one of the most costly and time-consuming steps is the deposition of metal contacts for the source, drain, and gate electrodes. The most common technique is vacuum evaporation of metal through a shadow mask in an inert atmosphere, ordinarily within a glove box or clean room environment. Precious metals, such as gold, silver, and platinum, are commonly used for OFET electrodes.[11] The high cost of these electrodes derives from the expensive nature of these metals, *e.g.* gold is $1200 per ounce, as well as the energy required to pressurize the vacuum chamber. However, there are two key advantages of using evaporated metal electrodes: the chemical nature of these materials and the high-resolution patterning achieved by evaporation. First, these highly conductive metals demonstrate chemical stability and inertness while in contact with a variety of semiconductors, dielectrics, and solvents. Secondly, gold electrodes have well-matched work functions for efficient charge injection into semiconductor materials, and offer routes to tailor their energetic compatibility through doping by self-assembled monolayers. Finally, these materials are electrically capable and robust to handle large voltages and currents over long periods of time.[17]

The second advantage refers to the patterning resolution achievable by vacuum evaporation of metals, which is unparalleled compared to conventional printing technologies, reaching resolutions of 5-10 μm (see Figure 3c).[18] Recent advances in printing technologies have explored pathways to produce metal conductors using metal nanoparticle-based inks and fabricating transistors contacts by inkjet-printing, screen-

printing, and gravure printing. However, these methods are inherently limited by low throughout and low resolution.[19] Optical images of evaporated gold electrodes and inkjet-printed silver electrodes are shown in Figure 3c. Transistors fabricated by solution-based printed approaches for flexible electronics remain above 50 μm in channel width (comparable to pre-1970s technology) due to the resolution limitations of these commercial processing techniques.[7] To translate these advantages to a low-cost, roll-to-roll process, both an alternative conductive material and processing technique are required.

1.3 Soft Nanoimprint Lithography

As the semiconductor industry achieved higher transistor integration in accordance with Moore's law, the production cost for integrated circuits similarly increased dramatically. Presently, the industry is focused on developing extreme ultraviolent lithography, known as EUV, to attain 13.5 nm feature size by 2020. A critical challenge to ensure the future success of high-performance electronics is the realization of manufacturing techniques that possessed nanoscale accuracy and precision. Several technologies to produce submicron features exist, including electron beam, x-ray, and scanning probe lithography; however, these methodologies are high cost and low throughput, resulting in expensive manufacturing facilities.[20] Currently, directed self-assembly of block copolymers as a bottom-up fabrication method and nanoimprint lithography as a top-down method have shown potential for next-generation nanoscale patterning.[21]

Nanoimprint lithography was first established in a landmark *Science* paper by Stephan Chou, Peter Krauss, and Preston Renstrom at the University of Minnesota in 1996.[22] This technique was inspired by compression molding, where a material is placed in contact with a prefabricated patterned mold and subjected to high temperature, used to produce the micron-scale grooves on CDs. Similarly, for nanoimprint lithography, a hard master mold of silicon oxide on a silicon wafer was patterned with 25 nm features using electron beam lithography. This master was then pressed into poly(methyl methacrylate) (PMMA), which was heated above its glass transition temperature as shown in Figure 5a, and the residual layer was removed by reactive ion etching. Next, gold was vacuum-evaporated over the nanoimprinted PMMA, which was subsequently dissolved by acetone, producing precise and uniform sub-25 nm gold features.[22]

At the same time, researchers in George Whitesides's group had developed the process of soft nanoimprint lithography the early 1990s at Harvard University. A key challenge for nanoimprint lithography is damaged incurred on the hard master mold over several printing replications, which must be reproduced using conventional lithography in a clean room environment. In comparison, Whitesides's group developed soft elastomeric daughter molds using poly(dimethyl siloxane) (PDMS), allowing for a low-cost alternative, which could be replicated countless times from the original silicon master mold. To accomplish this, PDMS was cured over a fluorinated master mold and peeled from the surface, producing a flexible and patterned mold that is also compatible with roll-to-roll processing.[22] The PDMS molds or stamps were demonstrated to produce clean nanoscale structures with minimal shrinkage. After a decade of dedicated research, soft nanoimprint lithography has been developed to pattern both organic and inorganic

materials, including nanoparticles for a wealth applications across several fields of research. In the Watkins's group, researchers have utilized solvent-assisted nanoimprint lithography to produce nanostructures antimicrobial surfaces, lithium ion batteries, biosensors, and photonic woodpile structures as shown in Figure 5. Related direct printing methods to fabricate structures using soft nanoimprint lithography, include mircocontact printing,[23] microtransfer printing, and micromoulding in capillaries.[24] However, many of these methods still suffer from complex processes with multiple steps and undesired residual layers between structures.

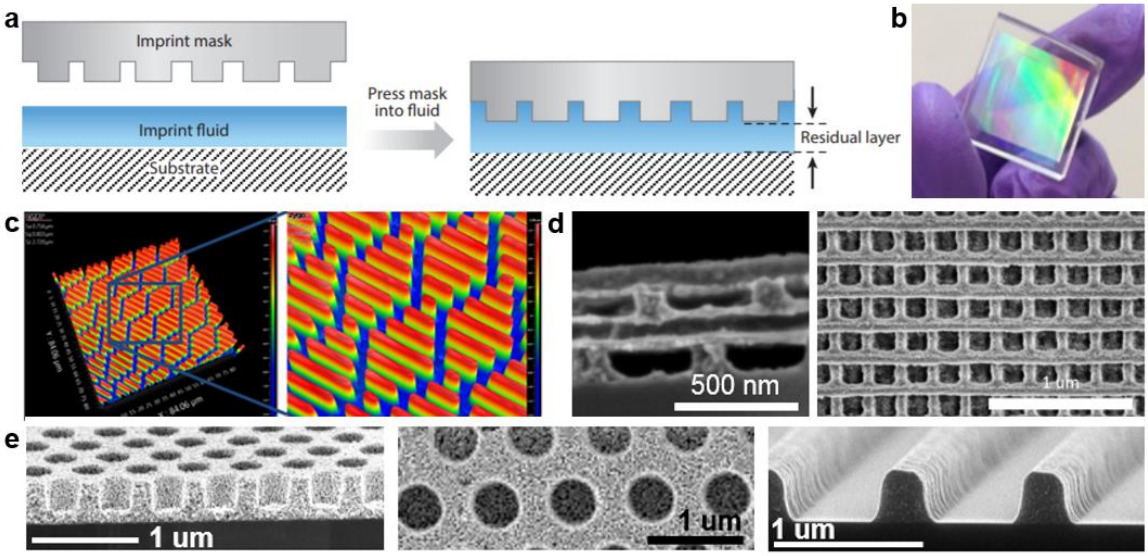

Figure 5. Soft Nanoimprint Lithography and Applications. (a) Illustration of nanoimprint lithography.[20] (b) PDMS mold derived from nanopatterned silicon master mold. (c) Nanoimprinted antimicrobial surface by Feyza Dundar. (d) 3D woodpile structure for photonic applications by Irene Howell. (b) Various nanostructures and features imprinted by Rohit Kothari.

A recently developed approach to direct printing which relies on PDMS molds is liquid-bridge-mediated transfer molding process (LB-nTM), demonstrated by Sung *et al.* (2010) to print high-resolution structures on a variety of substrates.[26] Here, microscale patterns are created on the PDMS molds, which instrinsically have a low surface energy of 20 mJ/m^2.[26] These structures within the PDMS stamp are back-filled with an ink using

discountinuous dewetting, which is dependent on the difference in surface tension of the ink with respect to the surface energy of the mold material. Generally, the ink solution must have a surface tension of 30-70 mJ/m^2 to dewet cleanly without leaving a residual layer on the surface of the stamp. To print, a few drops of the ink solution are pipetted onto the patterned stamp and drawn over the surface using a needle, allowing the ink to fill the structures, but dewet completely from the surface of the stamp. This printing also results in the transferred pattern suffering no surface diffusion during the printing process, preventing the formation of a residual layer between the structures.[27,28] As shown in Figure 6a, a layer of a polar solvent serves as the capillary bridge between the dried ink confined in line array mold and the substrate, resulting in uniform and cleanly printed structures with small feature sizes.

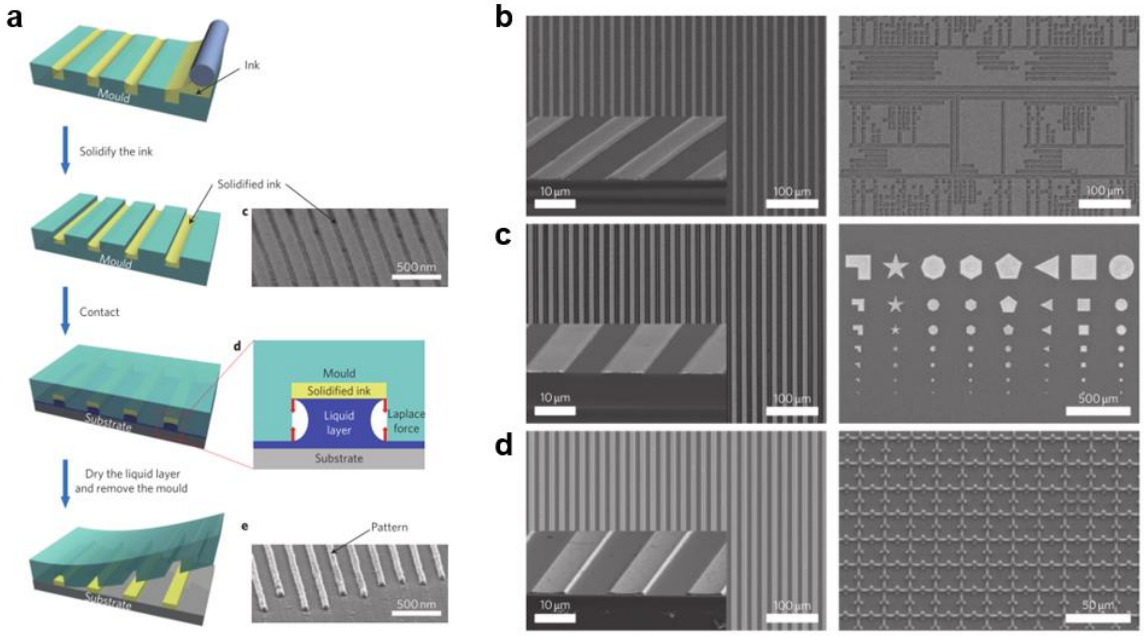

Figure 6. Liquid-bridge Mediated Nanotransfer Moulding.[26] (a) Schematic of liquid-bridge-mediated nanotransfer molding using silver ink. (b) Patterned zinc-tin oxide particles. (c) Patterned silver nanoparticles. (d) Patterned 6,13-bis(triisopro-pylsilylethynyl) pentacene (TIPS-PEN).

1.4 Solution-Processable Graphene Ink

Graphene has attracted tremendous scientific interest over the past decade in the field of printed electronics due to its high conductivity, superior electronic properties, chemical stability, and intrinsic flexibility.[29,30] The primary method of graphene production centers on carbon vapor deposition (CVD) where graphene is growth directly on metal foils.[31] Additional techniques include reduced graphene oxide,[32] mechanical exfoliation,[33] and laser-annealed graphene.[34] Despite these advances, these methods suffer from high temperature processing and complex procedures to create graphene films. Liquid-phase exfoliation of graphite capped with a stabilizing polymer offers an alternative strategy for the rapid production of low-cost and high quality graphene ink.[35] An advantage of a stable dispersion of graphene is the tunability of the solvent, viscosity, and surface tension of the ink.

The graphene ink developed in the Hersam group at Northwestern University shows great potential as a non-metallic conductive material for electrodes and interconnects for flexible electronics. The ink is produced by a liquid exfoliation method from graphite in a solution of ethanol and ethyl cellulose by probe ultrasonication, and is available for purchase through Sigma-Aldrich. The ethyl cellulose acts as a polymer stabilizer to prevent aggregation of graphene flakes composed of a few layers of pristine graphene, allowing for a stable dispersion of graphene ink in ethanol. As shown in Figure 7b, the graphene ink has been demonstrated to be inkjet-printed on flexible substrates with no issues of delamination or poor adhesion. Previous literature demonstrates that the flake thickness within the solution is measured to be between 1.6-1.8 nm with a variation of flake lateral dimension of 50-400 nm. The conductivity of thin films of graphene on

SiO_2 were measured to 2.5×10^4 S/m following thermal annealing at 250°C for 30 min. This short annealing time is required to decompose the ethyl cellulose and allow for densification of the graphene flakes. Raman spectroscopy on annealed graphene films showed insignificant oxidation.[35]

This graphene ink has been successfully used to fabricate OFETs,[36] SCs,[37] diodes,[38] and bioscaffolds,[39] by inkjet-printing,[40] gravure printing,[41] and screen-printing on flexible substrates[42], showing the potential for scability of this ink for industrial purposes for a range of applications (see Figure 7). However, traditional printing techniques for graphene ink offer limited capability to reach smaller features and higher resolutions while maintaining scalability.[19] This concern was recently addressed by Song *et al.*, who demonstrated transfer printing of graphene ink, reaching a line width of 3.2 μm.[43] However, this method is constrained by its reliance on a UV-curable adhesive as a substrate to transfer the graphene ink. Therefore, an efficient and versatile strategy for printing graphene ink directly onto arbitrary substrates using scalable methods remains a critical challenge.

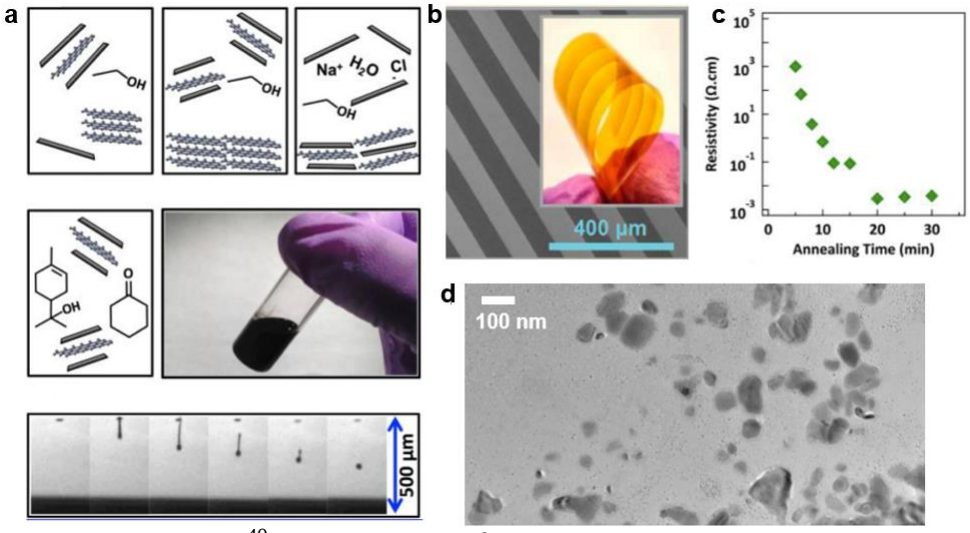

Figure 7. Graphene Ink.[40] (a) Graphene flakes are capped with ethyl cellulose and dispersed in an ethanol solution. (b) Inkjet-printing droplet formation of graphene ink. (c)

Scanning-electron microscopy (SEM) image of printed graphene lines on polyimide substrate. (d) Low-temperature annealing time to produce conductive graphene. (e) Transmission electron microscopy (TEM) image of graphene flakes.

1.5 Research Objectives

Here, we present the direct printing of graphene ink by LB-mNT to produce residue-free patterns on a variety of substrates for organic electronic applications. Several NIL techniques have been implemented to pattern graphene structures, such as electrodes[44], nanorings[45], and ribbons[46,47]. However, these approaches rely on CVD-grown or mechanically exfoliated graphene with multiple etching procedures before reaching the desired graphene patterns. Solvent-assisted NIL using reduced graphene was also implemented, but required high-temperature annealing following printing.[48] In comparison, a solution-based approach using low-temperature processing to pattern graphene features in ambient environments would harness the capability of this stable and conductive material.

To print, liquid-bridge-mediated nanotransfer molding (LB-nTM) will be used, for which a layer of solvent serves as a liquid-bridge between the graphene confined in a mold and the target substrate.[26] Using graphene source and drain electrodes, we will fabricate organic transistors and complementary inverters based on single-crystals of rubrene and fluorocarbon-substituted dicyanoperylene-3,4:9,10-bis(dicarboximide) (PDIF-CN_2), characterizing device mobilities, inverter performance, and gain values. This solution-based, cost-effective, and low-temperature procedure would be promising for scalable manufacturing of graphene micropatterns on a variety of substrates for printed and flexible electronics.

The organic electronic work on transistors and inverters discussed in this chapter are the result of a close collaboration with Professor Alejandro Briseño and his research group, particularly Dr. Jae Joon Kim, Dr. Özlem Usluer, and Dr. D. Leonardo Gonzalez. The graphene ink was produced by Dr. Ethan Secor in Professor Mark Hersam's group and the PDIF-CN_2 single-crystals by Professor Antonio Facchetti at Northwestern University. This work was funded by the Center for Hierarchical Manufacturing led by Professor James Watkins. The discussion that follows has also been peer-reviewed and published in *ACS Applied Materials and Interfaces* (DOI: 10.1021/acsami.8b01302) in early 2018.

1.6 Experimental Section

The graphene ink formulation was produced by ultrasonication of graphite and stabilized by ethyl cellulose, as reported in previous literature,[35] and dispersed in ethanol to form a 10 mg mL^{-1} graphene dispersion. The ethanol was evaporated under a constant flow of air. The graphene and ethyl cellulose solid was redispersed into isopropanol (IPA) and sonicated for 20 minutes. N-methylpyrrolidone (NMP) was then added into the solution and sonicated for another 20 minutes. The final graphene ink used for transfer printing contained 53 mg mL^{-1} graphene in a solvent system containing 4:1 IPA to NMP by volume. The IPA and NMP were provided by Fisher Scientific.

The polydimethylsiloxane (PDMS) molds were fabricated from polymeric masters for transfer printing micropatterns of graphene ink. Patterns were produced on SU8 photoresist (MicroChem) using a Mylar photomask (FineLine Imaging) by UV photolithography in a cleanroom environment. The SU8 master mold was exposed to

oxygen plasma for 2 minutes and fluorinated by vapor deposition of the silanizing agent (tridecafluoro-1,1,2,2- tetrahydrooctyl) trichlorosilane (Gelest, Inc.) for several hours at 60°C. PDMS molds were created using Sylgard 184 (Dow Corning) mixed in a ratio of 1:10 curing agent to elastomeric base. This mixture was poured over the SU8 master and allowed to cure overnight at 60°C. The PDMS molds were peeled from the SU8 masters and used for printing. The depth of the PDMS molds was ~2.2 um for the electrode design as determined from the SU8 master height profile (Figure 8).

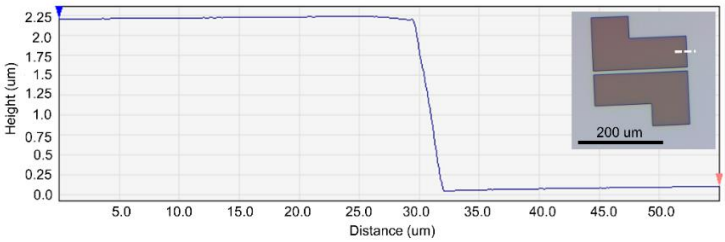

Figure 8. Height of SU8 master for printed electrodes measured by optical profilometry to be 2.25um (measurement taken at white dotted line). The height of the fabricated PDMS daughter molds will demonstrate similar dimensions to the original master mold.

To fill the molds by LN-nTM, a drop of graphene ink was pipetted onto the corner of the PDMS molds and drawn over the surface using a needle. The ink filled the structures within the mold, but dewetted from the surface of PDMS, leaving no residue between the patterns. The filled molds were heated at 65°C for 30 minutes to remove residual solvent, leaving dried graphene flakes with ethyl cellulose within the mold. For printing, a drop of ethanol (Pharmco-Aaper) was cast over the substrate and the mold placed over the solvent layer to produce a liquid-bridge between the dried graphene ink and substrate. The mold remained over the substrate for 1 hour at 65°C until the ethanol permeated through the PDMS. The mold was then removed, having transferred the graphene and ethyl cellulose to the substrate. The printed patterns were annealed at

250°C for 30 minutes to decompose the ethyl cellulose, producing conductive graphene patterns.

To fabricate the devices, silicon wafers with a 300 nm SiO_2 layer (Addison Engineering) were cleaned by sonication using soap and water, water, acetone, and isopropanol, each for 15 minutes, and dried under a stream of N_2. Prior to device fabrication, the wafers were exposed to UV/Ozone treatment for 10 minutes. For both OFETs and inverters, graphene electrodes were printed and annealed on the surface of the SiO_2/Si wafer. High quality, single-crystals of rubrene and PDIF-CN2 were grown by physical vapor transfer (PVT), as described previously.[49] The crystal dimensions were several millimeters in length and width and ~200 to 800 nm in thickness. Single-crystals were placed on top of the graphene electrodes to complete the organic field-effect (OFET) and inverter fabrication, and all devices were measured under ambient conditions.

Several characterization techniques were used to analyze the graphene ink and printed graphene patterns. For the graphene ink used for LB-nTM, the ink viscosity (m-VROC Viscometer, RheoSense) and surface tension (Sigma 701 Force Tensiometer, Dyne Testing) were measured. Optical microscopy (OM, Zeiss Axio Scope A1), scanning electron microscopy (SEM, FEI Magellan 400 XHR) and energy dispersive x-ray spectroscopy (EDS, FEI Magellan 400 XHR) were used to image the surface of the graphene patterns. A 3D optical surface profiler (OP, Nexview, Zygo Corporation) was used to measure height profiles of printed graphene, and atomic force microscopy (AFM, Veeco Dimension 310) was used for surface roughness measurements. The conductivity of planar films of graphene ink was measured by a four-point resistivity system from

Signatone. The OFET and inverter devices were characterized using a Keithley 4200 system. The surface energy of the various substrates was determined by the geometric mean method with diiodomethane (Sigma Aldrich) and water using a video contact angle system (VCA Optima, AST Products, Inc.).

1.7 Printed Graphene Structures

The fabrication of printed graphene electrodes by LB-nTM is shown below. Here, microelectrode structures composed of opposite facing "Alphabet L" designs with 10 μm and 50 μm gaps were selected for printing to allow for straightforward OFET measurements. For LB-nTM, polydimethylsiloxane (PDMS) molds were filled with graphene ink as a result of discontinuous dewetting.[18,19] Optical microscopy (OM) and scanning electron microscopy (SEM) images of the mold are shown in Figure 9e and f.

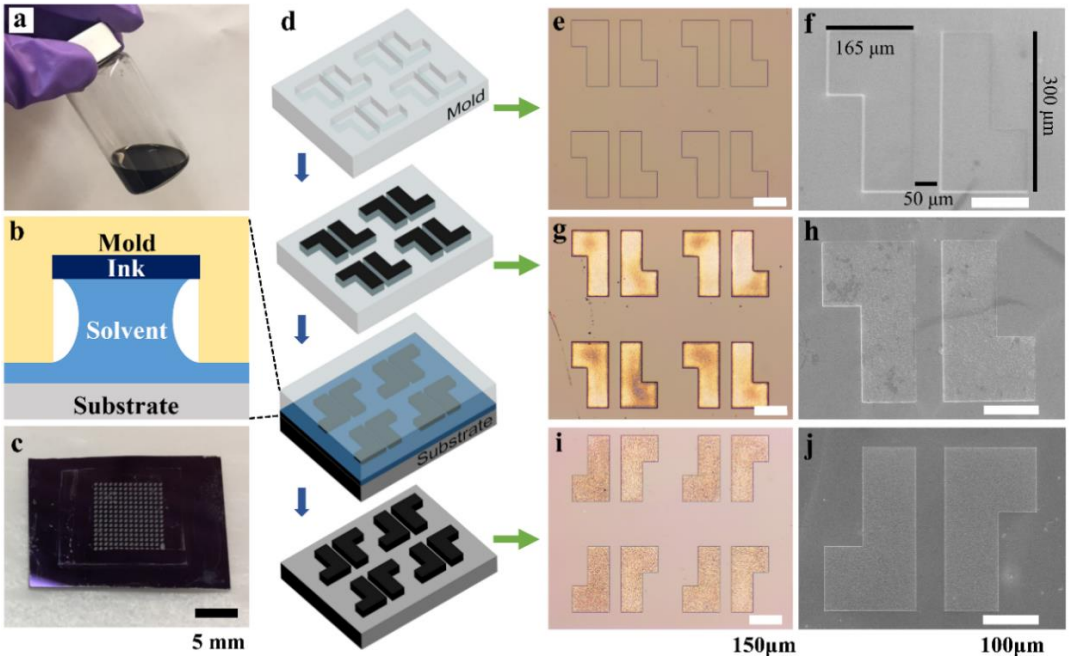

Figure 9. Direct printing of graphene electrodes. (a) Image of a vial of graphene ink. (b) Illustration of liquid-bridge created by solvent between dried graphene ink and substrate. (c) Large-area image of graphene electrodes printed on SiO_2 substrate. (d) Schematic of printing graphene ink by LB-nTM. (e-j) OM and SEM images, respectively, of (e, f)

PDMS mold, (g, h) graphene ink within mold, and (i, j) graphene electrodes printed onto SiO_2. Scale bar for OM images is 150 μm and for SEM images is 100 μm.

The solvent system for the graphene ink was specifically designed for LB-nTM printing. This graphene ink is a stable dispersion of graphene flakes produced by liquid-phase exfoliation from graphite in a solution of ethanol and ethyl cellulose by probe ultrasonication, as discussed in previous literature.[35] The ethyl cellulose acts as a polymer stabilizer to prevent aggregation of the graphene flakes, which range from 1 to 5 nm in flake thickness and 50 to 400 nm in lateral dimension.[35] The graphene ink produced for LB-nTM was composed of 53 mg mL^{-1} graphene stabilized by ethyl cellulose in 4:1 isopropanol (IPA) and N-methylpyrrolidone (NMP) by volume, as shown in Figure 1a.

To fill the PDMS molds, a drop of ink was drawn across the surface of the mold with a needle. The low boiling point of IPA (82 °C) allowed for effective discontinuous dewetting from the PDMS surface, and the high boiling point of NMP (204 °C) prevented evaporation prior to complete filling of the mold. The IPA evaporated quickly to allow for dewetting, while the NMP evaporated slowly enough to fill the individual structures within the molds. Without such a solvent system, the graphene dispersion would not fully dewet from the mold surface, or only partially fill the patterned areas. The graphene ink has a surface tension of ~28 mJ m^{-2} and viscosity of ~11 mPa s (see Figure 10), which uniformly filled the mold patterns and dewet from the PDMS surface (surface energy, γ = 20 mN m^{-1}).[26] Prior to printing, the molds filled with graphene ink were dried on a hot plate to remove the solvent.

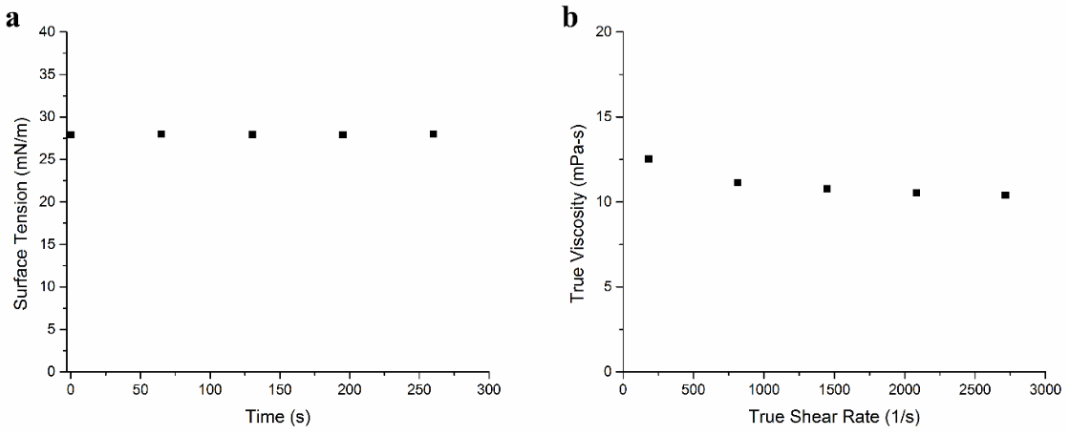

Figure 10. Graphene ink properties for LB-nTM printing. (a) Surface tension of graphene ink. (b) Viscosity of graphene ink by rate sweep measurement.

For printing, a thin film of a polar solvent served as the capillary bridge between the dried ink within the PDMS mold and the desired substrate. A drop of ethanol was dropcast onto the substrate, and the mold was placed on top immediately. Previous literature indicates that water is also a suitable liquid-bridge solvent for LB-nTM printing.[51,52] Since solvent polarity can be approximated by dielectric constant, we expect the LB-nTM method will function for solvents with dielectric constant between 24.3 (ethanol) and 80.4 (water) at room temperature.[53] However, ethanol offers several advantages over using water or other organic solvents when printing electrodes for electronics devices. The lower surface tension of ethanol (γ = 22.07 mN m^{-1})[54] compared with water (γ = 71.99 mN m^{-1})[55] allows for increased wetting of the desired substrate. Ethanol will evaporate quicker than water, which leads to faster printing.[56] Additionally, printing with a water liquid-bridge may introduce impurities and contaminants on the surface, which would serve as charge traps or affect the dielectric or semiconductor layers used in the device.[57] Finally, ethanol is considered an environmentally-friendly solvent with a low EHS indicator score and is commonly used in household products and industrial processes.[58] Methanol is the only other polar solvent with a low indicator score,

but it is toxic in large quantities and known to cause blindness. Therefore, compared with other solvents, printing with ethanol will allow for a safer and faster route to large-scale fabrication of this type of printing technique.

The mold remained over the substrate until the ethanol evaporated, transferring the graphene flakes with ethyl cellulose onto the substrate. The mold was then peeled off the substrate to reveal uniformly printed graphene patterns. The transferred graphene patterns suffered no surface migration or fracture during the direct printing process, preventing residue formation between the patterns. The large-area print, OM image, and SEM image of the graphene electrodes on SiO_2 are shown in Figure 9c, i, and j, respectively.

Following printing, the graphene patterns were annealed at 250°C to decompose the ethyl cellulose capping the graphene flakes, which allowed for efficient flake-to-flake charge transport and thus highly conductive patterns.[40] The planar conductivity of spin-coated films at the thickness of the 10 μm and 50 μm electrodes was ~7.8×10^3 S m^{-1} and ~8.1×10^3 S m^{-1}, respectively. The sheet resistance of the graphene ink was measured to be ~5.9×10^2 Ω sq^{-1}. The graphene electrodes were further characterized by SEM as shown in Figure 11, demonstrating well-packed graphene flakes confined to the desired printed regions.

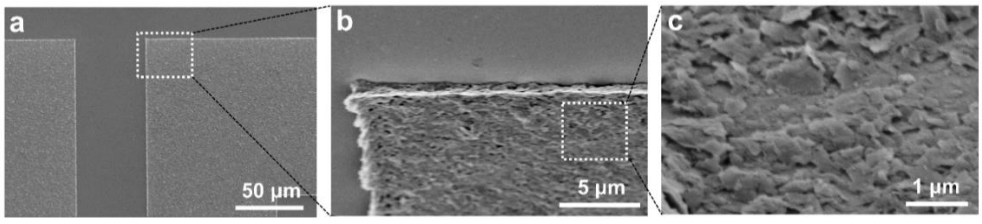

Figure 11. SEM images of graphene surface. (a) Graphene electrodes, (b) Tilted edge of electrode, (c) High-resolution image of graphene flakes on electrode surface.

Along with the electrode patterns, micropatterns and nanopatterns of graphene squares, dots, and line arrays were printed on SiO_2, as shown in Figure 12. The larger graphene micropatterns, such as the electrode design (Figure 12j), squares (Figure 12b), and dots (Figure 12e), demonstrate the printing uniformity by LB-nTM over large areas, while the line array pattern demonstrates the high-resolution patterning achievable with this graphene ink, shown in Figure 12h, i. The width of the graphene lines is 310 nm ± 60 nm (average of 30 line width profiles), similar to the lateral dimension of individual graphene flakes, and thus approaching the maximum resolution for this ink. To reach higher resolutions, the flake size could be decreased further by mechanical or chemical routes prior to ink formulation.

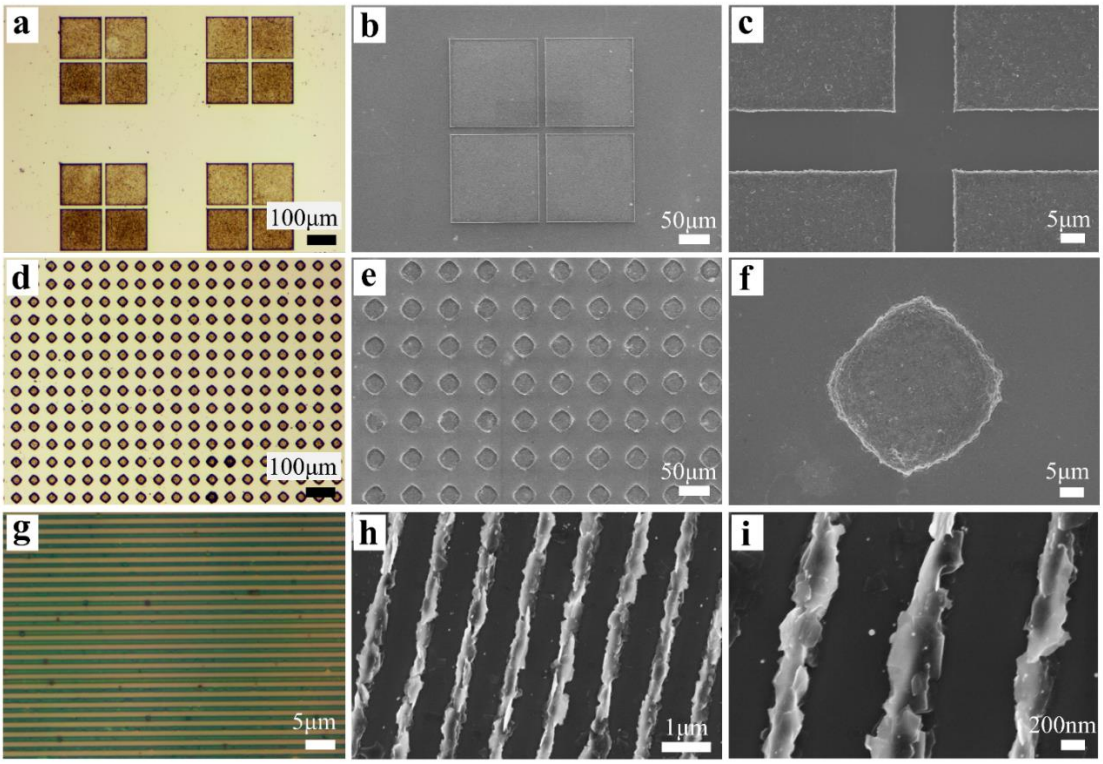

Figure 12. SEM images of printed graphene patterns on SiO_2. OM images of printed graphene (a) squares, 140 μm by 140 μm, (d) dots, 35 μm diameter, (g) lines, 310 nm ± 60 nm width. SEM images of graphene (b, c) squares, (e, f) dots, and (h, i) lines.

Graphene patterns can be directly printed onto a variety of substrates using LB-nTM. In comparison, conventional direct printing methods, such as inkjet, screen, and aerosol jet printing, require time-consuming optimization to tailor the printing conditions of an ink to the surface energy of the substrate.[59] LB-nTM printing uses a liquid-bridge to facilitate printing, which is less affected by the surface energy of the substrate. Ethanol as the liquid-bridge solvent allows for increased wetting on surfaces due to its low surface tension (γ = 22.10 mN m^{-1}).[54] As shown below, graphene electrodes can be reliably printed on several substrates commonly used for printed electronics, including SiO_2, glass, gold, polyethylene terephthalate (PET), and polyimide (PI). These substrates demonstrated a range of surface energies between ~43 and 73 mN m^{-1}, which are within the expected values for these materials.[60,61-62] The results highlight the adaptability and versatility of this printing method to a broad range of surfaces. As a note, while the printed graphene in Figure 13d is unannealed due to the limited thermal stability of PET, photonic annealing could be accomplished for this sample without damaging the low-temperature substrate.[63]

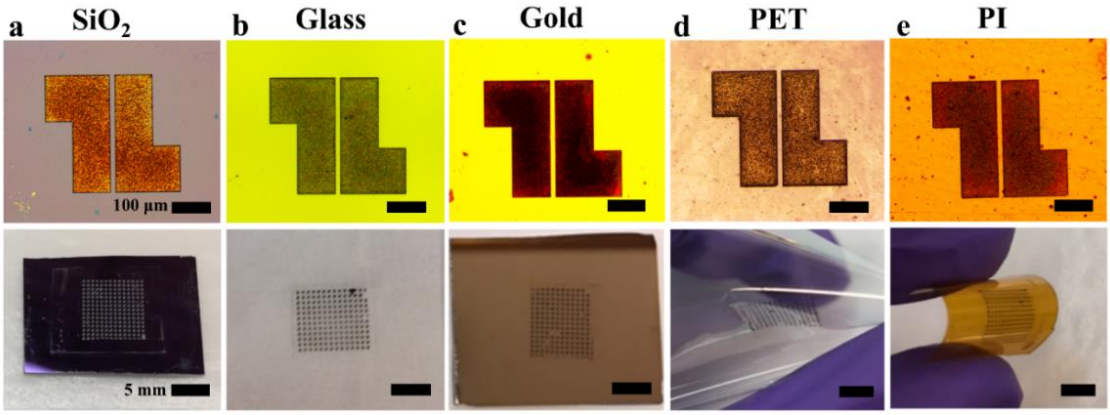

Figure 13. Graphene electrodes printed on a variety of substrates. OM image, scale bar 100 µm (top) and large-area sample, scale bar 5 mm (bottom) of printed graphene electrodes on (a) SiO_2 (surface energy, γ~73 mN m^{-1}), (b) glass (γ~68 mN m^{-1}), (c) gold (γ~47 mN m^{-1}), (d) PET (unannealed) (γ~45 mN m^{-1}), and (e) PI (γ~43 mN m^{-1}).

The LB-nTM printing method is also applicable for uniform, controlled, and large-area fabrication of graphene patterns as shown by the height profiles in Figure 4. The graphene ink was tailored to produce uniform height profiles for the graphene electrode pattern. Twenty sets of electrodes with spacings of 10 μm and 50 μm were printed on SiO_2 (Figure 14a, d). The height profiles and surface characteristics were measured by optical profilometry (OP), atomic force microscopy (AFM), and SEM. A 3D image of a single set of electrodes of both 10 μm and 50 μm spacings are shown in Figure 4b and 4e to visualize the high-resolution, uniform printing. The average height for electrodes with 10 μm spacing was 250 ± 11 nm, and for electrodes with 50 μm spacing was 238 ± 6 nm. While this depth is much greater than the height profile of the printed graphene electrodes, it can be varied accordingly by controlling the spin-coated thickness of the SU8 photoresist mixture prior to photolithography. Similarly, the height of the graphene electrodes can be increased by drawing additional layers of ink across the mold as demonstrated by Song *et al.* (2017).[43] Individual line profiles for a single pair of electrodes with 10 μm and 50 μm spacings are shown in Figure 14c,f, and the average heights for nine electrode sets are shown in Figure 4i. The surface roughness (Ra) of the printed electrodes with 10 μm and 50 μm spacings were measured to be 39 ± 2 nm and 41 ± 5 nm, respectively (average of 3 AFM scans for 10 μm x 10 μm surfaces). The AFM image (Figure 14g) shows the individual flakes of graphene, which contribute to the surface roughness of the electrodes. High-resolution SEM images of the graphene electrode surface are shown in Figure S4. The uniform edge of the electrode is evident in a tilted SEM image in Figure 14h, demonstrating the continuous packing of graphene flakes to form the printed pattern.

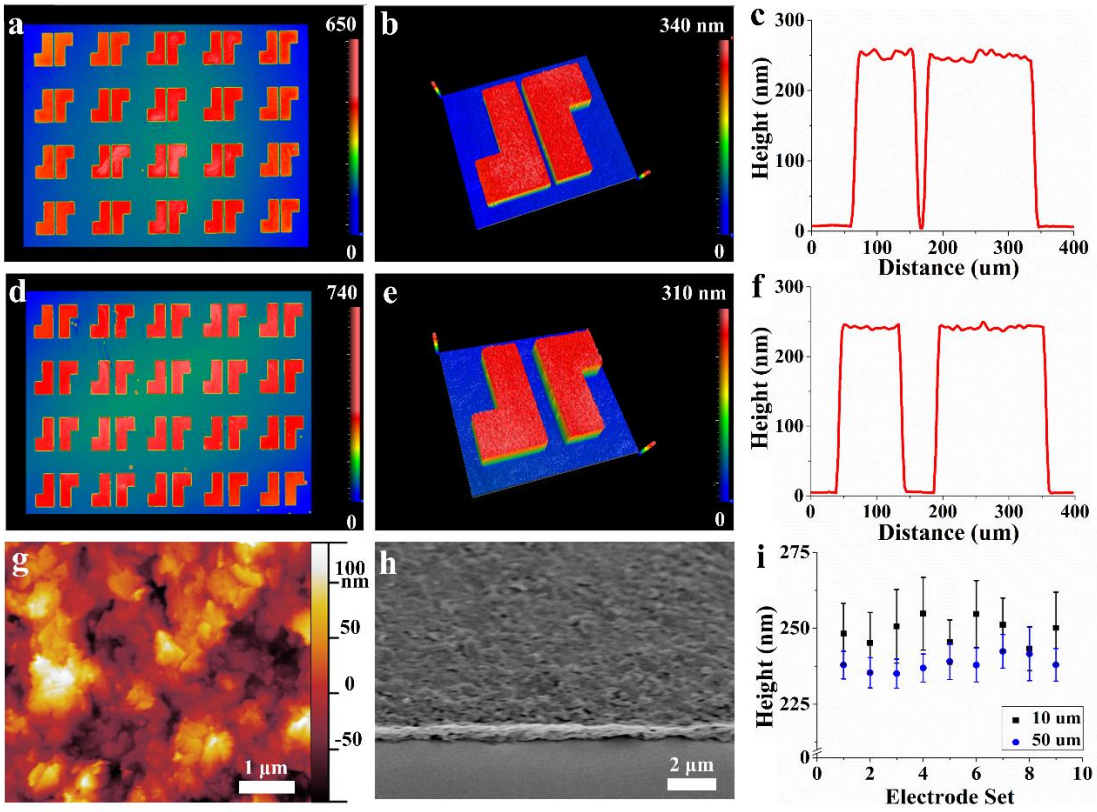

Figure 14. Height profile of graphene electrodes. OP image of twenty sets of printed electrodes with (a) 10 µm and (d) 50 µm spacing over a 2 mm x 2.5 mm area on SiO_2. The 3D image of single set of electrodes with (b) 10 µm and (e) 50 µm spacing. Line profile for electrode set with (c) 10 µm spacing, 250 ± 11 nm height, and (f) 50 µm spacing, 238 ± 6 nm height, corresponding to the 3D images. (g) AFM image of printed graphene electrode with surface roughness of 39 ± 2 nm and 41 ± 5 nm for 10 µm and 50 µm spacings, respectively. (h) Tilted SEM image of graphene electrode edge. (i) Electrode height for nine individual sets of graphene electrodes with 10 and 50 µm spacings.

To confirm residue-free printing, energy dispersive X-ray spectroscopy (EDS) was used to examine the 10 µm gap between a set of electrodes printed on SiO_2. In Figure 15, an SEM image and corresponding EDS spectrum are shown with the elements of carbon, oxygen, and silicon. The elemental mapping confirms the lack of carbon in the 10 µm gap between the electrodes, verifying graphene was only printed where desired.

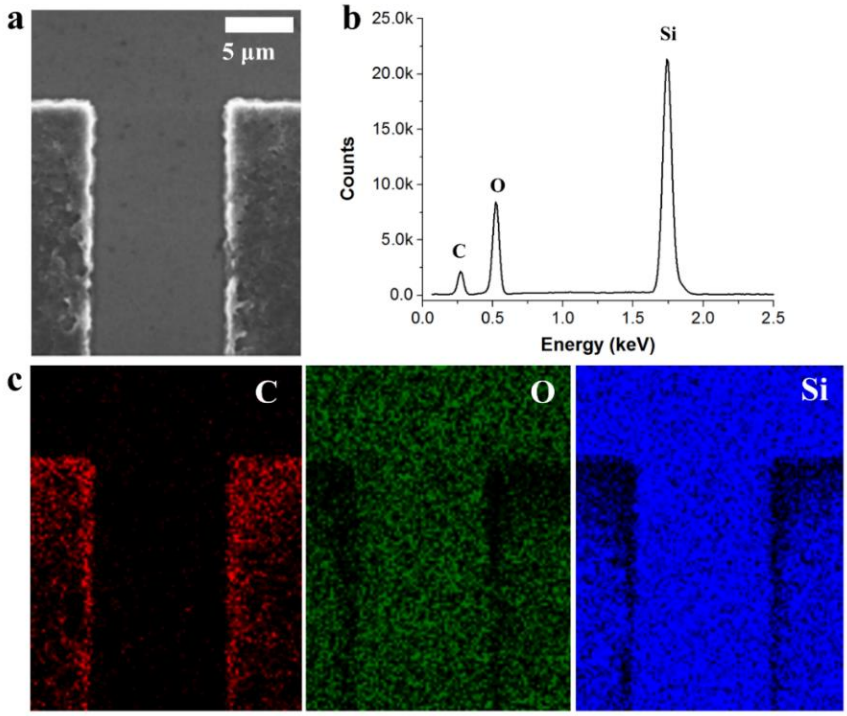

Figure 15. EDS spectrum of printed graphene. (a) SEM image of graphene electrodes on a SiO_2 substrate. (b) EDS spectrum showing elemental peaks from carbon, oxygen, and silicon. (c) Residue-free printing demonstrated by elemental mapping of C, O, and Si.

1.8 Organic Transistors and Inverters

The printed graphene electrodes were used to fabricate OFETs with rubrene (p-type) and PDIF-CN_2 (n-type) single-crystals, as shown in Figure 17b. Graphene electrodes were printed on highly doped Si with SiO_2 (300 nm), which served as the gate electrode and dielectric layer, respectively, of the transistor. The OFET devices were measured under ambient conditions, since rubrene and PDIF-CN_2 are both air-stable organic semiconductors.[64] The single-crystals were grown by PVT and placed over the graphene electrodes, as shown in Figure 16 below.

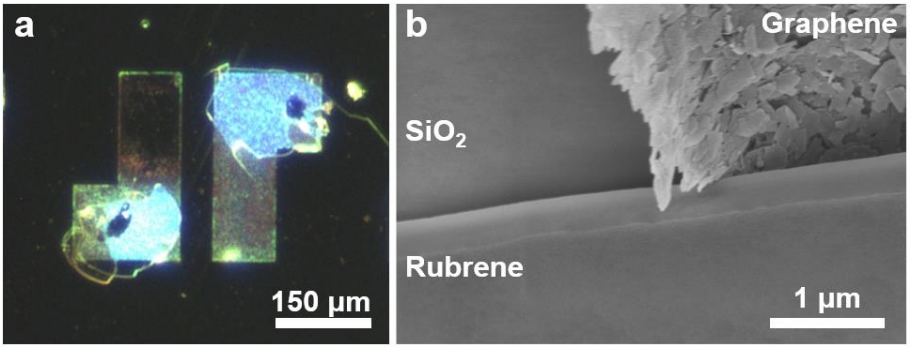

Figure 16. Rubrene single-crystal on graphene electrodes. (a) OM image of thin rubrene crystal over graphene electrodes after OFET measurement, (b) SEM image of rubrene crystal in contact with SiO_2 and graphene electrode.

The p-channel and n-channel electrical characteristics of these devices are shown in Figure 17c,d. The output curves shown in Figure 17d indicate well-resolved current modulation at large source-drain voltages (V_{ds}) as applied gate voltage (V_G) is increased. The transfer characteristics are shown in Figure 17c with a plot of both the log and the square root of the source-drain current (I_{ds}) as a function of V_G. As expected, a linear increase in the square root of I_{ds} as a function of V_G is demonstrated. The rubrene transistors exhibited a maximum mobility of 2.1 $cm^2\ V^{-1}\ s^{-1}$, a current on/off ratio of 10^6, and a threshold voltage of 0.02 V at a constant V_{ds} of -60 V. The PDIF-CN_2 devices showed a maximum mobility of 0.6 $cm^2\ V^{-1}\ s^{-1}$, a current on/off ratio of 10^7, and a threshold voltage of 5.1 V at a constant V_{ds} of 60 V. Mobilities from six individual single-crystal devices ranged from 0.2 to 2.1 $cm^2\ V^{-1}\ s^{-1}$ for rubrene and 0.1 to 0.6 $cm^2\ V^{-1}\ s^{-1}$ for PDIF-CN_2. These values were calculated from the saturation region using Equation 1, where µ is mobility, C is the dielectric capacitance, W is the channel width, L is the channel length, and V_{th} is threshold voltage.

$$I_{DS} = \mu C \left(\frac{W}{2L}\right)(V_G - V_{th})^2 \qquad [3]$$

Device performance was further investigated by measuring the mobility as a function of different V_{ds} (Figure 17e). The mobility was saturated above $|V_{ds}|$ = 30 V for both rubrene and PDIF-CN_2, suggesting that the mobility values extracted at reasonably large V_{ds} values are no longer affected by contact resistance. In Figure 17f, the dependence of mobility on V_G is plotted using Equation 2.

$$\mu = \frac{2\,L}{W\,C}\left(\frac{\delta\, I_{ds}^{\frac{1}{2}}}{\delta\, V_G}\right)^2 \qquad [4]$$

It is observed that at higher $|V_G|$, the mobility becomes V_G independent. In comparison, the mobility is dependent on V_G at low V_{ds} values, which is explained by the fact that contact resistance increases at lower V_{ds}.[65] We note that for rubrene, the mobility is contact-limited at V_{ds} below -25 V. For PDIF-CN_2, the device is contact-limited at about +30 V and below. Podzorov et al. demonstrated the contact resistance effect by conducting two-probe and four-probe measurements and concluded that two-probe mobility measurements, as presented here, can be considered "contact-corrected" at sufficiently high source-drain voltages.[65] As demonstrated, our two-probe results are consistent with their findings.

Finally, we have compared single-crystal rubrene devices fabricated on gold electrodes with the results of our work. Gold electrodes (4.4-5.1) offers a similar work function as printed graphene electrodes (4.4-4.5), and the device in the cited study also uses a SiO_2 dielectric layer on a Si gate electrode and was measured under ambient conditions.[66] For these devices, the gold/rubrene device demonstrated a mobility of 2.6 cm^2/V s. While the mobility values cannot be directly compared due to differences in work function and electrode material, we demonstrate that our results fall within the expected range for such device.

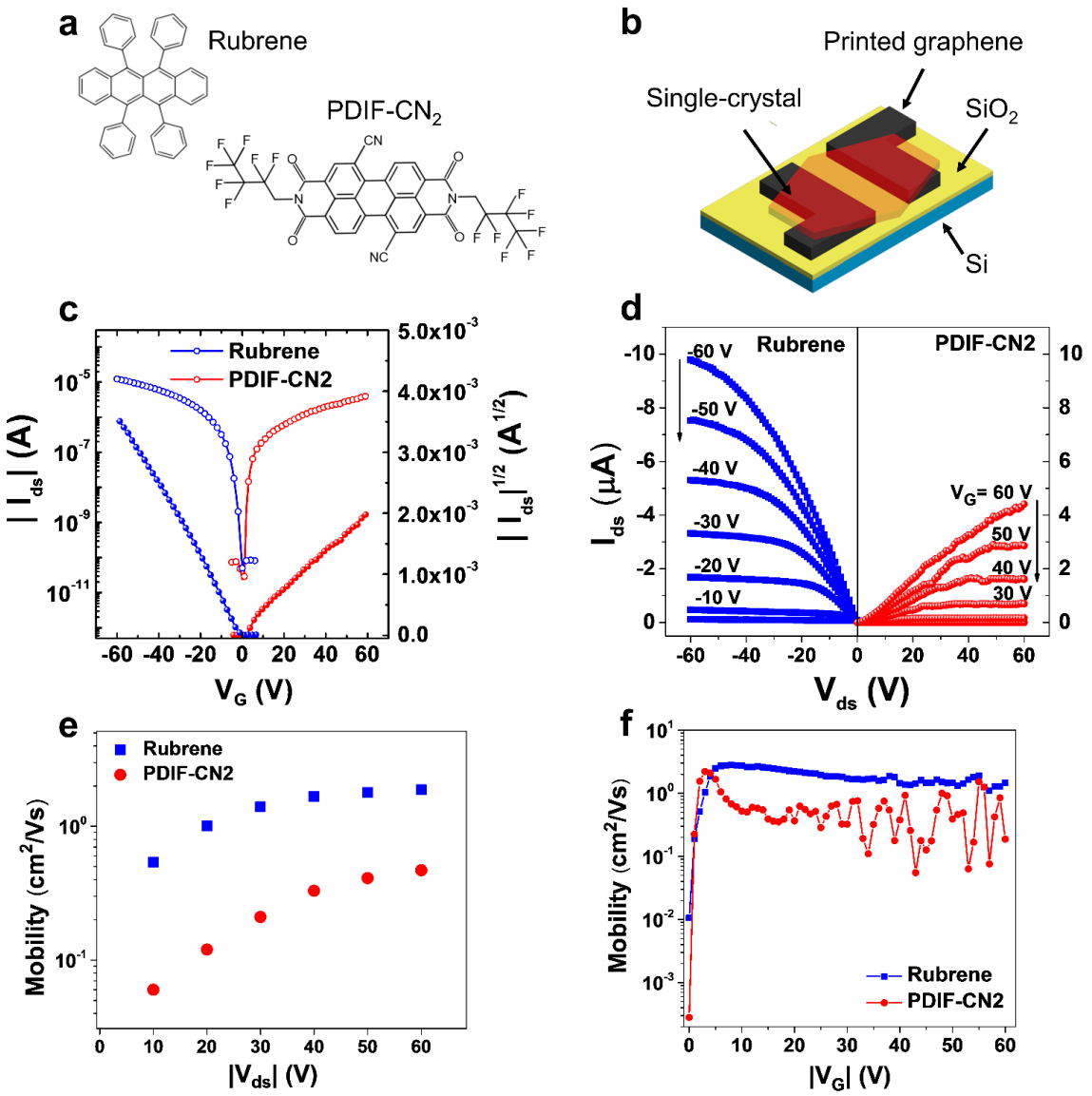

Figure 17. Device characteristics of rubrene and PDIF-CN_2 OFETs using printed graphene electrodes. (a) Rubrene and PDIF-CN_2 chemical structures. (b) Schematic of a single-crystal transistor using graphene as source/drain electrodes with a 50 μm channel length in bottom-gate, bottom-contact geometry on SiO_2/Si substrate. (c) Transfer characteristics at V_{ds} = -60 V for rubrene and V_{ds} = 60 V for PDIF-CN_2 showing excellent characteristics and good linearity over a broad V_G range. (d) Output characteristics for gate biases between -60 V ≤ V_G ≤ -10 V varied in 10 V steps for rubrene and 10 V ≤ V_G ≤ 60 V for PDIF-CN_2. (e) Mobility versus V_{ds} for rubrene and PDIF-CN_2. (f) Plot of mobility versus V_G at constant V_{ds} of -60 V for rubrene and 60 V for PDIF-CN_2. V_G: gate voltage, V_{ds}: source-drain voltage, I_{ds}: source-drain current.

For single-crystal PDIF-CN_2 OFETs, there are no comparable studies for devices fabricated with a SiO_2 dielectric layer. It has been shown that using different dielectric layers will significantly affect the mobility of single-crystal devices.[67] While we cannot draw a direct comparison due to this difference, the mobility of our PDIF-CN_2/printed graphene system ranged from 0.1 to 0.6 $cm^2\ V^{-1}\ s^{-1}$, which is comparable to the 0.8 to 3 $cm^2\ V^{-1}\ s^{-1}$ mobility reported for single-crystal PDIF-CN_2 OFETs on gold electrodes measured under ambient conditions.[64] The higher mobility reported in this study may be a result of their PMMA/SiO_2 dielectric where the polymer layer prevented the effects of surface bound hydroxyl groups on SiO_2, which can act as charge traps.[68] Additionally, Chinanese *et al.* recently showed that PDIF-CN_2/gold interfaces actually hinder charge injection and allow for parasitic contact effects.[69] In comparison, exfoliated graphene flakes within PDIF-CN_2 films resulted in a three orders of magnitude increase in the mobility of PDIF-CN_2 OFETs.[70] We assume a similar effect may be seen with our graphene electrodes which are also composed of graphene flakes.

Lastly, printed graphene electrodes offer several attractive advantages over commonly used gold or silver electrodes for OFETs. In particular, gold electrodes are expensive to fabricate using solution-processable methods. While silver electrodes are low-cost and compatible with printed techniques, they require high-temperature annealing and show poor stability due to oxidation. Several studies using both inorganic and organic semiconductors have demonstrated superior device performance of graphene ink electrodes compared with printed silver electrodes.[43,71] This is because these graphene ink electrodes allow for good stability and low contact resistance.[36,42] Finally, graphene electrodes also provide better charge injection than metal electrodes due to the tunability

of the work function to be similar to the organic semiconductor, and also offer the ability for selective growth of organic semiconductors.[72]

Finally, as a demonstration of an integrated circuit, we fabricated complementary inverters using p-type rubrene and n-type PDIF-CN_2. The inverter configuration consisted of single-crystals placed on printed graphene electrodes, as shown in Figure 18a. Well-resolved voltage transfer characteristics are demonstrated in Figure 18b over a supply voltage (V_{dd}) range of -80 to 80 V. Depending on the polarity of V_{dd}, one can observe defined transfer characteristics in the first and third quadrants of the output (V_{out}) versus input (V_{in}) voltage diagram. These results show symmetric V_{out}-V_{in} switching at the midpoint voltage ($V_{dd}/2$), as shown graphically at the intersection of the transfer curves and the line of V_{out} = V_{in}. This symmetry is a result of balanced mobilities, threshold voltages, and identical geometric factors, including the dielectric layer, channel width, and channel length of the inverter. Lastly, Figure 18c shows the derivative of the static transfer characteristics from Figure 7b with gains as large as 50 for V_{dd}=-80 V.

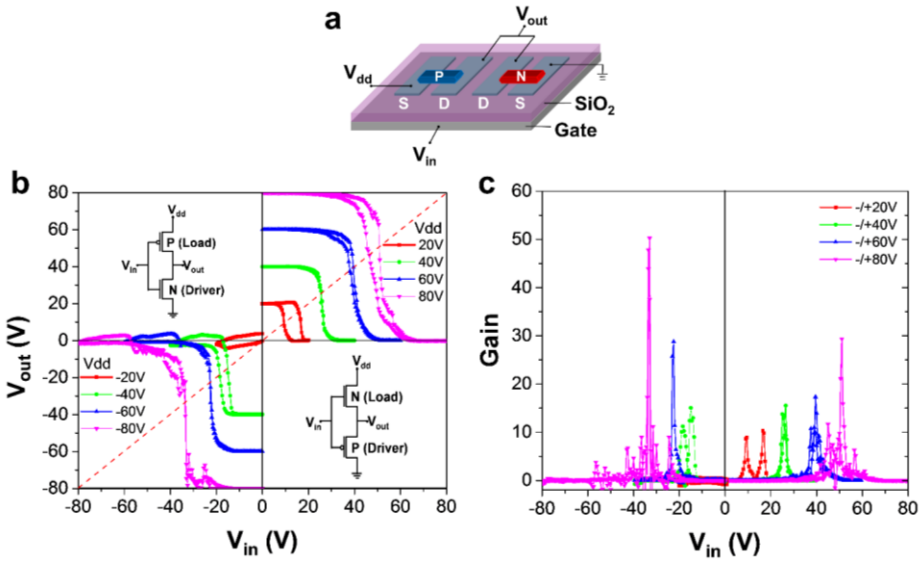

Figure 18. Structure and static transfer characteristics of the rubrene/PDIF-CN_2 complementary inverter. (a) Illustration of the complementary inverter with graphene

source and drain electrodes. (b) Voltage transfer characteristics indicating symmetric switching at the midpoint voltage. (c) The plot of gain versus V_{in}, indicating gains as large as 50 for V_{dd} = -80 V.

1.9 Conclusion

In conclusion, we have demonstrated the direct printing of high-resolution graphene patterns and shown their use for source and drain electrodes in single-crystal OFETs and inverters. LB-nTM was used to fabricate uniform and precise graphene electrodes over large-areas, as well as graphene squares, dots, and lines. The resolution of printed graphene patterns ranged between 300 μm to ~310 nm, demonstrating the high-resolution printing capability of LB-nTM. Graphene electrodes were printed on a variety of substrates with surface energies from ~43 to 73 mN m^{-1}, confirming the versatility of this technique. Additionally, LB-nTM of graphene provides an alternative route for the fabrication of highly conductive electrodes and circuitry, which is not reliant on chemical etching or hazardous solvents. Using printed graphene electrodes, we demonstrated organic single-crystal OFETs with rubrene and PFID-CN_2 with maximum mobilities of 2.1 cm^2 V^{-1} s^{-1} and 0.6 cm^2 V^{-1} s^{-1}, respectively, as well as inverters with gains of ~50. In this way, direct printing of graphene by LB-nTM allows for an inexpensive, solution-based method for high-resolution, scalable manufacturing for printed electronics.

1.10 References

(1) Das, R.; Ghaffarzadeh, K.; He, X. Printed, Organic & Flexible Electronics Forecasts, Players & Opportunities 2017-2027. *IDTechEx Res.* **2017**, 1–329.

(2) Søndergaard, R. R.; Hösel, M.; Krebs, F. C. Roll-to-Roll Fabrication of Large Area Functional Organic Materials. *J. Polym. Sci. Part B Polym. Phys.* **2013**, *51* (1), 16–34.

(3) Schwartz, E. Roll to Roll Processing for Flexible Electronics. *Roll to Roll Process. Flex. Electron.* **2006**, 1–24.

(4) Koidis, C.; Logothetidis, S.; Ioakeimidis, A.; Laskarakis, A.; Kapnopoulos, C. Key Factors to Improve the Efficiency of Roll-to-Roll Printed Organic Photovoltaics. *Org. Electron. physics, Mater. Appl.* **2013**, *14* (7), 1744–1748.

(5) Ross, I. M. The Invention of the Transistor. *Proc. IEEE* **1998**, *86* (1), 7–28.

(6) Samsung. Samsung Starts Industry's First Mass Production of System-on-Chip with 10-Nanometer FinFET Technology. **2016**, Oct-16.

(7) Ferain, I.; Colinge, C. a.; Colinge, J.-P. Multigate Transistors as the Future of Classical Metal–oxide–semiconductor Field-Effect Transistors. *Nature* **2011**, *479* (7373), 310–316.

(8) Yan, H.; Chen, Z.; Zheng, Y.; Newman, C.; Quinn, J. R.; Dötz, F.; Kastler, M.; Facchetti, A. A High-Mobility Electron-Transporting Polymer for Printed Transistors. *Nature* **2009**, *457* (7230), 679–686.

(9) Beaulieu, M. R.; Baral, J. K.; Hendricks, N. R.; Tang, Y.; Briseno, A. L.; Watkins, J. J. Solution Processable High Dielectric Constant Nanocomposites Based on zro2 Nanoparticles for Flexible Organic Transistors. *ACS Appl. Mater. Interfaces* **2013**, *5* (24), 13096–13103.

(10) Wang, Z.; Cook, A. P.; Yang, X.; Liu, Z.; Yu, Q.; Chen, M. Y. Graphene-Based Flexible Field Effect Transistor with Inkjet Printed Silver Electrodes. **2013**, 635–637.

(11) Sirringhaus, H. 25th Anniversary Article: Organic Field-Effect Transistors: The Path beyond Amorphous Silicon. *Adv. Mater.* **2014**, *26* (9), 1319–1335.

(12) Gomes, H. L. Organic Field Effect Transistors. *Org. Print. Electron. - Fundam. Appl.* **2016**, 1–26.

(13) Gao, Y.; Shao, Y.; Yan, L.; Li, H.; Su, Y.; Meng, H.; Wang, X. Efficient Charge Injection in Organic Field-Effect Transistors Enabled by Low-Temperature Atomic Layer Deposition of Ultrathin VOxInterlayer. *Adv. Funct. Mater.* **2016**, *26*

(25), 4456–4463.

(14) Facchetti, A.; Yoon, M.-H.; Marks, T. J. Gate Dielectrics for Organic Field-Effect Transistors: New Opportunities for Organic Electronics. *Adv. Mater.* **2005**, *17* (14), 1705–1725.

(15) Campos, A.; Riera-Galindo, S.; Puigdollers, J.; Mas-Torrent, M. Reduction of Charge Traps and Stability Enhancement in Solution-Processed Organic Field-Effect Transistors Based on a Blended N-Type Semiconductor. *ACS Appl. Mater. Interfaces* **2018**, *10* (18), 15952–15961.

(16) Bao, Z.; Locklin, J. Organic Field Effect Transistors. **2007**, 1–33.

(17) Wu, Y.; Li, Y.; Ong, B. S.; Liu, P.; Gardner, S.; Chiang, B. High-Performance Organic Thin-Film Transistors with Solution-Printed Gold Contacts. *Adv. Mater.* **2005**, *17* (2), 184–187.

(18) Yi, S. M.; Jin, S. H.; Lee, J. D.; Chu, C. N. Fabrication of a High-Aspect-Ratio Stainless Steel Shadow Mask and Its Application to Pentacene Thin-Film Transistors. *J. Micromechanics Microengineering* **2005**, *15* (2), 263–269.

(19) Kim, S.; Sojoudi, H.; Zhao, H.; Mariappan, D.; McKinley, G. H.; Gleason, K. K.; Hart, A. J. Ultrathin High-Resolution Flexographic Printing Using Nanoporous Stamps. *Sci. Adv.* **2016**, *2*, 1–11.

(20) Traub, M. C.; Longsine, W.; Truskett, V. N. Advances in Nanoimprint Lithography. *Annu. Rev. Chem. Biomol. Eng.* **2016**, *7* (1), 583–604.

(21) Park, S. M.; Liang, X.; Harteneck, B. D.; Pick, T. E.; Hiroshiba, N.; Wu, Y.; Helms, B. A.; Olynick, D. L. Sub-10 Nm Nanofabrication via Nanoimprint Directed Self-Assembly of Block Copolymers. *ACS Nano* **2011**, *5* (11), 8523–8531.

(22) Chou, S. Y.; Krauss, P. R.; Renstrom, P. J. Imprint Lithography with 25 Nm Resolution. *Science.* **1996**, *272* (5258), 85–87.

(23) Tabatabai, A.; Fassler, A.; Usiak, C.; Majidi, C. Liquid-Phase Gallium − Indium Alloy Electronics with Microcontact Printing. **2013**.

(24) Blümel, A.; Klug, A.; Eder, S.; Scherf, U.; Moderegger, E.; List, E. J. W. Micromolding in Capillaries and Microtransfer Printing of Silver Nanoparticles as Soft-Lithographic Approach for the Fabrication of Source/drain Electrodes in Organic Field-Effect Transistors. *Org. Electron. physics, Mater. Appl.* **2007**, *8* (4), 389–395.

(25) Beaulieu, M. R.; Hendricks, N. R.; Watkins, J. J. Large-Area Printing of Optical Gratings and 3D Photonic Crystals Using Solution-Processable Nanoparticle/Polymer Composites. *ACS Photonics* **2014**, *1* (9), 799–805.

(26) Hwang, J. K.; Cho, S.; Dang, J. M.; Kwak, E. B.; Song, K.; Moon, J.; Sung, M. M. Direct Nanoprinting by Liquid-Bridge-Mediated Nanotransfer Moulding. *Nat. Nanotechnol.* **2010**, *5* (10), 742–748.

(27) Cho, B.; Park, K. S.; Baek, J.; Oh, H. S.; Koo Lee, Y. E.; Sung, M. M. Single-Crystal poly(3,4-Ethylenedioxythiophene) Nanowires with Ultrahigh Conductivity. *Nano Lett.* **2014**, *14* (6), 3321–3327.

(28) Kumar, S. Liquid Transfer in Printing Processes: Liquid Bridges with Moving Contact Lines. *Annu. Rev. Fluid Mech.* **2015**, *47* (1), 67–94.

(29) Weiss, N. O.; Zhou, H.; Liao, L.; Liu, Y.; Jiang, S.; Huang, Y.; Duan, X. Graphene: An Emerging Electronic Material. *Adv. Mater.* **2012**, *24* (43), 5782–5825.

(30) Zeng, M.; Xiao, Y.; Liu, J.; Lu, W.; Fu, L. Controllable Fabrication of Nanostructured Graphene Towards Electronics. *Adv. Electron. Mater.* **2016**, *2* (4), 1500456.

(31) Field-effect, O. S. C.; Liu, W.; Jackson, B. L.; Zhu, J.; Miao, C.; Park, Y.; Sun, K.; Woo, J.; Xie, Y. Large Scale Pattern Graphene Electrode for High Performance in Transparent. **2010**, *4* (7), 3927–3932.

(32) Dua, V.; Surwade, S. P.; Ammu, S.; Agnihotra, S. R.; Jain, S.; Roberts, K. E.; Park, S.; Ruoff, R. S.; Manohar, S. K. All-Organic Vapor Sensor Using Inkjet-Printed Reduced Graphene Oxide. *Angew. Chemie - Int. Ed.* **2010**, *49* (12), 2154–2157.

(33) Yi, M.; Shen, Z. A Review on Mechanical Exfoliation for the Scalable Production of Graphene. *J. Mater. Chem. A* **2015**, *3* (22), 11700–11715.

(34) Lin, J.; Peng, Z.; Liu, Y.; Ruiz-Zepeda, F.; Ye, R.; Samuel, E. L. G.; Yacaman, M. J.; Yakobson, B. I.; Tour, J. M. Laser-Induced Porous Graphene Films from Commercial Polymers. *Nat. Commun.* **2014**, *5* (5714), 1–8.

(35) Liang, Y. T.; Hersam, M. C. Highly Concentrated Graphene Solutions via Polymer Enhanced Solvent Exfoliation and Iterative Solvent Exchange. *J. Am. Chem. Soc.* **2010**, *132* (50), 17661–17663.

(36) Hyun, W. J.; Secor, E. B.; Rojas, G. A.; Hersam, M. C.; Francis, L. F.; Frisbie, C. D. All-Printed, Foldable Organic Thin-Film Transistors on Glassine Paper. *Adv. Mater.* **2015**, *27* (44), 7058–7064.

(37) Li, L.; Secor, E. B.; Chen, K. S.; Zhu, J.; Liu, X.; Gao, T. Z.; Seo, J. W. T.; Zhao, Y.; Hersam, M. C. High-Performance Solid-State Supercapacitors and Microsupercapacitors Derived from Printable Graphene Inks. *Adv. Energy Mater.* **2016**, *6* (20), 1–8.

(38) Gonzalez Arellano, D. L.; Lee, H.; Secor, E. B.; Burnett, E. K.; Hersam, M. C.; Watkins, J. J.; Briseno, A. L. Graphene Ink as a Conductive Templating Interlayer for Enhanced Charge Transport of C60-Based Devices. *ACS Appl. Mater. Interfaces* **2016**, *8* (43), 29594–29599.

(39) Jakus, A. E.; Secor, E. B.; Rutz, A. L.; Jordan, S. W.; Hersam, M. C.; Shah, R. N. Three-Dimensional Printing of High-Content Graphene Sca Ff Olds for Electronic and Biomedical Applications. *ACS Nano* **2015**, *9* (4), 4636–4648.

(40) Secor, E. B.; Prabhumirashi, P. L.; Puntambekar, K.; Geier, M. L.; Hersam, M. C. Inkjet Printing of High Conductivity , Flexible Graphene Patterns. *J. Phys. Chem. Lett.* **2013**, *4*, 1347–1351.

(41) Secor, E. B.; Lim, S.; Zhang, H.; Frisbie, C. D.; Francis, L. F.; Hersam, M. C. Gravure Printing of Graphene for Large-Area Flexible Electronics. *Adv. Mater.* **2014**, *26*, 4533–4538.

(42) Hyun, W. J.; Secor, E. B.; Hersam, M. C.; Frisbie, C. D.; Francis, L. F. High-Resolution Patterning of Graphene by Screen Printing with a Silicon Stencil for Highly Flexible Printed Electronics. *Adv. Mater.* **2015**, *27* (1), 109–115.

(43) Song, D.; Mahajan, A.; Secor, E. B.; Hersam, M. C.; Francis, L. F.; Frisbie, C. D. High-Resolution Transfer Printing of Graphene Lines for Fully Printed, Flexible Electronics. *ACS Nano* **2017**, *11* (7), 7431.

(44) Kang, S. J.; Lee, G.-H.; Yu, Y.-J.; Zhao, Y.; Kim, B.; Watanabe, K.; Taniguchi, T.; Hone, J.; Kim, P.; Nuckolls, C. Organic Field Effect Transistors Based on Graphene and Hexagonal Boron Nitride Heterostructures. *Adv. Funct. Mater.* **2014**, *24*, 5157–5163.

(45) Pak, Y.; Jeong, H.; Lee, K. H.; Song, H.; Kwon, T.; Park, J.; Park, W.; Jeong, M. S.; Lee, T.; Seo, S.; Jung, G. Y. Large-Area Fabrication of Periodic Sub-15 Nm-Width Single-Layer Graphene Nanorings. *Adv. Mater.* **2013**, *25* (2), 199–204.

(46) Chao, W.; Keith, J. M.; Zengli, F.; Wen-Di, L.; Stephen, Y. C. Printing of Sub-20 Nm Wide Graphene Ribbon Arrays Using Nanoimprinted Graphite Stamps and Electrostatic Force Assisted Bonding. *Nanotechnology* **2011**, *22* (44), 445301.

(47) Liang, X.; Jung, Y. S.; Wu, S.; Ismach, A.; Olynick, D. L.; Cabrini, S.; Bokor, J. Formation of Bandgap and Subbands in Graphene Nanomeshes with Sub-10 Nm Ribbon Width Fabricated via Nanoimprint Lithography. *Nano Lett.* **2010**, *10* (7), 2454–2460.

(48) Zhang, J.; Hu, P.; Zhang, R.; Wang, X.; Yang, B.; Cao, W.; Li, Y.; He, X.; Wang, Z.; O'Neill, W. Soft-Lithographic Processed Soluble Micropatterns of Reduced Graphene Oxide for Wafer-Scale Thin Film Transistors and Gas Sensors. *J. Mater. Chem.* **2012**, *22*, 714.

(49) Liu, S.; Wang, W. M.; Briseno, A. L.; Mannsfeld, S. C. B.; Bao, Z. Controlled Deposition of Crystalline Organic Semiconductors for Field-Effect-Transistor Applications. *Adv. Mater.* **2009**, *21* (12), 1217–1232.

(50) Jackman, R. J.; Duffy, D. C.; Ostuni, E.; Willmore, N. D.; Whitesides, G. M. Fabricating Large Arrays of Microwells with Arbitrary Dimensions and Filling Them Using Discontinuous Dewetting. *Anal. Chem.* **1998**, *70* (11), 2280–2287.

(51) Park, K. S.; Cho, B.; Baek, J.; Hwang, J. K.; Lee, H.; Sung, M. M. Single-Crystal Organic Nanowire Electronics by Direct Printing from Molecular Solutions. *Adv. Funct. Mater.* **2013**, *23* (38), 4776–4784.

(52) Lee, B. H.; Cho, Y. H.; Lee, H.; Lee, K. D.; Kim, S. H.; Sung, M. M. High-Resolution Patterning of Aluminum Thin Films with a Water-Mediated Transfer Process. *Adv. Mater.* **2007**, *19* (13), 1714–1718.

(53) National Bureau of Standards, United States Dept of Commerce. Table of Dielectric Constants of Pure Liquids; 1994.

(54) Khattab, I. S.; Bandarkar, F.; Fakhree, M. A. A.; Jouyban, A. Density, Viscosity, and Surface Tension of Water+ethanol Mixtures from 293 to 323K. *Korean J. Chem. Eng.* **2012**, *29* (6), 812–817.

(55) Vargaftik, N. B.; Volkov, B. N.; Voljak, L. D. International Tables of the Surface Tension of Water. *J. Phys. Chem. Ref. Data* **1983**, *12* (3), 817–820.

(56) Chen, X.; Weibel, J. A.; Garimella, S. V. Water and Ethanol Droplet Wetting Transition during Evaporation on Omniphobic Surfaces. *Sci. Rep.* **2015**, *5* (October), 1–11.

(57) Tsetseris, L.; Pantelides, S. T. Oxygen and Water-Related Impurities in C60 Crystals: A Density-Functional Theory Study. *Phys. Rev. B - Condens. Matter Mater. Phys.* **2010**, *82* (4), 1–5.

(58) Capello, C.; Fischer, U.; Hungerbühler, K. What Is a Green Solvent? A Comprehensive Framework for the Environmental Assessment of Solvents. *Green Chem.* **2007**, *9* (9), 927.

(59) Yin, Z.; Huang, Y.; Bu, N.; Wang, X.; Xiong, Y. Inkjet Printing for Flexible Electronics: Materials, Processes and Equipments. *Chinese Sci. Bull.* **2010**, *55* (30), 3383–3407.

(60) Janssen, D.; De Palma, R.; Verlaak, S.; Heremans, P.; Dehaen, W. Static Solvent Contact Angle Measurements, Surface Free Energy and Wettability Determination of Various Self-Assembled Monolayers on Silicon Dioxide. *Thin Solid Films* **2006**, *515* (4), 1433–1438.

(61) Shafrin, E. G.; Zisman, W. A. Effect of Adsorbed Water on the Spreading of

Organic Liquids on Soda-Lime Glass. *J. Am. Ceram. Soc.* **1967**, *50* (9), 478–484.

(62) van Osch, T. H. J.; Perelaer, J.; de Laat, A. W. M.; Schubert, U. S. Inkjet Printing of Narrow Conductive Tracks on Untreated Polymeric Substrates. *Adv. Mater.* **2008**, *20* (2), 343–345.

(63) Secor, E. B.; Ahn, B. Y.; Gao, T. Z.; Lewis, J. A.; Hersam, M. C. Rapid and Versatile Photonic Annealing of Graphene Inks for Flexible Printed Electronics. *Adv. Mater.* **2015**, *27* (42), 6683–6688.

(64) Molinari, A. S.; Alves, H.; Chen, Z.; Facchetti, A.; Morpurgo, A. F. High Electron Mobility in Vacuum and Ambient for PDIF-CN $_2$ Single-Crystal Transistors. *J. Am. Chem. Soc.* **2009**, *131* (7), 2462–2463.

(65) Podzorov, V.; Sysoev, S. E.; Loginova, E.; Pudalov, V. M.; Gershenson, M. E. Single-Crystal Organic Field Effect Transistors with the Hole Mobility ~8 cm2/V S. *Appl. Phys. Lett.* **2003**, *83* (17), 3504.

(66) Briseno, A. L.; Tseng, R. J.; Ling, M. M.; Falcao, E. H. L.; Yang, Y.; Wudl, F.; Bao, Z. High-Performance Organic Single-Crystal Transistors on Flexible Substrates. *Adv. Mater.* **2006**, *18* (17), 2320–2324.

(67) Stassen, A. F.; De Boer, R. W. I.; Losad, N. N.; Morpurgo, A. F. Influence of the Gate Dielectric on the Mobility of Rubrene Single-Crystal Field-Effect Transistors. *Appl. Phys. Lett.* **2004**, *85* (17), 3899–3901.

(68) Kiron Prabha Rajeev, Charles Opoku, Vlad Stolojan, Marios Constantinou, M. S. Effect of Nanowire-Dielectric Interface on the Hysteresis of Solution Processed Silicon Nanowire FETs. *Nanosci. Nanoeng.* **2017**, *5* (2), 17–24.

(69) Chianese, F.; Chiarella, F.; Barra, M.; Carella, A.; Cassinese, A. Scanning Kelvin Probe Microscopy Investigation of the Contact Resistances and Charge Mobility in N-Type PDIF-CN2thin-Film Transistors. *Org. Electron. physics, Mater. Appl.* **2018**, *52* (August 2017), 206–212.

(70) Pathipati, S. R.; Pavlica, E.; Schlierf, A.; El Gemayel, M.; Samorì, P.; Palermo, V.; Bratina, G. Graphene-Induced Enhancement of N-Type Mobility in Perylenediimide Thin Films. *J. Phys. Chem. C* **2014**, *118* (43), 24819–24826.

(71) Secor, E. B.; Smith, J.; Marks, T. J.; Hersam, M. C. High-Performance Inkjet-Printed Indium-Gallium-Zinc-Oxide Transistors Enabled by Embedded, Chemically Stable Graphene Electrodes. *ACS Appl. Mater. Interfaces* **2016**, *8* (27).

(72) Acevedo-Cartagena, D. E.; Zhu, J.; Trabanino, E.; Pentzer, E.; Emrick, T.; Nonnenmann, S. S.; Briseno, A. L.; Hayward, R. C. Selective Nucleation of poly(3-Hexyl Thiophene) Nanofibers on Multilayer Graphene Substrates. *ACS Macro Lett.* **2015**, *4* (5), 483–487.

CHAPTER 2

WEARABLE MICROFLUIDIC ELECTROWETTING VALVES

Skin-compatible, low-cost, and scalable microfluidic valving systems must be integrated with sweat sensing devices for continuous assessment of temporal and chemical biomarker variation. We demonstrate the fabrication of inkjet-printed electrowetting valves produced directly onto a skin adhesive and driven by fast capillary action. The valve consists of two conductive silver electrodes printed on a flexible hydrophilic substrate. The first electrode remains hydrophilic, while the second is modified with a dielectric hydrophobic monolayer to prevent fluid flow. This hydrophilicity is decreased using an applied potential, irreversibly opening the valve. Wearable electrowetting valves demonstrated fast and reliable actuation at 200 μm to 2 mm electrode spacings using applied voltages as low as 1 V, avoiding electrolysis of water. Inkjet-printing conditions of the valve were optimized to prevent the flow of artificial sweat for over six hours. While these valves require no external moving parts, multiple valves would necessitate larger space dimensions on a sweat sensing device. To reduce the overall size footprint, a single connected electrode was used for charge injection of multiple valves. Finally, valves were successfully integrated into a flexible wearable patch with individual absorbent pads for sweat collection. These solution-processable, disposable, and low voltage valves offer exciting opportunities for inexpensive and noninvasive personal sweat monitoring.

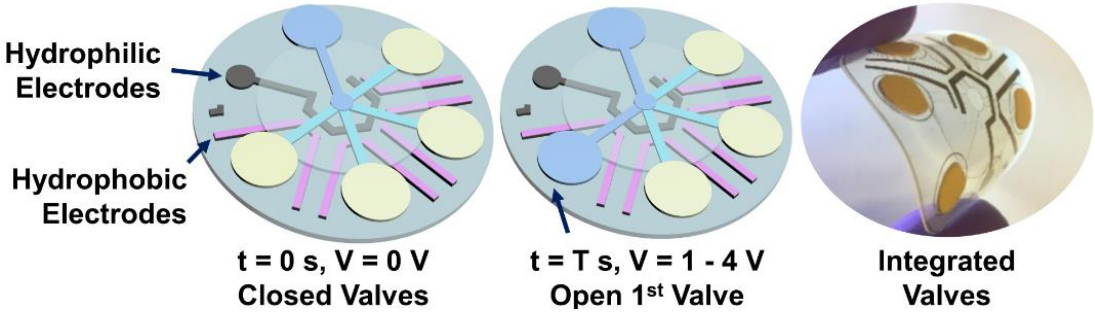

Figure 19. Schematic of wearable electrowetting valve patch in closed position (Left), with one valve opened (Middle), and an optical image of the fabricated device in a bent position.

2.1 Introduction

The field of microfluidics centers on fluid flow at the microscale for a large variety of applications, such as biosensors,[1] chemical synthesis,[2] protein crystallization,[3] and cell cultures.[4] Capillary force within the microchannel is commonly used to manipulate the behavior, flow, and direction of fluid transport. This technique provides for an inexpensive and simple microfluidics platform, which is applicable to many substrates from glass to plastic to paper.[5] Pregnancy tests and glucose test strips are two examples of highly successful commercial products that rely on capillary force-driven paper microfluidics. The success of these two point-of-care devices is largely due to their low-cost, flexible substrates, and user-friendly design. In comparison, expensive inkjet-printing cartridges are the only plastic-based microfluidic device with large-scale commercial success to date. To develop inexpensive diagnostic devices to detect more complex proteins and biomolecules, a simple and easy-to-use microfluidic valve to control fluid flow is necessary within capillary force-driven systems.[6]

Microfluidic valves are responsible for regulating fluid flow within a microchannel. The design of the valve dictates the interaction of liquids in a controllable

manner within nanoscale or microscale architecture. Two types of microfluidic valving systems are active valves, which require an external stimulus to function, and passive valves, which use surface chemistry to direct flow.[7] Some examples of valves include pneumatic valves,[8] electrostatic valves,[9] bubble-based valves,[10] capillary burst valves,[11] and time-delayed valves, which are discussed in greater detail below.[12] Many of these systems are not ideal for a point-of-care device, since they require multiple processing steps, use external moving parts, and are costly to scale-up on flexible substrates.[13]

In comparison, electrowetting valves have the potential to be a low-cost, user-friendly, portable, and reliable microfluidic valving system with applications in point-of-care devices. The valve uses the principle of electrowetting-on-a-dielectric, where the hydrophobicity of a thin dielectric insulator can be tuned to be hydrophilic by applying a low voltage. A pair of parallel, hydrophilic silver electrodes are inkjet-printed orthogonal to a microfluidic channel. One electrode is modified with a hydrophobic monolayer, while the other remains hydrophilic. The hydrophobic electrode will prevent liquid flow within the microchannel until voltage is applied across the electrodes, irreversibly opening the valve.[14] Current literature shows that electrowetting valves can be printed on a variety of paper and plastic substrates, demonstrating the versatility of this microfluidic valve and application for biological sensing and diagnostics.

2.2 Microfluidic Valves

In the field of microfluidic devices, one of the key aspects is the research and development of controllable microfluidic valves to direct flow of fluids within channels. A valve can be defined as a mechanism that is responsible for the regulation of fluid,

such as liquids and gases, or the direction of pressure and are commonly used to control flow in engineering systems. Similarly, for microfluidic devices, the design of the microfluidic valve dictates the ability of the microfluidic device to function in situations that require the interaction of two or more fluids in a timed manner.[7]

The history of microfluidic devices starts with a gas sensor system developed at Imperial College by Andreas Mann in the 1970s; however, research into the design of the microfluidic valve did not commence until the late 1990s. This was largely due to the introduction of soft lithographical techniques developed in Professor George Whitesides's group using polydimethylsiloxane (PDMS). From this material, soft elastomeric molds can be easily fabricated, allowing a large variety of microfluidic devices to be designed and produced quickly.[7] The research into soft lithography led to the immediate growth in the potential applications of microfluidic devices as well. Due to the increased complexity of these systems, microfluidic valves were then needed to direct and control the flow of fluid.

Several of the commonly used valving methods to control flow for microfluidic systems are shown in Figure 20. These can be divided into divided into active and passive valves. Brief introductions for electrostatic valves, capillary bubble valves, PDMS-based valves, time-delayed valves, and piston-based valves are given below. Even today, the development of reliable microfluidic devices that can be used in everyday life, such as point-of-care devices, are hindered due to the lack of inexpensive and portable microfluidic valves.[15,16]

One method to direct flow is to change the surface energy of the microchannel to prevent fluid from entering a particular region, as shown in Figure 20a. This

straightforward procedure called fluid routing *via* surface chemistry will selectively direct fluid through a microchannel, but will not regulate flow as a valve. Using self-assembled monolayers or UV photolithography, researchers are able to pattern specific regions of the microchannel to be hydrophilic or hydrophobic. This surface modification results in polar solvents being confined to the hydrophilic regions and non-polar solvents to the hydrophobic regions. Therefore, fluid routing allows for fluid entering the microfluidic device to follow a specific pathway based on its surface tension.[17]

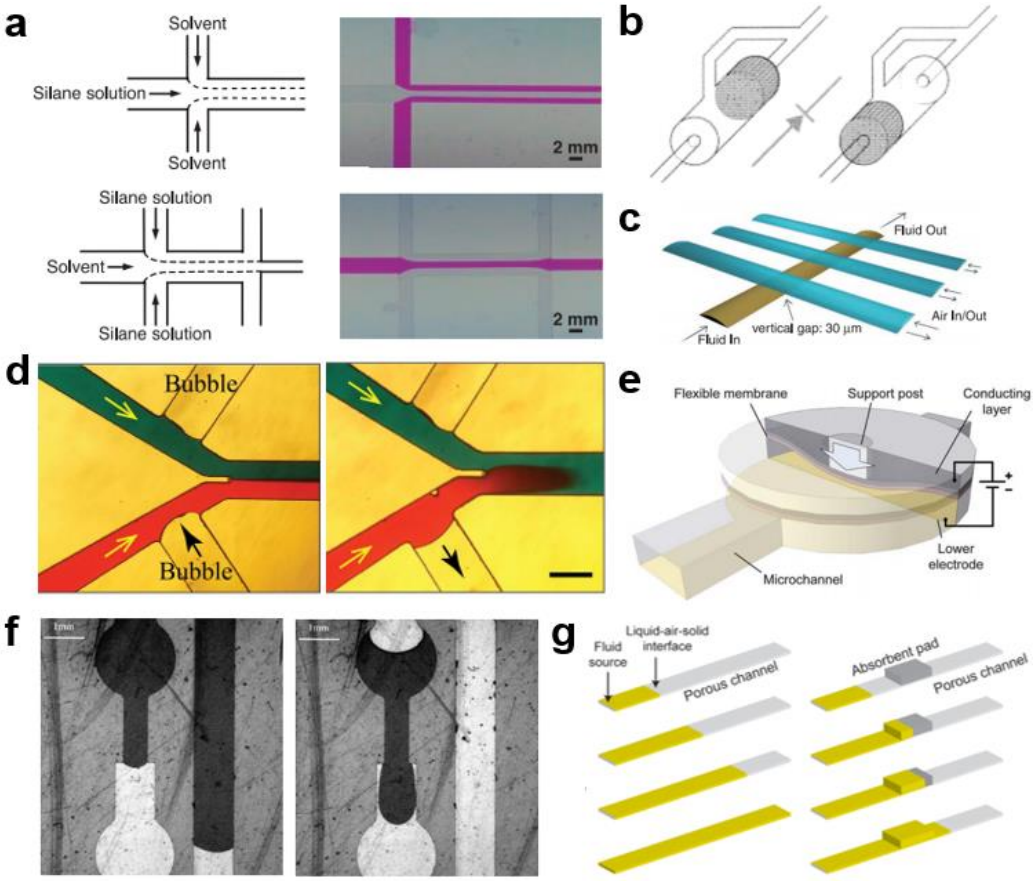

Figure 20. Microfluidic Valve Examples. (a) Fluid-routing *via* surface chemistry.[17] (b) Piston-based flow control valve.[18] (c) PDMS-based soft pneumatic valve.[19] (d) Bubble-based valve.[10] (e) Electrostatic valve.[20] (f) Capillary burst valves.[11] (g) Tunable-delay shunt.[12]

Microfluidic valves using piston-based methods are able to restrict flow in a single direction as shown in Figure 20b. These valves are effective systems that function

as passive check within the microfluidic device to prevent flow from flowing in the undesired direction. To fabricate, a UV-crosslinkable polymer is filled inside the valve channel and cured by laser polymerization to form a moveable piston inside the valve. The unreacted monomer solution is removed from the microchannel, while the piston is trapped due to a geometric restriction. While the fabrication process is not trivial, it does not require sacrificial layers or etching to produce the piston and can be completed in ambient conditions. The valve functions by allowing fluid to pass when flowing in the forward direction, but restricts flow due to the piston in the backwards direction without leakage.[18]

Microfluidic PDMS-based pneumatic valves rely on the elasticity of a siloxane-based membrane and an external air or vacuum pump to actuate the valve. As shown in Figure 20c, air pressure is increased or decreased to push out the PDMS layer into the channel to prevent flow or pull the PDMS layer up to allow for flow through the channel. The pneumatic valve is soft, flexible, and reliable, making it simple to integrate into a range of microfluidic applications. Fabrication of this valve requires a master mold with the inverted design of the microchannel that is produced by photolithography. PDMS is poured into the master mold, thermally cross-linked, and peeled off the mold to be assembled into the channel. A thin membrane of PDMS is placed over the channel piece, which can be controlled by air pressure to open and close the valve. In general, the pneumatic valve is one of the most common valves used for microfluidic devices, but requires complex assembly using multiple channels.[19]

By manipulating the pressure of air within a side channel connected to the main microchannel, the fluid flow in the channel can be tuned depending on the pressure of air

used. This air bubble method can also be regulated to induce mixing within a microchannel. For microvalves, the bubble of air is introduced into the flow of fluid, cutting off the flow within the channel. By controlling the expansion of air within the channel, the valve can induce a fully-closed, partially-closed, and fully-closed flow in the device as shown in Figure 20d. An advantage of this method is that it can be applied to a variety of fluids without using dissolvable barriers, which could affect the fluid further downstream. For air-sensitive solutions, inert argon or nitrogen gas can be used in place of air to act as the bubble within the microvalve.[10]

An electrostatic valve in a microfluidic device works by combining a moving conductive top electrode with an electric circuit to open and close the valve as shown in Figure 20e. In terms of scalability and integration, it is important that a microvalve be simple to fabrication and have a low actuate threshold. Unlike a pneumatic valve, an electrostatic valve has fewer moving parts and can be switched to open and close by applying a potential to the two electrodes. These types of microvalve systems have been produced for both hard microfluidics and soft microfluidics. While this advantage will allow for easy valve integration, a major drawback of this valve is the high voltages above ~100 V needed to actuate the valve to open or close.[20]

A capillary burst valve relies on an increase in channel dimension and shape to control the flow of fluid. The valve will actuate due to increased fluid pressure in the device and requires no moving parts. Fluid flows through a channel until it forms a meniscus due to geometrical restrictions and surface energy, which prevents its advancement. Following an increase in pressure, the fluid in the valve bursts forward, opening the valve irreversibly, as shown in Figure 20f. For some capillary burst valves,

the holding time is increased by changing the hydrophobicity at the entrance of the wider channel, further preventing the flow of fluid.[11]

There are several passive methods of microfluidic valves, which result in time-delayed fluid flow, such as the tunable-delay shunt. Several types of microfluidic valves require moving parts in order to control the flow, which are difficult to incorporate into paper-based microfluidic systems, and not well-suited for point-of-care microfluidic devices. For time-delayed valves, flow is reduced for a period of time through the channel, resulting in the delayed delivery of fluid within the microfluidic device, as shown in Figure 20f. For this, an absorbent pad is placed along the microchannel that significantly slows the fluid velocity compared to the control sample.[12] A key advantage is that these valves require no moving parts or external systems, making time-delayed valves very user-friendly.

In summary, the development of microvalves is an area of great interest and an important aspect hindering the integration of microfluidic components requiring complex fluid flow. The overall goal is the fabrication of reliable, user-friendly, portable, simple, and easily-fabricated valve that can be used in a variety of microfluidic applications, from drug testing to point-of-care biosensors, to complex biochemical analysis.

2.3 Electrowetting-on-a-Dielectric

Electrowetting valves function based on the phenomenon of electrowetting, which is described by a change in the surface energy of a material through applied voltage. The power to control surface energy by a potential difference is used a wide variety of applications from electrowetting pumps,[21] microconveyors,[22] dynamic lens,[23] to

electronic paper.[24] Electrowetting is examined by considering contact angle, which is used to quantify the wettability of a surface with respect to the liquid and vapor interfaces of a droplet above the surface. The contact angle can be measured using the static sessile drop method or advancing drop method on a goniometer. A surface with a contact angle greater than 90° is described as hydrophobic and with an angle less than 90° as hydrophilic. For an ideal surface, this relationship is described by Young's Equation, where the surface energy (γ) of solid (S), liquid (L), and gas (G) are related by the contact angle (θ). [25]

$$\gamma_{SG}\cos(\theta) = \gamma_{SG} - \gamma_{SL} \quad [1]$$

The Young-Lippmann relationship, given in Equation 2, accounts for the electric polarization by an applied voltage to an electrolyte solution on the surface energy of a metal. This relationship includes the applied voltage (V) and electric capacitance (C) of the material per unit area in contact with the droplet. The voltage is applied to both the electrolyte solution and the metal surface, creating an excess of negative charges in the metal. This excess results in charge polarization within the electrolyte and attracts positive charges to the interface between the liquid and solid, increasing the wetting behavior of the electrolyte solution on the surface.[25]

$$\gamma_{SG}\cos(\theta) = \gamma_{SG} - \gamma_{SL} + \frac{1}{2} C V^2 \quad [2]$$

A larger applied voltage will lead to a greater increase in wetting behavior. However, the interaction between the salts from the electrolyte solutions with the metal surface can cause irreversible electrochemical reactions that will corrode the metal. To avoid this, a thin dielectric material deposited between the metal and the solution to protect the metal, which is known as electrowetting-on-a-dielectric. The capacitance of a

material will increase as the thickness of the material decreases, therefore a thinner dielectric will require a lower applied voltage compared with a thicker material. A thin hydrophobic layer can be deposited over the dielectric to further increase the hydrophobic solid-liquid interaction prior to applied voltage. Depending on the final application, a single hydrophobic dielectric material can be used in place of two separate materials to simplify the system. This technique is shown in Figure 21.[25]

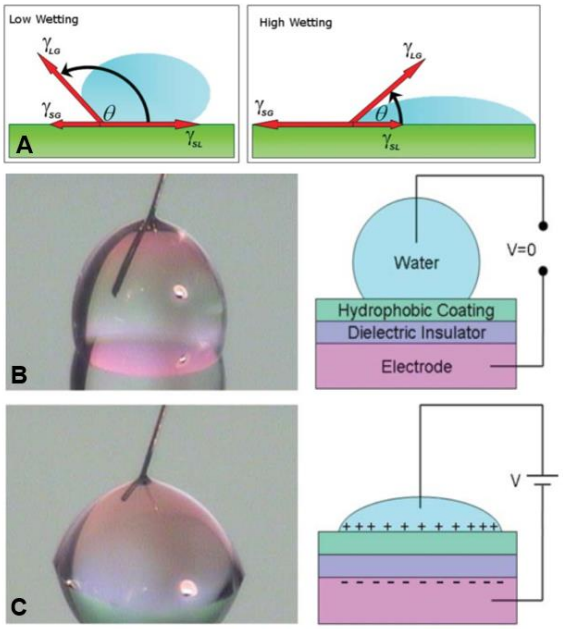

Figure 21. Schematic of Electrowetting-on-a-Dielectric.[25] (a) Visual depiction of the contact angle of a droplet on a hydrophobic surface with low wetting or a low surface energy (Left) and hydrophilic surface with high wetting or high surface energy (Right), (b) Hydrophobic contact angle of an electrolyte droplet on a metal electrode coated with thin hydrophobic and dielectric materials, (c) An applied voltage results in increased wetting of the metal surface.

In particular, applying electrowetting-on-a-dielectric to the field of microfluidics allows for a controllable, time-delivery valving system to deliver fluid within a channel. Electrowetting valves are a low-cost, single-use, printed flexible valve with for capillary flow microfluidic devices. By exploiting electrowetting, this valve will actuate-to-open within seconds following the application of a low voltage across two silver electrodes.[14]

The microchannel for this system is created by either pressure-sensitive adhesive (PSA) or by soft nanoimprint lithography, which is scalable by roll-to-roll manufacturing.[27] This inexpensive valve requires no external moving parts and extends the ability for capillary-flow microfluidics to include timed delivery of fluids for more complex reactions.

The general procedure to fabricate the valve, as shown in Figure 22, remains similar throughout the publications on electrowetting valves even for a variety of substrates. First, one electrode of silver nanoparticles is inkjet-printed on the substrate and thermally or photonically sintered until conductive. The inkjet-printed silver is a hydrophilic material, so it is modified with a thiolated self-assembled monolayer to become hydrophobic. The monolayer is solution-deposited by immersing the electrodes into a low concentration of the self-assembled monolayer in ethanol,[14] drop-casting the solution over the electrodes multiple times,[27] or inkjet-printing silver nanoparticles mixed with the monolayer.[26] Next, a second silver electrode is printed and annealed parallel to the first electrode. This electrode is referred to as the hydrophilic electrode.

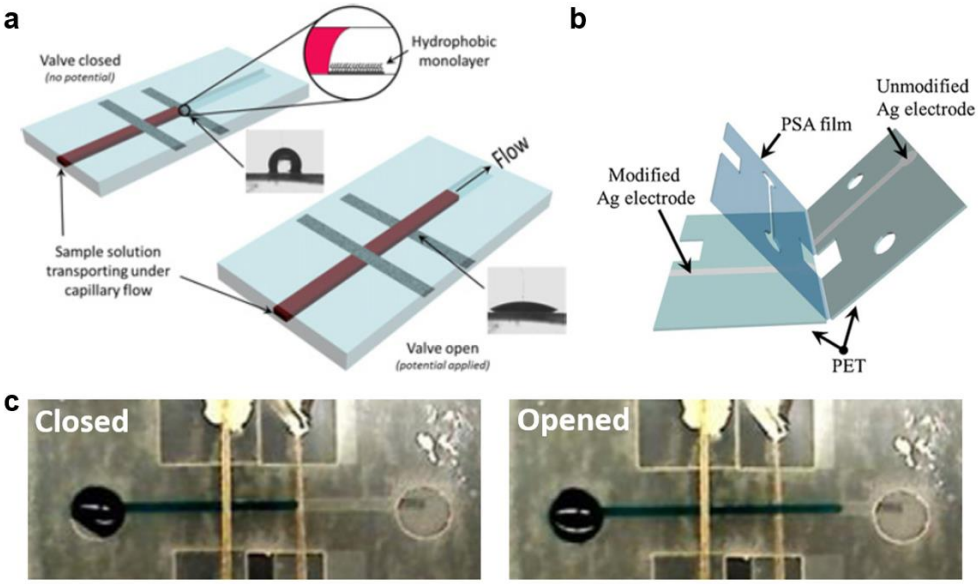

Figure 22. Electrowetting Valves.[14] (a) Schematic of electrowetting valve highlighting the chance in surface energy of the hydrophobic-modified silver electrode, (b)

Fabrication scheme to assemble electrowetting valve with electrodes on opposite sides of PET substrate, (c) Closed electrowetting valve (Left) and open electrowetting valve after applying voltage (Right).

Next, the two electrodes are assembled into a microfluidic channel. For this system, a channel is laser cut into a piece of PSA and placed perpendicular to the two electrodes. Inlet and outlet ports are laser cut from second piece of PET and placed over the microchannel. For proof-of-concept demonstrations, phosphate buffer solution (PBS) dyed with food coloring is used as the electrolyte solution for the electrowetting valve system. The fluid flows toward the electrodes by capillary force and passes the first hydrophilic electrode; however, it will be unable to pass the hydrophobic-modified electrode due to a mismatch of surface tension of the solution to surface energy of the substrate. The fluid can only flow past the second electrode by applying a negative voltage to hydrophobic electrode and an equal positive voltage to the hydrophilic electrode. This will provide additional charge to the electrolyte solution and cause electrowetting-on-a-dielectric between the solution and the surface.[28] This valve can be fabricated with two electrodes printed on the same side of a substrate,[27] or one electrode on the bottom substrate and the second electrode on the top substrate.[14] This flexibility in valve assembly allows the electrowetting valve to be tailored to the specific application needed for an integrated microfluidic system.

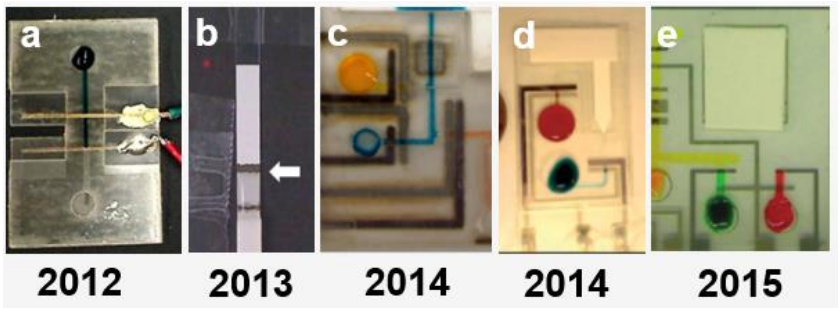

Figure 23. Images of electrowetting valves integrated with lateral flow assays for biological sensing applications over the years.

2.4. Wearable Microfluidic Valves

Wearable sweat sensing devices are emerging as a topic of interest for low-cost, point-of-care diagnostics.[29] Sweat is secreted from the eccrine glands and is composed of primarily water and a mixture of electrolytes, proteins, and biomolecules that contain valuable information regarding overall health status. Compared with blood, urine, and tears, sweat is a biofluid that offers the potential for noninvasive continuous monitoring of significant biomarkers over extended periods of time.[30] Recently, several innovative wearable sweat sensors using electrochemical and colorimetric analysis approaches have demonstrated the feasibility and importance of these types of devices.[31,32] A critical disadvantage of these systems is the lack of a microfluidic valving system designed for sweat collection at distinct time points. This capability would allow for quantitative assessment of electrolytes for dehydration monitoring or temporal variation of health biomarkers, such as glucose or cortisol levels.[33] Rogers, *et al*. (2017, 2018) recently addressed this concern by fabricating capillary burst valves for chrono-sampling of sweat[34] and water-actuated valves based on super absorbent polymers for discrete sampling of sweat.[35] These two valving methods are well-integrated and elegant; however, the designs require complex photolithography-based fabrication and the finished microfluidic devices fill to capacity in under an hour. Therefore, it is of interest to develop an inexpensive, adaptable, and user-friendly microfluidic valve for sweat collection over longer periods of time.

A low-cost, portable, and reliable microfluidic valve with demonstrated potential for point-of-care diagnostics is the electrowetting valve.[14] For sweat-based devices, the design of the valve would require some optimization, including (1) fabrication using

hydrophilic substrate and skin adhesive, (2) prevention of flow for several hours, and (3) the use a lower voltage for actuation. Currently, electrowetting valves have prevented fluid flow for less than an hour before premature failure[27] and required a voltage of at least 2 V for actuation,[28] indicating areas for further development.

2.5 Research Objectives

Here, we demonstrate the fabrication of wearable electrowetting valves with fast and reliable actuation at low voltages for sweat-based microfluidic devices. These flexible electrowetting valves are designed for rapid sweat collection by capillary-force driven flow using a hydrophilic substrate and a skin adhesive. By building on previous electrowetting valve research and optimizing several processing conditions, we have achieved exceptional valve hold times of more than six hours, electrode distances as small as 200 μm, and valve actuation at voltages as low as 1 V, preventing the electrolysis of water. Furthermore, multiple electrowetting valves are demonstrated to open individually from a single connected hydrophilic electrode, decreasing the dimensions of the overall valving system. As a proof-of-concept device, a wearable patch using electrowetting valves to collect artificial sweat into absorbent pads over specific time points is demonstrated. These results will allow for the integration of electrowetting valves into low-cost, scalable, point-of-care microfluidics that require precise control of sweat for continuous biomarker measurements.

This research was a result of Nano-Bio Manufacturing Consortium collaboration, led by General Electric to produce a sweat sensing device to characterize dehydration. This collaboration is a work of direct collaboration with Brenda Warren, Yiliang Zhou,

and Dr. Jeffrey Morse at UMass Amherst. Additionally, this research was possible due to guidance of Dr. Andrew Burns, Dr. Ralf Lenigk, and Dr. Azar Alizadeh at General Electric. Finally, this work on electrowetting valves began as a research project in Dr. Sarah Perry's course on Microfluidics under the guidance of Dr. Samuel Nugen and Dr. Charmaine Koo.

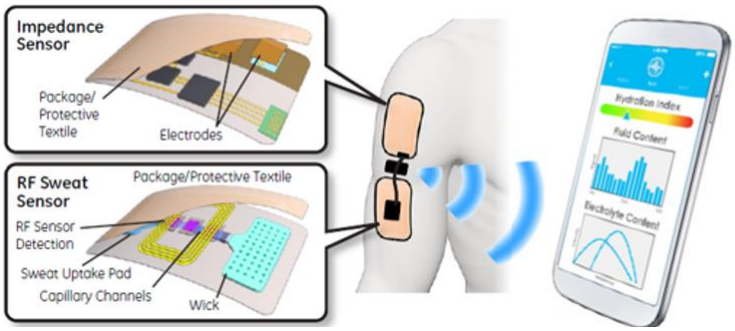

Figure 24. General Electric design for Nano-Bio Manufacturing Consortium-funded wearable impedance sensor and RF sweat sensor for personal health monitoring.

2.6 Material Selection

A commercial nanoparticle ink that would be viable for large-scale manufacturing and a hydrophilic PET substrate were selected to produce the wearable electrowetting valves. Four silver nanoparticle inks were considered for this study: Novacentrix JSA 102, Novacentrix JSB 25HV, Mitsubshi NBSIJ-FD02, and Clariant TPS 30. Test patterns for each silver ink were evaluated by comparing the formation of satellite drops, proper droplet jetting, ink pooling, surface tension, sintering temperature, and PFDT modification. Three types of PET substrates were assessed: ArFlow Film, McMaster-Carr PET, 3M Hydrophilic Film, and Novacentrix Novele PET. These substrates were tested for surface energy, wettability, silver ink adhesion, and PFDT modification. The difference is that the silver electrode must show an increase in hydrophobicity after PFDT modification, while the hydrophilic PET will remain unchanged. Based on this

study, the Novacentrix JSB-35HV silver ink was selected to be printed on the Novacentrix Novele PET substrate to produce the electrowetting valves. The inkjet-printing and final test patterns of this ink and substrate are shown in Figure 25.

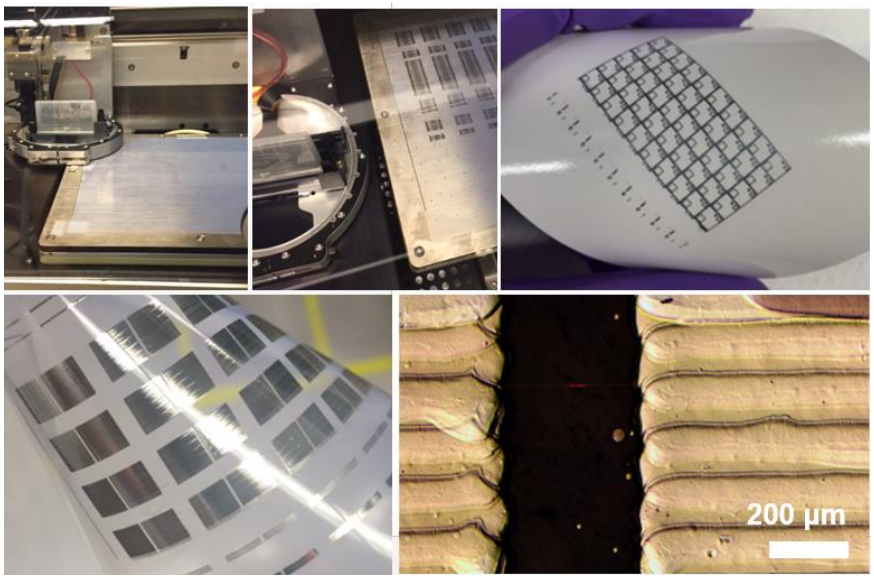

Figure 25. Inkjet-printed patterns using Novacentrix JSB2HV silver nanoparticle-based ink on PET and paper substrates.

For sweat-based sensing, it is important that the electrowetting valves and microfluidic system be effective when placed directly on human skin. Depending on the activity and hydration level of the individual or the ambient temperature or humidity, the sweat collected by the microfluidic device may have a high or low volumetric flow rate. Therefore, the hydrophilic substrate is an important consideration to allow the device to function at low flow rates. This substrate would allow for sweat to wick quickly through the microchannel in combination with capillary force towards the valve or sensor. The top layer of this microchannel will be a medical-grade adhesive for the microfluidic system to be conformal to the skin. To accommodate this design, both electrodes for the electrowetting valve are printed directly onto the hydrophilic PET substrate.

2.7 Experimental Section

Printed silver electrodes were fabricated from nanosilver ink (Metalon JSB-25HV, Novacentrix). This well-dispersed ink contained 25 wt% silver in an aqueous dispersion and was filtered through a 1 μm PTFE filter prior to printing. For printing, a Dimatix DMP-2850 (Fujifilm) inkjet printer was used with a 10 pL cartridge, a 28 V jetting voltage, and a customized waveform (see Figure S1). A single layer of silver ink was printed using 4 nozzles onto polyethylene terephthalate (PET, Novacentrix). The printed silver electrodes were annealed at 130°C in an oven for 5 min until conductive.

For the hydrophobic electrode fabrication, the annealed silver electrodes on PET were exposed to UV Ozone for 15 min to remove contaminants from the electrode surface. Next, the electrodes were immersed in a 12 mM solution of 1H, 1H, 2H, 2H-perfluorodecanethiol (PFDT, Sigma-Aldrich) in ethanol (Pharmco-Aaper) for 35 min under gentle agitation. Following the PFDT modification, the electrodes were rinsed with ethanol for 2 min and then dried with N_2. A second silver electrode, termed hydrophilic, was printed alongside the hydrophobic electrode and annealed.

A microfluidic setup was fabricated to test the electrowetting valves as shown in Figure 26. The 3 mm wide microchannel was laser cut from pressure-sensitive adhesive (PSA, ArCare 92712, 48 um thickness) with a liner on either side. A transparent, medical-grade, skin adhesive (3M Tegaderm) was used at the top layer to complete the valve, and hollow punches were used to create the inlet and outlet holes of 3 mm. The PSA microchannel was adhered to the back of the skin adhesive, and this assembly was then pressed over the electrowetting valve electrodes to minimize damage to the printed

electrodes. Artificial perspiration (Pickering, pH 4.5) mixed with blue food dye (McCormick) was pipetted over the inlet of the microfluidic device. To actuate-to-open, wires connected to a power supply box (80W Switching DC Power Supply, Extech) were clipped to the silver electrodes. The positive potential was applied to the hydrophilic electrode, and the negative potential to the hydrophobic electrode.

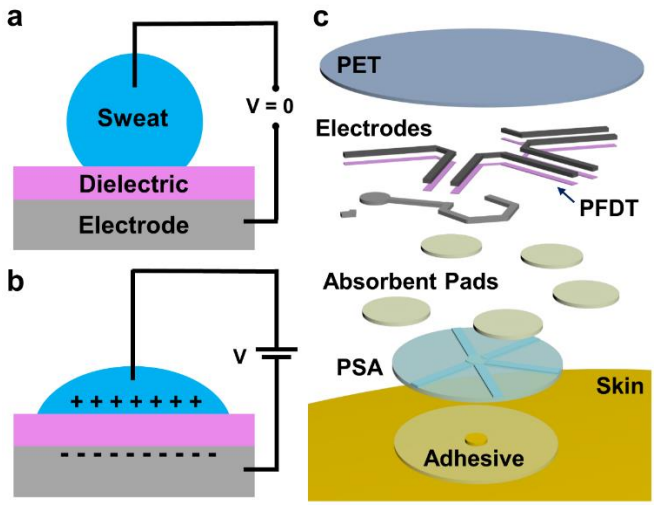

Figure 26. Schematic of electrowetting-on-a-dielectric and fabrication of wearable electrowetting valves. Electrowetting-on-a-dielectric is portrayed with a droplet of sweat over an insulator-covered conductive electrode (a) before and (b) after the application of voltage, allowing for a large change in wetting behavior. (c) Assembly of a wearable patch with integrated electrowetting valves.

Several characterization techniques were used to examine the printed electrowetting valves. Optical microscopy was used to observe the drop size spacing of the printed silver and distance between the electrowetting valve electrodes. Scanning electron microscopy (SEM, FEI Magellan 400 XHR) and energy dispersive x-ray spectroscopy (EDS, FEI Magellan 400 XHR) were used to characterize the surface of the printed silver electrodes. Mechanical profilometry was used to measure the height profile of the 20 μm drop size spacing printed silver electrode. The four-point resistivity system (Signatone) was used to measure the sheet resistivity of the printed electrode patterns at

different drop size spacing. The Video contact angle system (VCA Optima, AST Products, Inc) was used to measure the static contact angles of water on the printed and modified silver surfaces.

2.8 Inkjet-Printed Electrode Optimization

A robust hydrophobic electrode is the key to fabricate a reliable electrowetting valve that will remain closed for several hours. The printed silver electrode must demonstrate (1) high electrical conductivity, (2) strong adhesion to the PET substrate, (3) no cracks or delamination during the hydrophobic modification, and (4) high hydrophobicity following modification. The Novacentrix JSB25HV silver nanoparticle-based ink satisfied these criteria when printed on the Novacentrix Novele PET. To produce uniform droplets with clean tails during inkjet-printing, a voltage of 28 V was applied to the nozzles in a 10 pL cartridge with an optimized jetting waveform (see Figure 27). For high quality printed features with good adhesion, a single layer of ink was printed from four nozzles with cleaning cycles every 25 s.

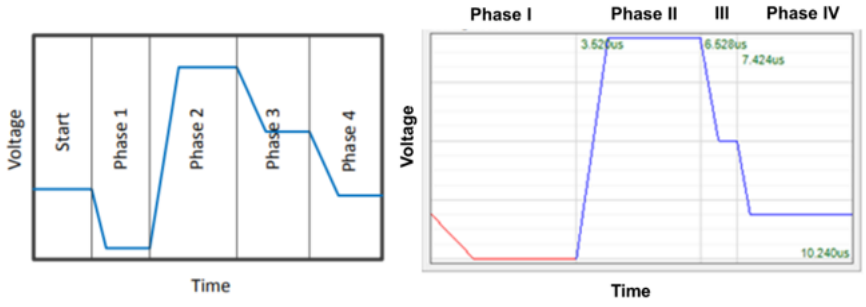

Figure 27. Customized jetting waveform for silver ink. Times shown: 3.52 µs, 6.528 µs, 7.424 µs, and 10.240 µs.

Five different drop size spacings (15 µm, 20 µm, 25 µm, 30 µm, 35 µm) were examined to understand the optimal inkjet-printing resolution required for the

electrowetting electrodes. Figure 28 shows optical microscopy images after thermal annealing and the sheet resistivity of silver ink printed at these drop size spacings on hydrophilic PET. Low resistivity is necessary for fast actuation of the electrowetting valves. Defects and gaps between print lines are visible for the 30 μm and 35 μm spacings in Figure 2d and 2e, which contribute to the high sheet resistivity measured for these samples in Figure 2f. Both 15 μm and 20 μm drop size spacing show low resistivity; however the 15 μm spacing resulted in ink pooling as shown in Figure 2a, leading to a large standard deviation of the measured sheet resistivity. Therefore, the electrowetting valve electrodes were printed at 20 μm drop size spacing, corresponding to 1270 dpi resolution. The conductivity for the 20 μm drop size spacing electrode was 8.80 x 10^2 ± 0.12 x 10^2 S/m, based on the electrode thickness (see Figure 29).

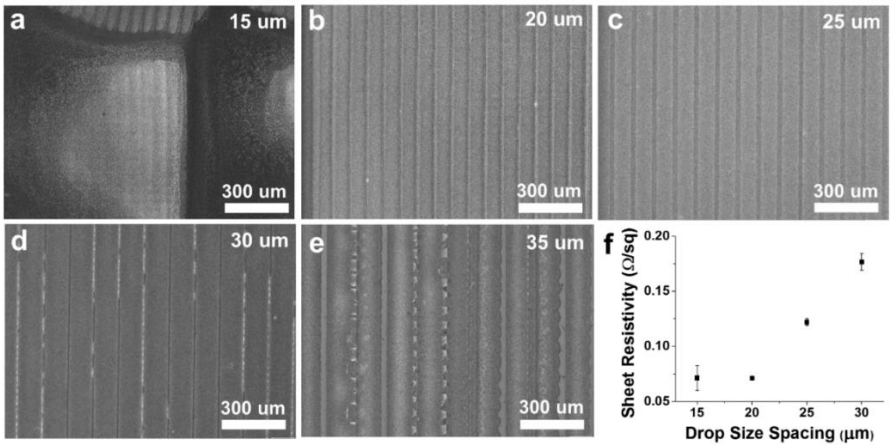

Figure 28. Drop Size Spacings. (a-e) Optical microscopy images of silver ink printed at 15 μm, 20 μm, 25 μm, 30 μm, 35 μm drop size spacings, respectively. (f) Sheet resistivity vs drop size spacing. As a note, silver printed at 35 μm drop size spacing demonstrated a high resistivity of 1.7 ± 0.4 Ω/sq.

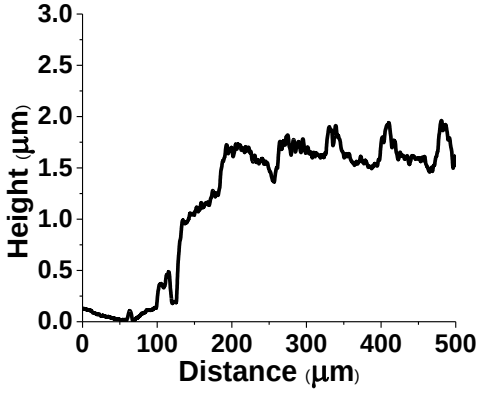

Figure 29. Height profile of silver electrode printed at 20 μm drop size spacing with thickness of 1.6 ± 0.1 um measured by mechanical profilometry.

2.9 Hydrophobic Electrode Modification

A self-assembled monolayer of PFDT was deposited on top of the printed electrode to modify the silver surface to become hydrophobic. Prior to PFDT modification, the electrode was cleaned by UV Ozone treatment to reduce contaminants on the surface, resulting in increased wetting on the silver surface as shown by comparing Figure 2a and 3b.[28] Several modification techniques were explored, including dropcasting directly onto the surface, vapor deposition, and an immersion method. The immersion method involved placing the printed electrodes into a solution PFDT in ethanol under gentle agitation and was followed by an ethanol rinse to remove excess PFDT. This method resulted in the highest hydrophobicity for the silver surface without damage to the electrodes. In comparison, electrodes printed at 25 μm, 30 μm, and 35 μm would crack or delaminate from the PET surface during the ethanol rinse step. A concentration of 12 mM PFDT was used for the immersion modification, compared to 2 mM PFDT used in previous electrowetting studies,[14,36] which significantly reduced the modification time from 3 hours to 35 min. This optimal immersion time was determined by measuring the static contact angle of water on the silver surface from 0 min to 40 min, as shown in

Figure 2g. Based on these results, the hydrophobicity of the silver electrodes did not increase further after 35 min (see Figure 30). The contact angle of the silver electrodes was measured both parallel and perpendicular to the direction of printing and found to be similar. As a note, a self-sintering silver ink (Mitsubishi NBSIJ-FD02), was also considered for faster electrode fabrication. However, the self-sintering silver ink was unable to obtain high hydrophobicity after PFDT modification. This is likely due to the increased number of additives in the ink required for self-sintering, decreasing the available reaction sites for PFDT on the electrode surface.

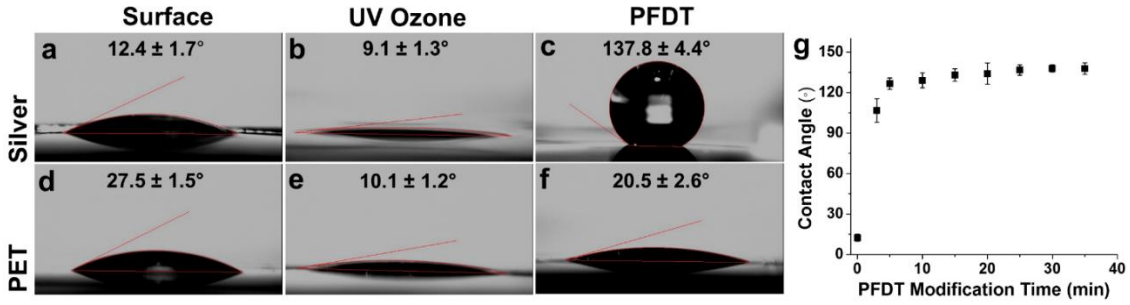

Figure 30. PFDT Modification. (a-c) Contact angle of silver surface, after UV Ozone treatment, and after PDFT immersion modification, respectively. (d-f) Contact angle of PET surface, after UV Ozone, and after PFDT immersion modification, respectively. (g) Contact angle of electrodes in 12 mM PFDT/ethanol solution over time.

For electrowetting valves to function well for wearable sweat devices, the hydrophilic PET layer needs to allow sweat to wick quickly by capillary action through the microchannel at high or low flow rates. This is an important consideration for sweat-based devices, since human sweating rates range from 0.1 μL/min to 5 μL/min.[37] Additionally, capillary-force driven flow provides for an inexpensive and simple microfluidic platform without external pumps. Therefore, it is important to demonstrate that the PET substrate remains hydrophilic following the PFDT immersion modification step. As shown in Figure 30e, d, and f, the contact angle of the original PET is slightly

higher than the PET after the UV Ozone and PFDT immersion steps, indicating the PET is still hydrophilic. This minor increase in surface energy is a temporary result of the UV Ozone treatment.

The surface of the printed silver electrodes was also characterized by scanning electron microscopy (SEM) and energy-dispersive x-ray spectroscopy (EDS). As shown in Figure 31a and b, the printed silver nanoparticles coalesce into larger grains forming a conductive silver film. The silver surface shows increased roughness at the microscale following the UV Ozone treatment to reduce contaminants, but remains unchanged after PFDT modification as seen in Figure 31c and d. EDS was also performed to ensure the PFDT monolayer was coated over the entire silver surface using the immersion method. Elemental analysis of the unmodified silver surface demonstrated predominantly silver (see Figure 32), while the PFDT-modified silver showed fluorine uniformly over the entire surface.

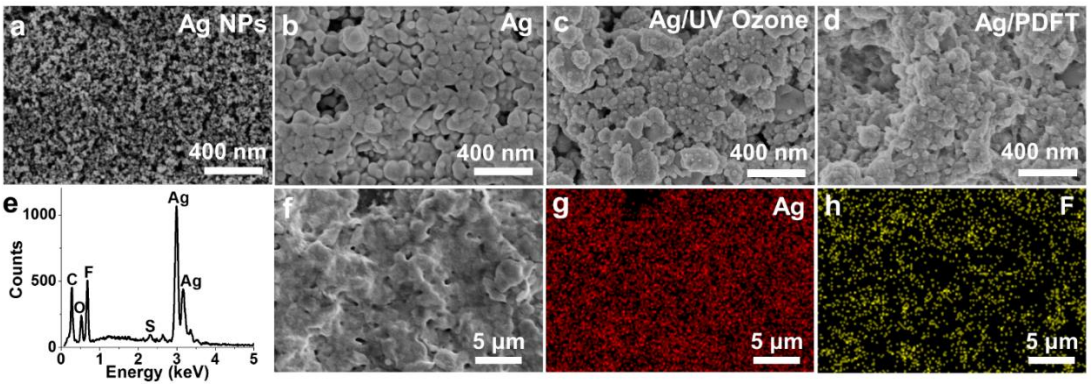

Figure 31. Electrode surface characterization. (a-d) High-resolution SEM images of printed silver nanoparticle-based ink, annealed silver, silver after UV ozone treatment, and silver after PFDT modification on PET substrate, respectively. Samples were coated with 2 nm Pt for imaging. (e) EDS spectrum showing elemental peaks of silver, fluorine, sulfur, carbon, and oxygen. (f) SEM image of silver after PFDT modification on Si substrate. (g) Elemental mapping of silver and (h) fluorine following PFDT modification

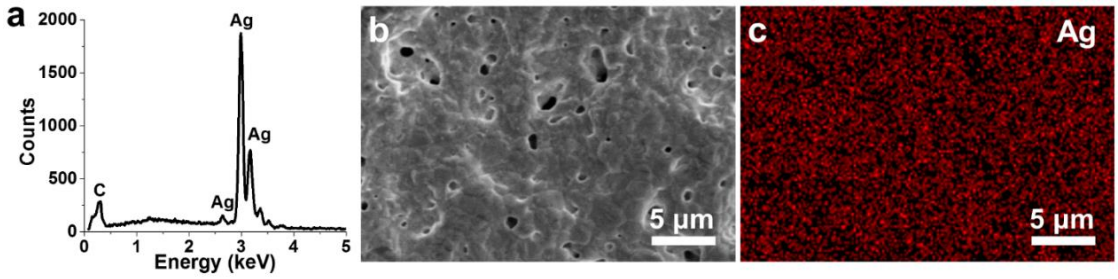

Figure 32. EDS spectrum of silver after thermal annealing on Si substrate. (a) EDS spectrum showing elemental peaks from silver and carbon. (b) SEM image of silver. (b) Elemental mapping of Ag.

2.10 Electrowetting Valve Assembly

The hydrophobic electrode was thus optimized for improved printing conditions, print quality, and PFDT modification time. These improvements were necessary to achieve superior valve hold time, referring to the time that the hydrophobic electrode will prevent fluid flow with no applied voltage. The valve hold times from previous literature range from 15 min to roughly 1 hour.[26,27] Our goal was for the valve to exceed a six hour window where the electrowetting valve would remain closed without untimely failure. For these experiments, the hydrophobic electrode was printed with a width of 500 µm. A laser cut PSA microchannel was attached to a skin adhesive with inlet and outlet holes and pressed onto the PET substrate with printed hydrophobic electrodes. Interestingly, the print direction of the hydrophobic electrode affected the valve hold time (see Figure 33). If the electrode is printed normal to the fluid flow direction, then it remains closed for more than nine hours; however, when the electrode is printed parallel to the flow, then it failed in less than three hours. This is a result of small microchannels formed during the inkjet-printing process where individual printed lines merge together. These printing artifacts are noticeable in the electrode height profile in Figure 29.

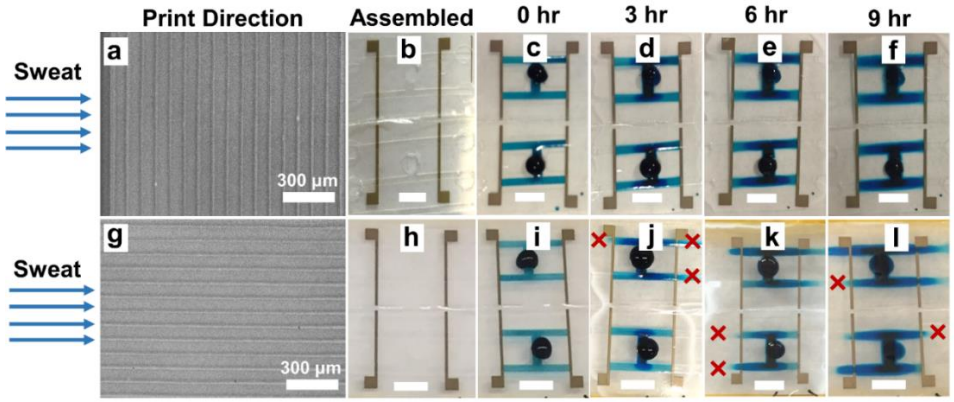

Figure 33. Valve hold time vs printing direction. (a) Electrodes printed perpendicular to the direction of fluid in the microchannel. (b) Assembled valves without hydrophilic electrode. (c-f) Hydrophobic electrode printed perpendicular to sweat flow prevents flow after 0 hr, 3 hr, 6 hr, and 9 hr, respectively. (g) Electrodes printed parallel to the direction of fluid in the microchannel. (h) Assembled valves without hydrophilic electrode. (i) Hydrophobic electrode printed parallel to sweat flow prevents flow at 0 hr, but (j-l) results in valve failure after 3 hr, 6 hr, and 9 hr, respectively. Scale bars for (b-f) & (h-l) are 10 mm.

To finish the electrowetting valve, the hydrophilic electrode was printed alongside the hydrophobic electrode, perpendicular to the direction of fluid flow and annealed until conductive at 130°C for five minutes. The PFDT monolayer is undamaged during the annealing step, and is thermally stable until 145°C.[38] This second hydrophilic electrode was aligned with the hydrophobic electrode using a fiducial mark and printed with a width of 1 mm at four increasing distances between the two electrodes: 200 µm, 500 µm, 1mm, and 2 mm (see Figure 34). Previous literature had not explored distances smaller than 1.36 mm between the electrodes.[26] Due to the similar surface energy of the PET before and after PFDT modification, the same inkjet-printing conditions were used to print the hydrophilic electrode, allowing for fast fabrication. Once the hydrophilic electrode was printed and annealed, a PSA microchannel and skin adhesive layer were assembled over the two electrodes on PET, completing the electrowetting valve.

Completed valves were also demonstrated to prevent the flow of artificial sweat for six hours and open successfully at low voltages as shown in Figure 35.

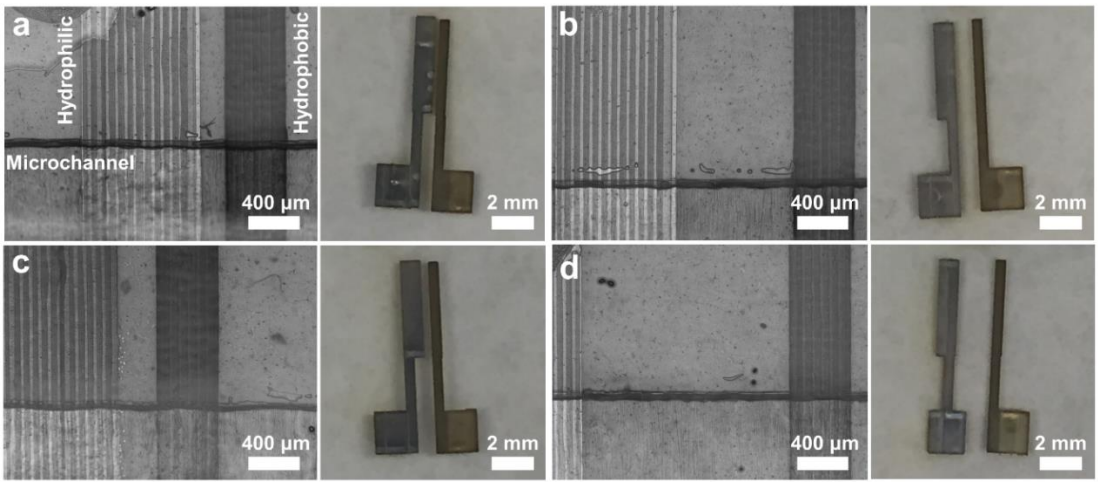

Figure 34. Electrode Distances. (a-d) (Left) Optical microscopy image of electrodes inside assembled valve and (Right) photos of printed individual electrowetting valves with electrode distances of 200 µm, 500 µm, 1 mm, and 2 mm, respectively.

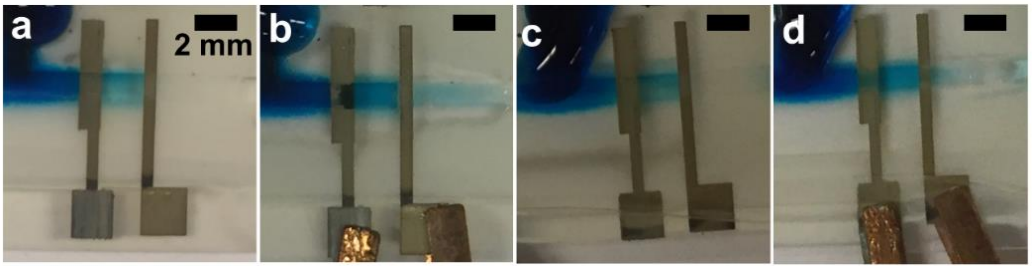

Figure 35. Valve actuation after six hours. (a, c) Electrowetting valve prevented flow for six hours prior to actuation using (b) 3 V and (d) 1 V.

2.11 Actuation and Wearable Valve System

To understand the actuation-to-open ability of the valves at the four electrode distances, four applied voltages were tested: 1 V, 2 V, 3 V, and 4 V, using an external power supply and artificial sweat dyed blue. It is important to apply the negative potential to the hydrophobic electrode and the positive voltage to the hydrophilic electrode. This will allow for reductive desorption to occur between the silver and the PFDT monolayer,

resulting in a faster opening time. Consequently, if these potentials are reversed, the positive voltage causes the monolayer to bind strongly to the silver, delaying the valve opening.[39] While it is known that larger voltages will result in faster actuation, it is important to demonstrate electrowetting valve feasibility at lower voltages to avoid the complications of electrolysis, as well as decrease overall power supply required. For example, the electrolysis of water occurs at 1.23 V and may damage biomarkers of interest within sweat.[40] Previous electrowetting valve literature relied on voltages as high as 16 V,[26] and has not examined voltages lower than 2 V.[14] The actuation-to-open time is also compared with the distance between the printed electrodes as shown in Figure 36. As expected, larger voltages result in faster valve actuation, while lower voltages require additional time to open. Similarly, the shorter the distance between the electrodes, the less time required for actuation. The effect of electrolysis, noticeably on the right side of the hydrophobic electrode in Figure 36b and c was most prominent at the 200 μm distance for high voltages. Valve actuation was also examined at 0.5 V; however, the opening times showed large variation and were not reproducible for all samples.

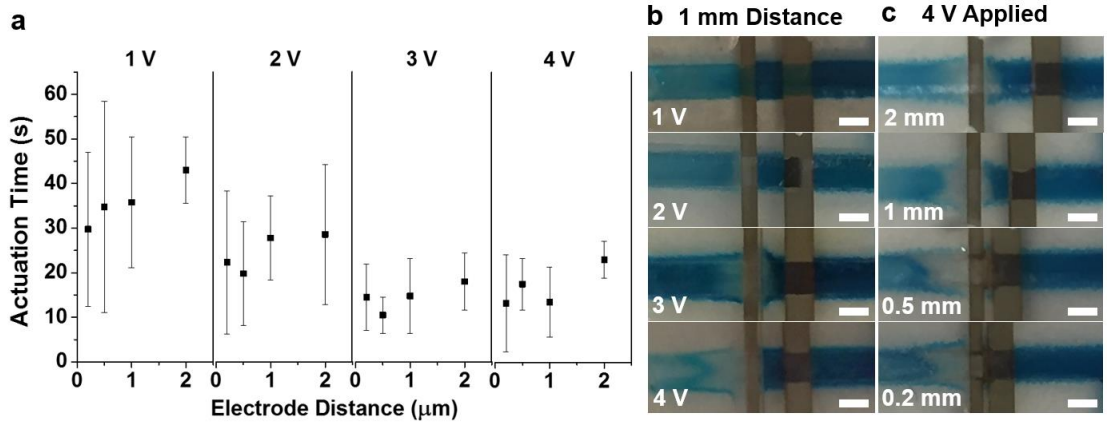

Figure 36. Electrode distance, actuation voltage, and electrolysis. (a) Electrowetting valves at four increasing distances tested for actuation time at five increasing voltages. Sample size of five valves. (b,c) Electrolysis more noticeable at smaller electrode

distances and higher voltages, where the hydrophobic electrode is on the right side. All scale bars are 2 mm.

For wearable microfluidics for continuous monitoring, it is important that the valving system use a minimal amount of space to allow for a smaller overall device footprint. Presently, each electrowetting valve involves a separate and individual hydrophilic and hydrophobic electrode. In comparison, by combining multiple hydrophilic electrodes together, it would be possible to achieve several electrowetting valves by using less space. It would not be possible to combine the hydrophobic electrodes in place of the hydrophilic electrodes, because reductive desorption of the PFDT from the silver surface may cause premature failure of valves. As shown in Figure 37, multiple electrowetting valves were successfully combined on a single hydrophilic electrode. Here, a voltage of 4 V was applied for electrodes separated by a distance of 500 μm. Furthermore, the actuation time could be also be modified by changing the distance between the electrodes of multiple valves on a single hydrophilic and hydrophobic electrodes, if a slight time delay was required prior to opening particular valves. Additionally, the consolidation of valves in this way would decrease fabrication time, increase space for electrical and sensing elements, and reduce the final device size.

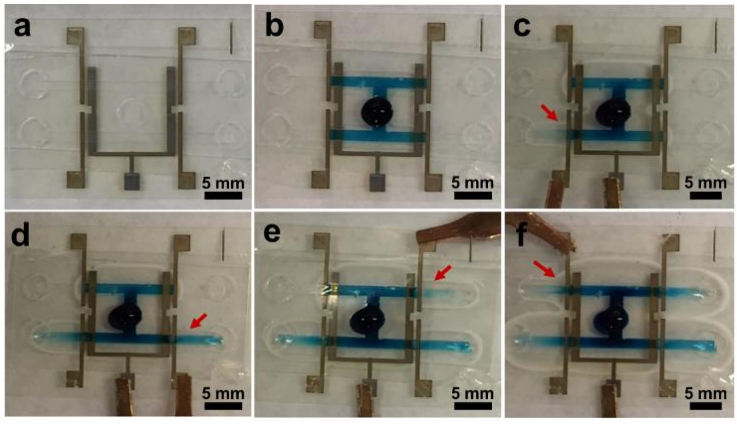

Figure 37. Single Hydrophilic Electrode for Multiple Valves. (a) Four electrowetting valves assembled on a single hydrophilic electrode with 500 μm distance between

electrodes. (b) Simulated sweat added to the inlet centered between the valves. (c-f) Valves are opened using 4 V with a ten min wait time in a counterclockwise order.

Finally, a proof-of-concept wearable device with integrated electrowetting valves was constructed, as shown in Figure 38. Here, four electrowetting valves are designed around a central inlet, which lead to adsorbent pads at the perimeter of the device. A single hydrophilic electrode wraps around the center inlet and is used for all four valves. The silver connectors to the electrodes are arranged for easy incorporation of a watch battery (1.5 V) with the hydrophilic electrode and small pushbutton or electrical switches between the hydrophobic electrodes to actuate the individual valves as shown in Figure 39. In Figure 38h-k, a voltage of 3V was applied to each valve resulting in fast actuation of artificial sweat into the microchannels leading to the absorbent pads. This wearable device is deployed on a human arm in Figure 38b, demonstrating the capability of integrated electrowetting valves for long-term sweat monitoring.

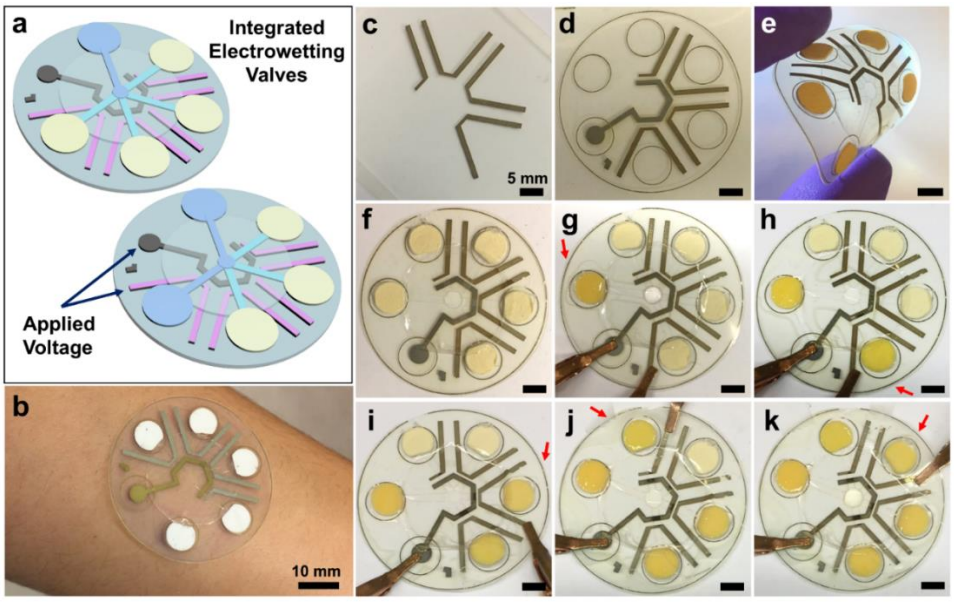

Figure 38. Integrated electrowetting valve wearable device with absorbent pads. (a) Schematic of electrowetting valve device before and after actuation of the first valve. (b) Optical image of wearable electrowetting valve device placed on human arm. (c) Printed hydrophobic electrodes after PFDT modification and (d) after printed hydrophilic electrodes. (e) Mechanical bendability of device. (f) Assembled integrated electrowetting

valve device. (g) Artificial sweat is pipetted into the inlet and absorbed by the initial pad. (h-k) Valves are actuated sequentially using 3V with a ten minute wait time, as shown by the darker yellow color of the absorbent pads after contact with sweat. Scale bars for (c-k) are 5 mm.

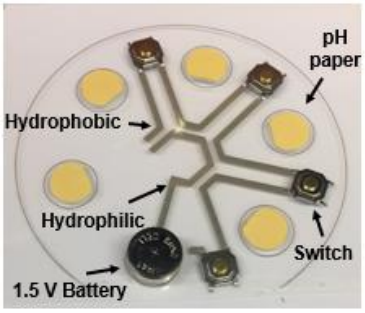

Figure 39. Integrated electrowetting valves shown with a watch battery and mini pushbutton switches for valve actuation.

2.12 Conclusions

We have demonstrated the feasibility of wearable electrowetting valves for integration with sweat sensing devices for collection of sweat at well-defined time points. Electrowetting valves were fabricated on hydrophilic PET for fast capillary-driven flow and a medical-grade adhesive for conformal contact with skin. Inkjet printing and hydrophobic modification conditions were further optimized for improved electrowetting valve performance. The valve hold time was extended to over 6 hours, the electrode distances decreased to 200 μm, and voltages as low as 1 V were used to reliably actuate-to-open the microfluidic valve. Furthermore, multiple electrowetting valves were integrated together on a single hydrophilic electrode to reduce the size dimensions of these valves on a wearable platform. A wearable integrated electrowetting valve device with absorbent pads was fabricated with four valves in a circular design, which were actuated individually. In this way, these user-friendly electrowetting valves allow for the collection of sweat at precise time intervals over several hours, leading to improved monitoring for health status through sweat devices.

2.13 References

(1) Koh, A.; Kang, D.; Xue, Y.; Lee, S.; Pielak, R. M.; Kim, J.; Hwang, T.; Min, S.; Rogers, J. A. A Soft, Wearable Microfluidic Device for the Capture, Storage, and Colorimetric Sensing of Sweat. *Sci. Transl. Med.* **2016**, *8* (366).

(2) Elvira, K. S.; i Solvas, X. C.; Wootton, R. C. R.; deMello, A. J. The Past, Present and Potential for Microfluidic Reactor Technology in Chemical Synthesis. *Nat. Chem.* **2013**, *5* (11), 905–915.

(3) Guha, S.; Perry, S. L.; Pawate, A. S.; Kenis, P. J. A. Fabrication of X-Ray Compatible Microfluidic Platforms for Protein Crystallization. *Sensors Actuators, B Chem.* **2012**, *174*, 1–9.

(4) Leyrat, A. A.; Pirone, D. M.; Chen, C. S.; Quake, S. R. Versatile , Fully Automated , Microfluidic Cell. *Anal. Chem.* **2007**, *79* (22), 8557–8563.

(5) Stone, H. A.; Stroock, A. D.; Ajdari, A. Engineering Flows in Small Devices. *Annu. Rev. Fluid Mech.* **2004**, *36* (1), 381–411.

(6) Byrnes, S.; Thiessen, G.; Fu, E. Progress in the Development of Paper-Based Diagnostics for Low-Resource Point-of-Care Settings. *Bioanalysis* **2013**, *5* (22), 2821–2836.

(7) Oh, K. W.; Ahn, C. H. A Review of Microvalves. *J. Micromechanics Microengineering* **2006**, *16* (5), R13–R39.

(8) Zhang, C.; Xing, D.; Li, Y. Micropumps, Microvalves, and Micromixers within PCR Microfluidic Chips: Advances and Trends. *Biotechnol. Adv.* **2007**, *25* (5), 483–514.

(9) Tice, J. D.; Desai, a V; Bassett, T. a; Apblett, C. a; Kenis, P. J. a. Electrostatic Microvalves for Integrated Microchemical Systems. *uTAS* **2011**, 1813–1815.

(10) Khoshmanesh, K.; Almansouri, A.; Albloushi, H.; Yi, P.; Soffe, R.; Kalantar-zadeh, K. A Multi-Functional Bubble-Based Microfluidic System. *Sci. Rep.* **2015**, *5*, 9942.

(11) Cho, H.; Kim, H. Y.; Kang, J. Y.; Kim, T. S. How the Capillary Burst Microvalve Works. *J. Colloid Interface Sci.* **2007**, *306* (2), 379–385.

(12) Toley, B. J.; McKenzie, B.; Liang, T.; Buser, J. R.; Yager, P.; Fu, E. Tunable-Delay Shunts for Paper Micro Fl Uidic Devices. *Anal. Chem.* **2013**, *85* (23), 11545–11552.

(13) Thorsen, T.; Maerkl, S. J.; Quake, S. R. Microfluidic Large-Scale Integration. *Science.* **2002**, *298* (5593), 580–584.

(14) Merian, T.; He, F.; Yan, H.; Chu, D.; Talbert, J. N.; Goddard, J. M.; Nugen, S. R. Development and Surface Characterization of an Electrowetting Valve for Capillary-Driven Microfluidics. *Colloids Surfaces A Physicochem. Eng. Asp.* **2012**, *414*, 251–258.

(15) Erickson, D.; Li, D. Integrated Microfluidic Devices. *Anal. Chim. Acta* **2004**, *507* (1), 11–26.

(16) Whitesides, G. M. The Origins and the Future of Microfluidics. *Nature* **2006**, *442* (7101), 368–373.

(17) Zhao, B.; Moore, J. S.; Beebe, D. J. Surface-Directed Liquid Flow inside Microchannels. *Science* **2001**, *291* (5506), 1023–1026.

(18) Hasselbrink, E. F.; Shepodd, T. J.; Rehm, J. E. High-Pressure Microfluidic Control in Lab-on-a-Chip Devices Using Mobile Polymer Monoliths. *Anal. Chem.* **2002**, *74* (19), 4913–4918.

(19) Unger, M. A. Monolithic Microfabricated Valves and Pumps by Multilayer Soft Lithography. *Science (80-.).* **2000**, *288* (5463), 113–116.

(20) Desai, A. V.; Tice, J. D.; Apblett, C. a.; Kenis, P. J. a. Design Considerations for Electrostatic Microvalves with Applications in Poly(dimethylsiloxane)-Based Microfluidics. *Lab Chip* **2012**, *12* (6), 1078.

(21) MacH, P.; Krupenkin, T.; Yang, S.; Rogers, J. A. Dynamic Tuning of Optical Waveguides with Electrowetting Pumps and Recirculating Fluid Channels. *Appl. Phys. Lett.* **2002**, *81* (2), 202–204.

(22) Moon, I.; Kim, J. Using EWOD (Electrowetting-on-Dielectric) Actuation in a Micro Conveyor System. *Sensors Actuators, A Phys.* **2006**, *130–131* (SPEC. ISS.), 537–544.

(23) Hendriks, B. H. W.; Kuiper, S.; Van As, M. A. J.; Renders, C. A.; Tukker, T. W. Electrowetting-Based Variable-Focus Lens for Miniature Systems. *Opt. Rev.* **2005**, *12* (3), 255–259.

(24) Di, Q. T.; Zhang, H.; Liang, X. L.; Li, A. D.; Xiao, C. S.; Wu, D.; Xu, Q. Y. Electrowetting Display Pixels Fabricated by Nanoimprint Lithography. **2015**, No. Asei, 495–501.

(25) Shamai, R.; Andelman, D.; Berge, B.; Hayes, R. Water, Electricity, and Between… On Electrowetting and Its Applications. *Soft Matter* **2008**, *4* (1), 38–45.

(26) Koo, C. K. W.; He, F.; Nugen, S. R. An Inkjet-Printed Electrowetting Valve for Paper-Fluidic Sensors. *Analyst* **2013**, *138* (17), 4998–5004.

(27) Chen, J.; Zhou, Y.; Wang, D.; He, F.; Rotello, V. M.; Carter, K. R.; Watkins, J. J.; Nugen, S. R. UV-Nanoimprint Lithography as a Tool to Develop Flexible Microfluidic Devices for Electrochemical Detection. *Lab Chip* **2015**, *15*, 3086–3094.

(28) He, F.; Grimes, J.; Alcaine, S. D.; Nugen, S. R. A Hybrid Paper and Microfluidic Chip with Electrowetting Valves and Colorimetric Detection. *Analyst* **2014**, *139* (12), 3002–3008.

(29) Jadoon, S.; Karim, S.; Akram, M. R.; Kalsoom Khan, A.; Zia, M. A.; Siddiqi, A. R.; Murtaza, G.; Jadoon, S.; Karim, S.; Akram, M. R.; Kalsoom Khan, A.; Zia, M. A.; Siddiqi, A. R.; Murtaza, G. Recent Developments in Sweat Analysis and Its Applications. *Int. J. Anal. Chem.* **2015**, *2015*, 1–7.

(30) Bandodkar, A. J.; Wang, J. Non-Invasive Wearable Electrochemical Sensors: A Review. *Trends Biotechnol.* **2014**, *32* (7), 363–371.

(31) Koh, A.; Kang, D.; Xue, Y.; Lee, S.; Pielak, R. M.; Kim, J.; Hwang, T.; Min, S.; Banks, A.; Manco, M. C.; Wang, L.; Ammann, K. R.; Jang, K.; Han, S.; Ghaffari, R.; Paik, U.; Slepian, M. J.; Huang, Y.; Rogers, J. A. A Soft, Wearable Microfluidic Device for the Capture, Storage, and Colorimetric Sensing of Sweat. *Sci Transl Med* **2017**, *8* (366), 1–14.

(32) Gao, W.; Emaminejad, S.; Nyein, H. Y. Y.; Challa, S.; Chen, K.; Peck, A.; Fahad, H. M.; Ota, H.; Shiraki, H.; Kiriya, D.; Lien, D.-H.; Brooks, G. A.; Davis, R. W.; Javey, A. Fully Integrated Wearable Sensor Arrays for Multiplexed in Situ Perspiration Analysis. *Nature* **2016**, *529* (7587), 509–514.

(33) Munje, R. D.; Muthukumar, S.; Panneer Selvam, A.; Prasad, S. Flexible Nanoporous Tunable Electrical Double Layer Biosensors for Sweat Diagnostics. *Sci. Rep.* **2015**, *5*, 14586.

(34) Choi, J.; Kang, D.; Han, S.; Kim, S. B.; Rogers, J. A. Thin, Soft, Skin-Mounted Microfluidic Networks with Capillary Bursting Valves for Chrono-Sampling of Sweat. *Adv. Healthc. Mater.* **2017**, *6* (5), 1–10.

(35) Kim, S. B.; Zhang, Y.; Won, S. M.; Bandodkar, A. J.; Sekine, Y.; Xue, Y.; Koo, J.; Harshman, S. W.; Martin, J. A.; Park, J. M.; Ray, T. R.; Crawford, K. E.; Lee, K. T.; Choi, J.; Pitsch, R. L.; Grigsby, C. C.; Strang, A. J.; Chen, Y. Y.; Xu, S.; Kim, J.; Koh, A.; Ha, J. S.; Huang, Y.; Kim, S. W.; Rogers, J. A. Super-Absorbent Polymer Valves and Colorimetric Chemistries for Time-Sequenced Discrete Sampling and Chloride Analysis of Sweat via Skin-Mounted Soft Microfluidics. *Small* **2018**, *14* (12), 1–11.

(36) He, F.; Nugen, S. R. Automating Fluid Delivery in a Capillary Microfluidic Device Using Low-Voltage Electrowetting Valves. *Microfluid. Nanofluidics* **2014**, *16* (5), 879–886.

(37) Brueck, A.; Iftekhar, T.; Stannard, A.; Yelamarthi, K.; Kaya, T. A Real-Time Wireless Sweat Rate Measurement System for Physical Activity Monitoring. *Sensors* **2018**, *18* (2), 533.

(38) Chandekar, A.; Sengupta, S. K.; Whitten, J. E. Thermal Stability of Thiol and Silane Monolayers : A Comparative Study. *Appl. Surf. Sci.* **2010**, *256*, 2742–2749.

(39) Love, J. C.; Estroff, L. A.; Kriebel, J. K.; Nuzzo, R. G.; Whitesides, G. M. *Self-Assembled Monolayers of Thiolates on Metals as a Form of Nanotechnology*; 2005; Vol. 105.

(40) Rossmeisl, J.; Logadottir, A.; Nørskov, J. K. Electrolysis of Water on Oxidized Metal Surfaces. *Chem. Phys.* **2005**, *319*, 178–184.

CHAPTER 3

MICROFLUIDIC GLUCOSE SWEAT SENSORS

Non-invasive wearable sweat biosensors offer compelling opportunities for portable, disposable, and inexpensive point-of-care diagnostics. We demonstrate a skin-compatible "smart Band-Aid" microfluidic design for continuous glucose monitoring. The low-cost laser cut microfluidic device is composed of an adhesive-based microchannel to enable capillary-driven sweat flow and prevent sensor contamination from residual sweat. Solution-based electrochemical sensors are fabricated by inkjet-printed graphene and silver inks, electrodeposited mediator layers, and drop-casted biorecognition elements. To examine the effect of perspiration rate on sensor performance for continuous monitoring applications, a synthetic skin is developed with 50 μm pores at a distribution of 250 pores/cm^2, mimicking human skin. An enzymatic amperometric glucose sensor with a two-electrode system was integrated with the synthetic skin to explore low flow rate (1-5 μL/min) sensing. The glucose sensor attained a range of 0.2 mM to 1 mM and exhibited reproducible response curves at 2 μL/min and higher. The glucose concentration and sweating rates used for this study are within physiological relevant ranges. In summary, the proposed microfluidic sensor platform indicates the potential for a low-cost flexible multi-sensing device, enabling real-time assessment of key biomarkers for improved human health.

3.1 Introduction

Sweat contains valuable information regarding biomarkers important for human health and well-being. Recently, several wearable sweat sensors demonstrate the delivery of sweat to colorimetric or electrochemical biosensors to detect glucose, pH, temperature, urea, lactate, and others. This previous research illustrates the feasibility of these devices to allow for direct, noninvasive, and continuous performance monitoring, which can also enable early disease diagnosis. The goal is for these devices to be disposable, low cost, and of use for point-of-care diagnostics. In particular, inexpensive wearable devices integrated with functional nanomaterials for sensing applications would allow for sweat collection and diagnostics.[1]

Although there has been significant progress for sweat sensing devices, there are still considerable challenges that have yet to be addressed for sweat-based wearable devices, including (1) sweating flow rates that vary, (2) contamination between the skin and sensor electrodes, (3) unknown sample volume over sensor surface, and (4) time-stamping of old versus newly produced sweat.[2] Presently, many of these innovative sweat-based devices rely on direct contact between the sensor electrodes and human skin, which may introduce contamination between biomarkers found on the skin versus those generated within sweat. The integration of wearable sweat-devices that use microfluidic channels would increase the potential of these devices and improve upon the above challenges. Despite tremendous advances in sweat sensing devices, the combination of solution-processable sensing materials, microfluidics, and wearable sweat devices to develop a single low-cost system remains a great challenge.

In particular, a key biomarkers of interest is glucose, which is found within sweat and correlated with the levels of these biomarkers with blood. Glucose is molecule that provide energy to cells within the body. However, many patients suffer from diabetes, where the blood has an inability to control the amount of glucose within the blood and suppresses the formation of insulin. Therefore, if a noninvasive method can be developed for glucose measurement, then it would be a great interest to patients, hospitals, and low-resources areas.

3.2 Sweat Biosensor Devices

Wearable sweat-based devices for personal health monitoring have received tremendous attention due to potential healthcare, athletic, and military applications. [3–5] Sweat offers the potential for accurate, continuous, and real-time assessment of key biomarkers without invasive measurements or the possibility of introducing infection, as compared with blood sampling. Wearable sweat sensors can be placed externally and painlessly on the skin without additional action from the user, unlike devices used to probe other noninvasive biofluids, including tears, saliva, interstitial fluid, or urine. Wireless wearable sweat devices can be paired with smartphone apps for ease of monitoring, allowing the user to modify lifestyle or behavior to achieve an improved health state.[6] This real-time assessment is particularly important for diabetes management, pathogen detection, athletic training, drug measurement, and stress monitoring. Sweat production can also be induced by iontophoresis when necessary, such as during irregular sampling or a sedentary state when no sweat is produced.

While sweat is principally composed of water (99%), it also contains electrolytes, metabolites, amino acids, small molecules, and proteins, secreted from eccrine sweat glands. The concentrations of biomarkers in sweat are diluted, requiring high performance sensors that operate under low sample volume and dynamic flow rates. Electrochemical sensors are predominately used for wearable sweat devices due to precise measurements, ease of miniaturization, and inexpensive fabrication. Recent studies have demonstrated incredible scientific advancements through the development and assessment of electrochemical sweat sensors, including a multi-sensing wearable arrays,[3] temperature monitoring,[7] stretchable and textile pH detection,[8,9] electrolyte monitoring,[10,11] and low-volume sweat collection.[12] Two key biomarkers accessible through sweat are cortisol[13–15] and glucose, [16–18] for which sweat-sensing devices are being developed as well. Elevated levels of cortisol within the body are linked with increased physiological stress and fatigue, and high glucose levels due to diabetes mellitus must be constantly monitored by patients. An additional challenge for wearable sweat biosensors is the mixing of old sweat with new sweat at the skin interface and contamination from cellular and microbial byproducts on the skin as well.[19] Sensor systems integrated with microfluidic wearables would allow for constant renewal of sweat at the sensor electrodes without contamination from previous sweat. This concept is evaluated by only a handful of studies, indicating the critical need for further research implementing inexpensive assembly.[19,4,20,2] Recent progress in wearable sweat devices require complex and expensive fabrication, such as the traditional photolithography within a clean room environment to produce polydimethylsiloxane-based microfluidics, and vacuum-evaporation of precious metals for electrode fabrication. For truly low-cost

microfluidic designs, alternative approaches, such as adhesive-based microfluidics or paperfluidics and direct printing and patterning of electrodes to enable cheap point-of-care devices for health monitoring.[21,22,1]

3.3 Glucose Monitoring Systems

Increased and prolonged levels of glucose within the blood can result in diabetes mellitus, commonly known as diabetes. This disease can develop in three forms: Type 1, previously known as juvenile diabetes where the body is unable to produce enough insulin; Type II, where the body developed insulin resistance and is unable to properly process insulin; or gestational diabetes, which can affect women during pregnancy, but usually resolves after childbirth. Of these types, Type II accounts for 90% of all diabetes cases and largely results from improper diet and lack of exercise. The goal of diabetes treatment is to reduce long-term complications of the disease by increasing or decreasing glucose levels to achieve normal concentrations.[17]

For those patients who require insulin injections to control diabetes, proper care must be taken to regulate and measure blood glucose levels. Patients with Type I diabetes are recommended to measure blood glucose levels at least four times per day, which is particularly difficult for younger patients. Similarly, patients who suffer from hypoglycemia, or constant low blood glucose, must also have accurate readings of blood glucose for proper medication and treatment. This measurement requires daily testing of blood glucose levels through a finger prick to draw blood, which is placed on a paper glucose strip and analyzed by a handheld glucometer device.[17]

These glucometers utilized electrochemical sensors to determine the levels of glucose within blood. The user will place a small drop of blood onto a paper strip, which draws the blood into the glucometer and reacts with glucose oxidase or dehydrogenase and undergoes a series of redox reactions, generating an electric current. This current is quantified and analyzed against a calibration curve to determine the level of glucose required to cause such as reaction. The glucose concentration within blood is 2 x 10^{-3} M to 40 x 10^{-3} M, while in sweat is much lower at 0.01 x 10^{-3} M to 1.11 x 10^{-3} M. Current well-established, invasive methods for measuring blood glucose levels are shown in Figure 40 on the left, while noninvasive methods demonstrated in literature for tears, sweat, interstitial fluid, and saliva are shown on the right.[17]

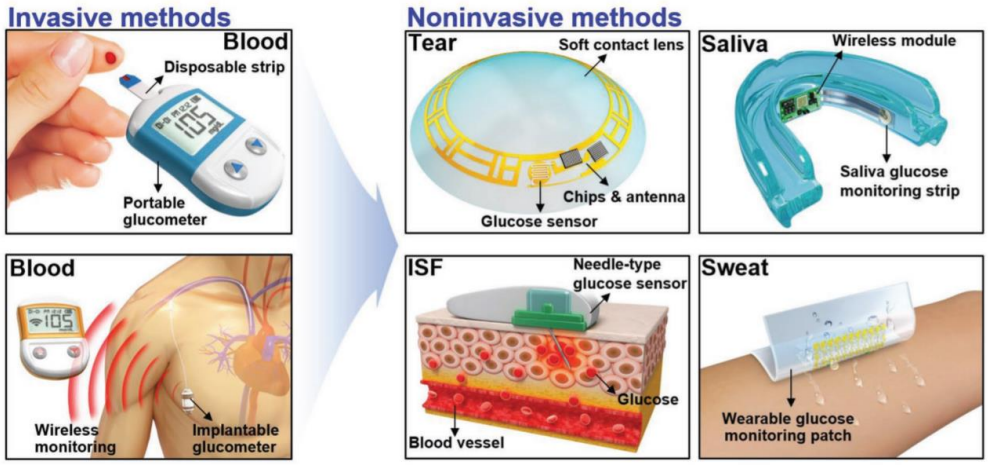

Figure 40. Current state of glucose monitoring.[17] Invasive methods include daily fingerpicks to draw blood, implanted glucometers under the skin. Noninvasive methods, requiring additional research, include soft contact lens to measure glucose levels from tears, retainers for saliva, microneedles for interstitial fluid, and wearables for sweat.

3.4 Research Objective

Here, we demonstrate the fabrication of an inexpensive microfluidic architecture with solution-processable electrodes for continuous glucose monitoring. The flexible

microfluidic system consisted of a pressure-sensitive adhesive microchannel between a polyimide (PI) and hydrophilic polyethylene terephthalate (PET) substrate for fast capillary-drive flow and integrated with an absorbent pad for controlled sweat evaporation. Electrochemical three-electrode systems were inkjet-printed from graphene and silver inks.[23,2,24] A low voltage, portable, and printed electrowetting valve was included on this design to illustrate the simplicity of customization for additional reagents.[25–28] This microfluidic device was then assessed for time-stamped sweat delivery of glucose through a polymer-based synthetic skin. This skin was designed with 50 μm pores at a distribution of 250 μm cm^{-2}, resembling the eccrine sweat glands that cover the human body and assessed for glucose diffusion and residence time of fluid within the skin. The amperometric glucose sensor was produced by electrodeposition of Prussian Blue (PB) on printed graphene and immobilized with glucose oxidase in a chitosan layer. The effect of perspiration rate on sensor performance was evaluated by adhering the microfluidic device onto the synthetic skin and testing at five flow rates between 1-5 μL/min. The glucose sensor demonstrated reproducibility within a range of 0.2 mM to 1 mM. Finally, this low-cost, easily fabricated microfluidic device offers a customizable design to accommodate single-use and continuous analyte measurements at various sweating flow rates for personalized health monitoring.

This research was funded through the Center for Hierarchical Manufacturing, the Center for Personalized Health Monitoring, and the Nano-Bio Manufacturing Consortium. This collaborative work was in thanks to Yiliang Zhou, Dr. Uzodinma Okoroanyanwu, Dr. Kenneth Carter, and Dr. James Watkins for their expertise in electrochemical sensors, and Anita Dey and Dr. Johnathan Rothstein for their knowledge

of microfluidic and synthetic skin systems. Furthermore, Dr. Karen Kalmakis, Dr. Lisa Chiodo, Dr. Jerry Meyer from the UMass College of Nursing offered valuable insight and information into the development of a sweat and saliva sensor for medical applications.

3.5 Experimental Section

Polydimethylsiloxane (PDMS) was used to fabricate the synthetic skin created from a bottom base layer adhered to a thin membrane with pores. An SU8 master was produced by standard UV photolithography on a silicon wafer to a depth of 30 μm. Using a 10:1 ratio of elastomer to curing agent, PDMS (Sylgard 184, Dow Corning) was poured over the SU8 master and cured at 65°C overnight. The PDMS was peeled from the SU8 master and used for the synthetic skin base, which includes the two inlets, mixing channel, and microfluidic channels leading to the skin pores. Next, a sacrificial micromolding technique was used to produce the porous top layer.[29] By photolithography, a SU8 master of posts (50 μm high and 50 μm tall) was fabricated to mimic the size and distribution of human skin pores. A 10:1 ratio of DI water to poly(vinyl alcohol) (PVA, Sigma-Aldrich) was spin coated over a silicon wafer and heated at 95°C for 5 min to achieve a 750 μm thickness. PDMS was spincoated over the PVA layer at a thickness of 50 μm and cured. The silicon wafer with PVA and PDMS was dipped into water, dissolving the sacrificial PVA layer and exposing the porous PDMS membrane. To bond the base and membrane layers, both were exposed to corona plasma and aligned under an optical microscope, pressed together. After an hour of wait time, the synthetic skin was complete.

Well-dispersed graphene ink was composed of graphene flakes exfoliated from graphite by probe ultrasonication and capped by nitrocellulose, as discussed earlier.[30,31] The graphene dispersion used for printing was 16.7 mg mL^{-1} graphene/nitrocellulose in a solution of 4:1 ethyl lactate (Sigma-Aldrich) to alpha-terpineol (Alfa-Aesar) by volume. Metalon JSB-25HV nanosilver ink with ~25 wt% silver in an aqueous dispersion was used for printing. A Dimatix DMP-2850 (Fujifilm) inkjet printer with a 10 pL cartridge was used to print the graphene and silver patterns on polyimide (PI, Kapton, American Durafilm) polyimide (PI) and polyethylene terephthalate (PET, Novele, Novacentrix) films. For graphene patterns, 25 layers of ink were printed using 16 nozzles and annealed at 350°C for 30 min until conductive. For silver patterns, 2 layers of ink were printed using 4 nozzles for the sweat sensors and 1 layer for the electrowetting valve. The printed silver was annealed at 125°C on Novacentrix Novele PET for 5 min and 285°C on PI until conductive. Both graphene and silver inks were printed using 20 μm drop spacing and 28 V jetting voltage.

The working electrode was composed of inkjet-printed graphene on polyimide with electrodeposited Prussian blue. For the electrodeposition, a constant potential of 0.4 V (vs. Ag/AgCl) was applied to the graphene for 120 s. The deposition bath was composed of 2.5 mM $FeCl_3$, 100 mM KCl, 2.5 mM $K_3Fe(CN)_6$, and 100 mM HCl. The glucose sensor working electrode was obtained by drop-casting 5 μL of the glucose oxidase/chitosan/glutaraldehyde solution onto the graphene/PB electrode. The preparation of this solution is listed as follows: 1% chitosan solution was first prepared by dissolving chitosan in 2% acetic acid with magnetic stirring; Then, this chitosan solution was mixed thoroughly with glucose oxidase solution (100 mg ml^{-1} in artificial

perspiration, pH 4.5) and 0.25 wt% glutaraldehyde solution in the volume ratio of 1:2:1. These modified electrodes were refrigerated at 4 °C, prior to testing.

An Ag/AgCl electrode was used as a combined counter and reference electrode system, as demonstrated in previous literature.[32,33] A solution of ferric chloride (Copper Etchant Type CE -100, CHEMTREC) was diluted with DI water until 50 mM in concentration. The $FeCl_3$ solution was dropcast over the printed silver electrode to convert the top layer of Ag to AgCl. The reaction was quenched with water after 1 min and the Ag/AgCl allowed to air dry. All measurements used artificial perspiration (Pickering, pH 4.5) spiked with increasing concentrations of glucose. A glucose stock solution (0.1 M) was prepared in artificial perspiration (pH 4.5) then left at room temperature for about 24 h prior to use to ensure the formation of β-D-glucose. The glucose solution was then diluted with artificial sweat to achieve the necessary specific concentrations for testing.

The microfluidic devices were fabricated from PI (25 um thickness), pressure-sensitive adhesive (PSA, ARCare 92712, 48 um thickness), and PET (140 um thickness) layers, which were individually laser cut according to CAD designs. The microfluidic strip was cut to 78 μm by 18 μm. A single layer of PSA was used to produce the 1 mm microchannel between the PI and PET films. To offer additional mechanical stability, a layer of PET sandwiched between two layers of PSA was adhered to the base of the microfluidic device. During testing, a thin piece of PDMS was adhered by corona treatment around the synthetic skin pores to prevent the formation of leaks or bubbles into the microfluidic device. The microfluidic strip was pressed onto the PDMS for the PSA to adhere with the surface.

For electrochemical measurements, the microfluidic device was connected to an electrochemical analyzer (CHI 660E, CH Instruments) for sensing measurements. For glucose testing, amperometric measurements were conducted on a two-electrode system using a current of −0.05 V versus Ag/AgCl electrode. For the cortisol sensor, a three-electrode. The spectra of cyclic voltammetry (CV) curves in characterization of electrode modification were recorded in PBS solution (10 mM, pH 7.4) containing a 5 mM $Fe(CN)_6^{3-/4-}$ redox probe.

Lastly, scanning electron microscopy and electron (SEM) and energy dispersive x-ray spectroscopy (EDS, FEI Magellan 400 XHR) were used to characterize the surface of the printed and modified electrodes.

3.6 Synthetic Skin Development

A flexible synthetic skin was designed to better understand time-stamped sweat acquisition for temporal biomarker measurements. Many research studies focus on human research to realize the ability of fabricated sweat sensor devices; however, these are subject to the perspiration of a particular individual with no control of the sweating rate. Systematic testing of a sweat-based sensor requires accurate measurements of the sensor at a variety of sweating rates and biomarker concentrations.

Here, we developed a PDMS-based synthetic skin composed of a base layer and a thin membrane using UV photolithography and soft lithography fabrication as shown in Figure 41. The base layer included two inlets, which led to a mixing channel to allow for the introduction of artificial sweat into one inlet and sweat spiked with a biomarker of interest into the other inlet. This mixing channel was designed for uniform mixing at both

low and high flow rates. After the mixing channel, the fluid is divided into several separate channels prior to reaching the sweat pores. These circuitous pathways are used to allow for the same pressure drop across each channel to ensure fluid will reach each sweat pores at similar times. Next, a 50 μm thick porous membrane serves as synthetic skin pores with 72 pores placed over a circular area with a diameter of 3 mm. The size of these pores is 50 μm and the distribution is 250 pores/cm^2, which mimic human skin.

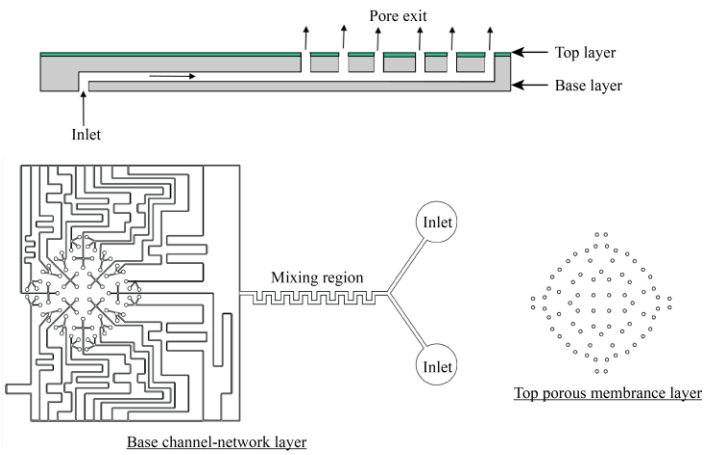

Figure 41. Synthetic skin illustration. (Top) Cross-sectional schematic of sweat flow from inlet of skin to outlet at the skin pores. (Bottom) Top-view illustration of the two layers used to produce the PDMS-based synthetic skin, including a lower layer for sweat mixing and delivery though equidistance channels and an upper layer with 50 μm outlet pores.

To further understand the ability of the synthetic skin, the effects of diffusion during flow in the microchannels was considered mathematically and experimentally. The diffusion of a plug of fluid with known concentration of glucose molecules is illustrated in Figure 42. The glucose will diffuse laterally as it reaches contact with the sides of microchannels within the synthetic skin, and the final microfluidic device. However, the velocity of the sweat within the channel will vary according to the location within the channel: the velocity will increase in the center of the channel and decrease at the edges. Similarly, glucose molecules introduced into the flow will be affected by this

non-uniformity depending on their location within the sweat. Therefore, convectional diffusion will occur at along the length of the microchannel due to the shear flow within the length of microchannel as well. Both these types of diffusion must be considered to gain an accurate understanding of diffusion of the glucose concentration with regard to flow rate at the surface of the skin pores.

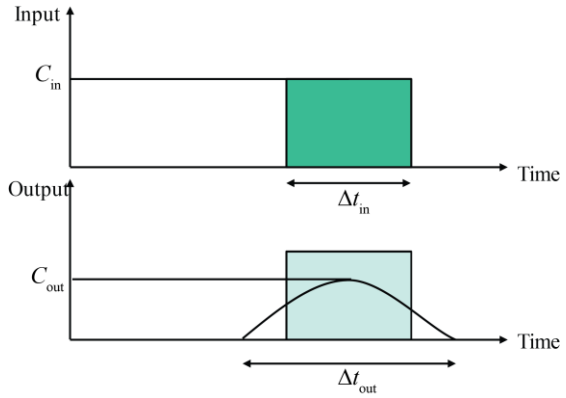

Figure 42. Representative illustration of the glucose concentration within sweat at the inlet and outlet of the synthetic skin. Due to diffusion of glucose within the microchannels, the concentration of glucose within a representative plug of sweat will decrease and require a longer exit time compared to the inlet concentration and time.

In particular, the Taylor-Aris dispersion theory can be used to understand the relationship between these types of diffusion and calculate important parameters of interest. Building on Fick's law of diffusion, an apparent effective diffusivity can be calculated from the mass flux across the channel, given by Equation 1.

$$Q = UC_m + D_{TA}\frac{\delta C_m}{\delta x} \qquad [1]$$

Here, Q (mol/ m^2 s) is the mass flux, U (m/s) is the velocity, D_{TA} (s) is the Taylor-Aris dispersion coefficient, C_m (mol/m^3) is the mean concentration across the distance, and x (m) is the length of the channel. In particular, the Taylor-Aris dispersion coefficient (D_{TA} (s)) accounts for both lateral and conventional diffusion within a channel,[34]

$$D_{\mathrm{TA}} = D + \frac{d^2 {U_c}^2}{192D} \quad [2]$$

where D (m^2/s) is the diffusion coefficient of glucose, d (m) is the hydraulic diameter, and U_c (m/s) is the channel velocity. Using the calculated dispersion coefficient, the dispersion time, given by $t_{dispersion}$ (s), for a representative plug of fluid can be calculated from Equation 3 below,

$$t_{\mathrm{dispersion}} = \frac{2\sqrt{D_{\mathrm{TA}}\, t_c}}{U_c} \quad [3]$$

where t_c is the time interval of the plug of fluid of known concentration C_o. The assumption is that fluid at the exit pores will have a mean concentration, C_{out} equal to 90% the original concentration, C_{in}, as a result of diffusion within the channel. Therefore, the time interval for the plug can be estimated. For 1 μL/min, this time interval would be 50 s and will continue to decrease as the flow rate increases.

Next, the residence times of fluid within the synthetic skin were explored as this is necessary to realize the time-stamping of sweat in the channels. These are again calculated using the assumption that the final concentration being 90% of the initial concentration with x equal to the entire distance from inlet to outlet of the microchannel. As shown in Figure 43, flow rates between 0.05 μL/min to 5 μL/min were evaluated for their residence time and plug spread. An absorbent pad was placed at the skin pores exit to determine when the fluid reached the outlet of the synthetic skin. The residence time within the channel was plotted with respect to flow rate, which was found to be approximately related to the inverse relationship with the flow rate. Additionally, the concentration of the plug spread was determined by the outlet time minus the inlet time

divided by the inlet time and multiplied by 100. For high flow rates, the plug spread approached zero.

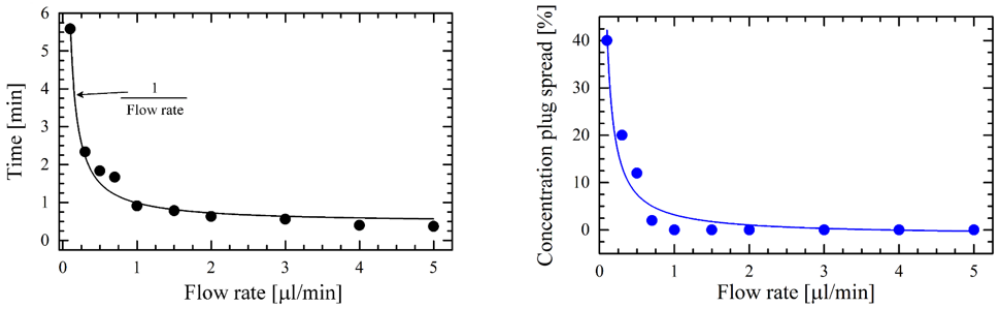

Figure 43. Experimental residence times of fluid within the synthetic skin at flow rates between 1-5 µL/min. (Left) The time for fluid to exit the pores of the synthetic skin, which can be approximated by the inverse of the flow rate. (Right) The percentage of plug spread have been plotted against a range of flow rates using colored dye with the synthetic skin.

3.7 Adhesive-based Microfluidic Fabrication

Next, the microfluidic channel was designed, which would support the printed sensor electrodes and adhere to the synthetic skin. A schematic of the final expected design is shown in Figure 44. The microfluidic design was optimized for (1) material selection, (2) microchannel dimensions, (3) wicking/absorbing pads, (4) mechanical stability, and (5) bubble prevention.

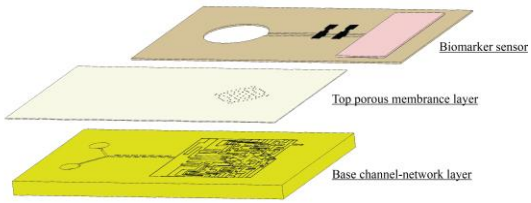

Figure 44. Schematic of microfluidic device integrated with synthetic skin. The porous synthetic skin is developed using UV photolithography and adhered to the thin top layer membrane by oxygen plasma. The printed microfluidic device with printed sensors is placed on top of synthetic skin components using a skin adhesive.

First, the material selection and microchannel dimensions were considered. The top substrate was chosen to be Novele PET provided by Novacentrix. This PET has a uniform microporous coating, which allows for very high hydrophilicity even after immersion in water and ethanol. This hydrophilic PET accommodates fast capillary-driven flow, which is necessary for this device to operate at both low and high sweating flow rates. The bottom layer was selected to be polyimide, also known as Kapton, which can withstand high-temperature annealing required for the sensor electrode fabrication. For a microfluidic channel, the most straightforward, simple, and fast design is a rectangular design. This was produced by laser cutting a design drawn in CAD onto PSA. The PSA was then sandwiched between the top and bottom substrates to produce a microchannel.

The channel widths considered were 500 μm, 1 mm, 2 mm, and 3 mm. Sweat dyed pink with Rhodamine B was introduced into the channel from the synthetic skin and observed as shown in Figure 45. For large channel widths of 2 mm and 3mm, the fluid flow travelled along the edges of the channels and resulted in early channel collapse. The smallest width of 500 μm demonstrated rough edges as a result of interference from the laser cutter at such a small distance. Therefore, the channel width of 1 mm was selected for the device; however, there was still some concerns of bubble formation within the channel, resulting for leakage or twisting of the device. From here, stagnation pressure would build in front of the bubble and result in a slower flow rate or complete blockage of the channel. Finally, the channel height was examined by considering the use of one PSA layer or two. Two layers would allow for fast flow of sweat without the concern of the sensor electrodes squeezing or preventing the fluid, while one layer would be best for

low flow rates of sweat. Therefore, one layer of PSA was used and the height of the sensor electrodes was controlled to be lower than 40 μm.

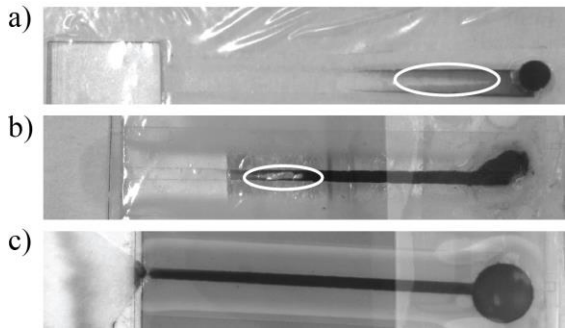

Figure 45. Microfluidic channel width optimization. (a) Laser cut PSA channel width of 3 mm, demonstrating channel collapse and slow flow to reach the absorbent pad. (b) 1 mm channel width revealing a bubble in the center of the channel. (c) Optimized 1 mm channel width showing fluid flow through the device without bubble formation.

The requirement of a wicking pad and absorbent pad were then explored on the microfluidic system attached to the synthetic skin. A wicking pad at the start of the device may offer an advantage to help the collection of sweat over a period of time. The following four conditions were tested: no wicking pad, Whatman 1 filter paper, Whatman 17 glass fiber, and nitrocellulose paper. Circular wicking pads were cut from these materials and placed over the sweat pores and under the microfluidic device. Artificial sweat was introduced into the synthetic skin and the time to reach the microfluidic channel was observed. All three wicking pads demonstrated leakage near the skin pores as shown in Figure 46 and resulted in very slow flow of sweat into the microfluidic device. The sweat leaking from the wicking pad also impaired the adhesion of the microfluidic device on the PDMS surface over time and resulted in the forming of small bubbles, on occasion. Therefore, no wicking pad was used for the final microfluidic device strip.

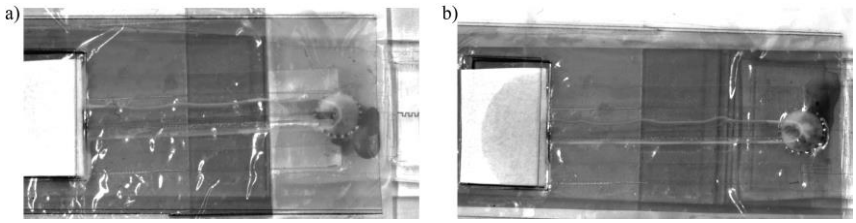

Figure 46. Sweat leakage. (a) Whatman 17 wicking pad resulted in increased leakage of the simulated sweat around the inlet, preventing flow through the microchannel. (b) Nitrocellulose wicking pad showed flow through the microchannel with leakage prominent near the inlet.

Another concern with the microfluidic device was the collapse of the microfluidic channel and flow near the edges of the channel, even using the 1 mm channel width. This result was due to the very thin polyimide layer used as the bottom layer, which had low mechanical stability. To strengthen this layer, an additional PET layer with a top and bottom layer of PSA was placed under the polyimide layer. While this increased the thickness of the overall device, it was not shown to hinder the bendability of the device.

Finally, to prevent the formation of bubbles within the channel, a thin layer of PDMS was placed between the synthetic skin and the microfluidic device as shown in Figure 47. The bubbles would greatly affect the sensor measurements by preventing the flow of fluid at low flow rates or becoming entrapped on the hydrophobic sensor electrode surface. Bubble formation within microfluidics channels and devices is a common challenge in this field of research. Gas bubbles are caused by diffusion of gas from the pumping solution or tubing, vibrations or perturbations of the microfluidics, and changes in temperature or pressure of the system. [35,36]

While it is difficult to remove bubbles following their formation, it is easier to prevent the creation of bubbles in the channel. These can occur by introduction from the syringe pumps leading to the synthetic skin, or from the connection of the microfluidic

device to the synthetic skin. Prior to use, the filled syringes were carefully tapped to remove any trapped bubbles from the solution. Next, a thin PDMS layer was placed over the porous skin membrane and offered a second layer of protection from leaking and entrapping air bubbles into the channels. A drawback of the porous skin membrane was that adhesive pressure from the microfluidic device would pull apart the two layers used to create the skin. This issue would cause small leaks within the skin and at the interface between the skin and the device. The added PDMS strip offered protection to the thin synthetic skin and prevented leaks. Additionally, the devices were prewet with sweat prior to testing to remove air from within the channel before testing. Lastly, a sequence of images demonstrating dyed fluid entering from the skin pores and through the microfluidic channel of the device is shown in Figure 48 below.

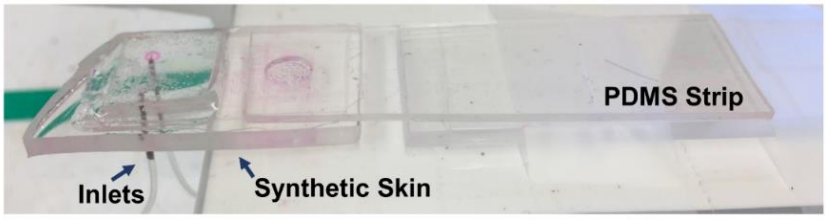

Figure 47. Synthetic skin with PDMS layer. A thin PDMS layer was adhered to the synthetic skin using oxygen plasma to prevent the formation of bubbles or leakage around the transition of fluid from the skin to the microfluidic device.

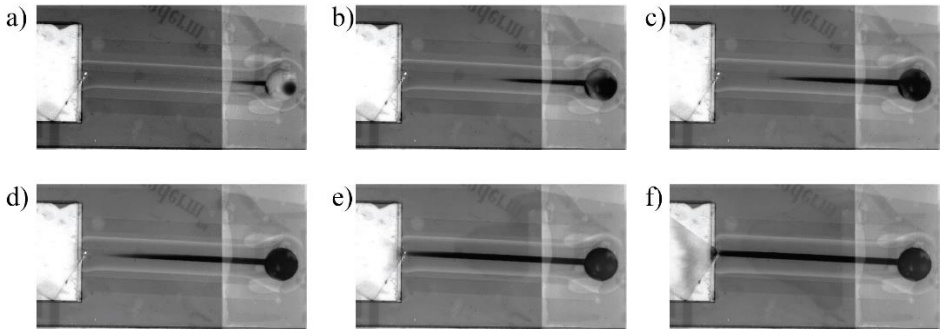

Figure 48. Fluid flowing through the microfluidic device with a 1 mm channel width at specific time points.

3.8 Printed Sensor Electrodes

Following design optimization, the final microfluidic device consisted of a layer of PSA to create the microchannel between a top hydrophilic layer of PET and a bottom polyimide layer. The polyimide layer can withstand high-temperature annealing, which is necessary for the fabrication of printed sensor electrodes. A side-view schematic of the microfluidic device with the printed electrodes is shown in Figure 49. The size of the microfluidic strip was 2.5 in width (comparable to a standard Band-Aid).

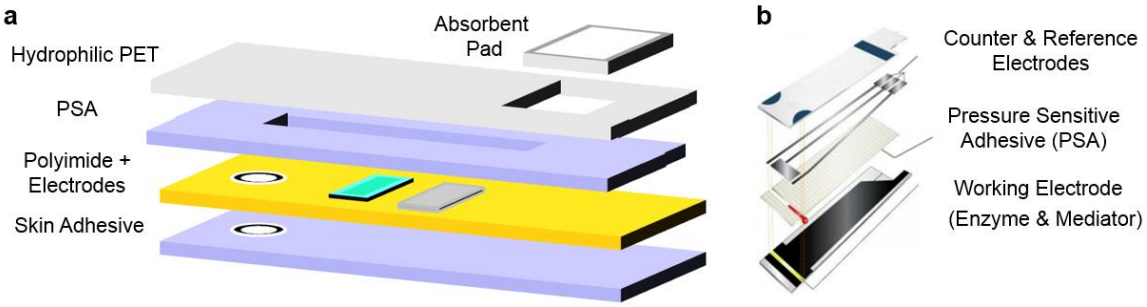

Figure 49. Schematic of microfluidic device fabrication. (a) Fabrication assembly of microfluidic device, including skin adhesive, polyimide substrate, PSA microchannel, hydrophilic PET substrate, and replaceable absorbent pad, (b) Common paperfluidic glucose test strip with similar design features.

For an electrochemical sensor, three conductive electrodes are needed: working, counter, and reference. The working electrode contains the sensing material with the ability to target and measure the biomarker or analyte of interest. The base of this electrode is usually produced from gold, silver, or platinum to allow for fast electron transfer. The counter electrode is used to complete the electrochemical circuit, is commonly made of an inert material, and does not participate in the reaction. Lastly, the reference electrode has a steady electrode properties, which are well-known, allowing it to serve as a reference to which very low voltage is applied.

For the printed glucose sensors, solution-processable graphene ink developed in Dr. Mark Hersam's research group was used for the base of the working electrode. This graphene ink is similar to the ink discussed in Chapter 1; however uses nitrocellulose as an ink stabilizer, compared with ethylcellulose. By using nitrocellulose as the capping agent, the ink is more water-resistant and shows better adhesion with polyimide films. The novel graphene ink stabilized by nitrocellulose was shown to be inkjet-printed and gravure-printed in previous studies. The graphene ink was printed at 20 μm drop size spacing at a jetting voltage of 28 V from a 10 pL cartridge. The printed design was drawn using a CAD program to print within the laser cut substrate. To achieve a highly conductive electrode, twenty-five layers of graphene ink were printed onto the Kapton substrate using all 16 inkjet printing nozzles to increase the thickness of the graphene ink. Following inkjet printing, the graphene ink is annealed at 350°C for 30-60min to degrade the nitrocellulose binder, allowing for better flake-to-flake contact and higher conductance (50-80 Ohm).

For the sensor counter and reference electrodes, silver ink from Novacentrix (JSB25HV) was printed. This ink requires a ten min thermal annealing step at 300°C for the silver nanoparticles to coalesce and become conductive on polyimide film. For the electrodes, two layers of silver were printed to obtain the desired conductivity level. This silver ink was also used as the conductive connectors from the electrodes to the edge of the microfluidic strip. A common reference electrode for printed sensors is Ag/AgCl. Here, the top layer of printed silver is converted to AgCl. This was completed by dropcasting diluted ferric chloride over the sensor pad and quenching the reaction with water after 1 min. As shown in Figure 50 below, the final Ag/AgCl electrode is a dark

gray color compared to the white silver connectors. For the glucose sensor, the reference and counter electrodes were combined together as a pseudo-reference electrode. This was accomplished to decrease fabrication time and require less space on the device.

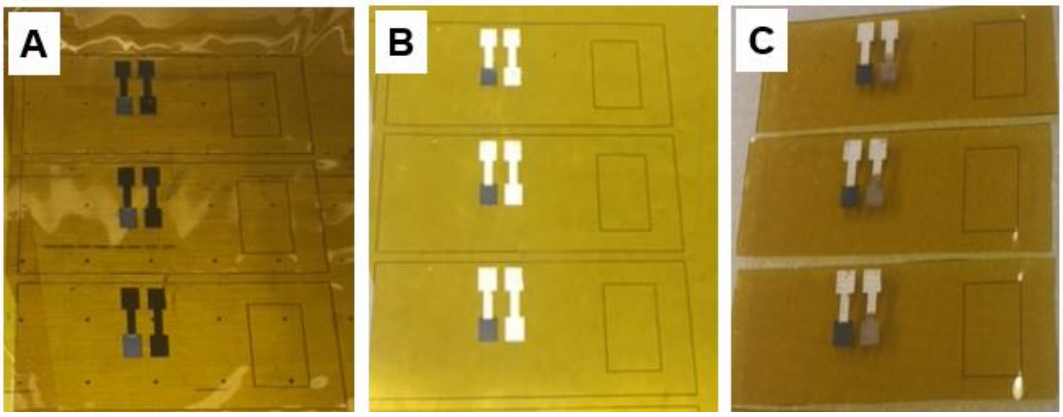

Figure 50. Ag/AgCl electrode fabrication. a) Inkjet-printed graphene and silver patterns. (b) Thermally treated graphene and silver patterns on polyimide substrate. c) Silver electrode modified with ferric chloride to become Ag/AgCl reference and counter electrode.

The electrode surfaces were characterized by scanning electron microscopy (SEM) and energy dispersive spectroscopy (EDS). As shown in Figure 51 (top), high-resolution SEM images show the original graphene, silver, and Ag/AgCl surfaces used for the sensor electrode. For the SEM images, electrodes printed on polyimide were coated with 2 nm of Pt for imaging without beam damage to the materials. For the EDS spectrums, these samples were printed on to SiO_2 surfaces to allow for imaging at high voltages and accelerating voltages necessary for this measurement. The EDS spectrum demonstrate predominantly carbon for the graphene sample, mainly silver for the annealed printed silver sample, and silver and chlorine for the Ag/AgCl modified sample.

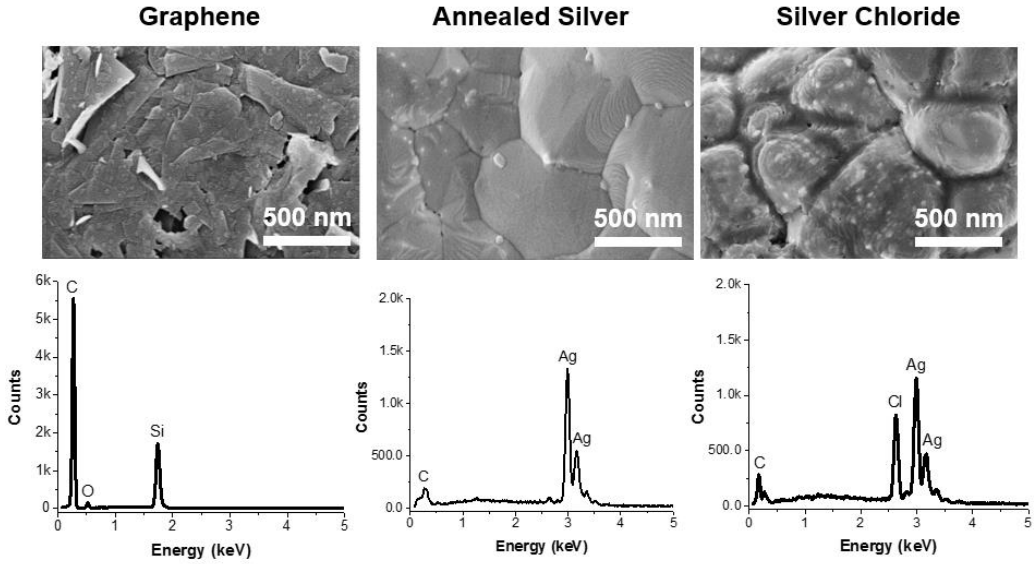

Figure 51. Electrode SEM Images and EDS Spectra. (Top) High-resolution SEM images of inkjet-printed graphene, silver, and Ag/AgCl electrode surfaces on polyimide substrates following thermal treatment. Samples were sputtered with 2 nm Pt coating for imaging. (b) EDS Spectra of graphene, silver, and silver chloride on silicon substrates. The graphene electrode demonstrated predominately carbon, the silver chloride predominately silver, and the Ag/AgCl electrode predominately silver and chlorine.

3.9 Integrated Microfluidic Design

Once the sensor electrodes were printed on the microfluidic device and assembled, it was connected with the electrochemical analyzer and synthetic skin. A camera was placed above the setup for video measurements, as shown in Figure 52. Artificial sweat and sweat spiked with glucose was pushed through separate syringe pumps connected to the synthetic skin. The microfluidic device with printed electrochemical sensors was adhered to the synthetic skin, thus fully integrating the test strip to examine continuous glucose monitoring.

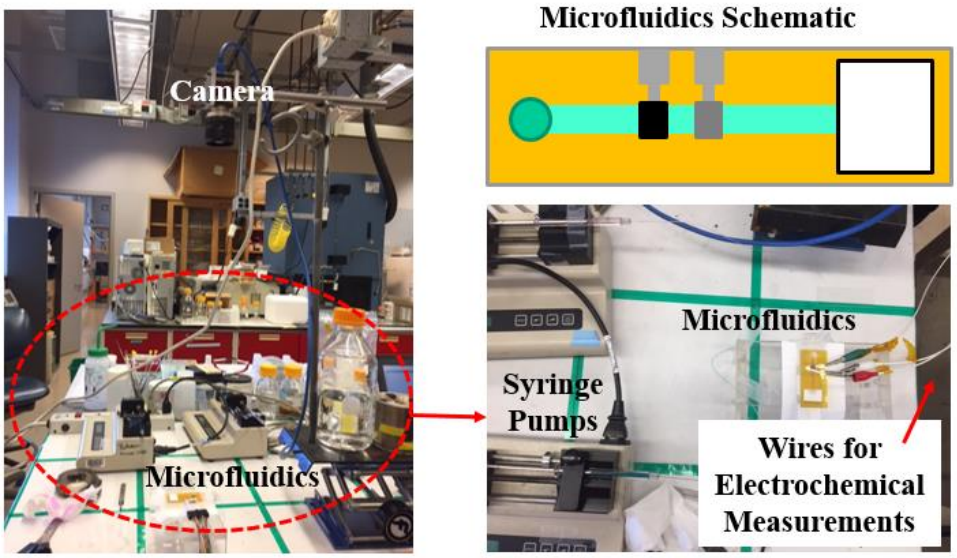

Figure 52. Integration of Microfluidics, Sweat Sensor, Simulated Skin. (Left) Photo of experimental setup, (Right) Image of connections required for the measurements, including wire to the electrochemical analyzer and microfluidic tubing to the syringe pumps.

To visualize the fluid flow within the microfluidic device, artificial sweat was pumped in through two inlets to synthetic skin and imaged. A sequence of photos were taken as sweat flowed through the device at specific time points as shown in Figure 53. The increasing fluid flow is demonstrated by the filling of the absorbent pad on the right side of the microchannel. To account for increased sweating rates, the absorbent pads can be easily switched out and replaced for new pads. One challenge with this design is the noticeable crimping of the polymeric substrate under the force of the alligator clips connecting the electrodes to the analyzer. This issue was reduced by adding a thicker piece of PET directly under the printed electrodes to increase stability.

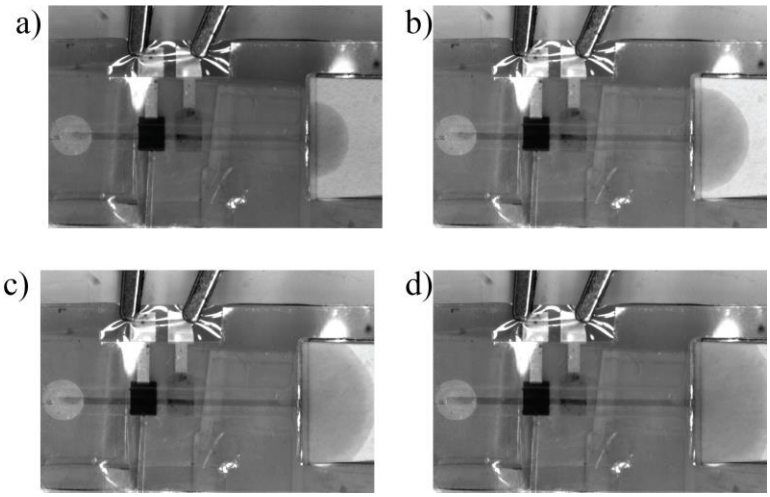

Figure 53. Fluid flow through microfluidic sensor device from the synthetic skin. (a-d) Increased fluid passing through the device without leakage as demonstrated by the filling of the absorbent pad.

3.10 Hydrogen Peroxide Microfluidic Data

Glucose biosensors rely on an enzymatic redox reaction where glucose oxidase will bind to glucose, oxidizing the molecule into glucose oxidase (GOx) by producing the byproduct of hydrogen peroxide (H_2O_2), as shown below.

$$\text{D-Glucose} + H_2O + O_2 \xrightarrow{\text{GOx}} \text{D-Gluconic Acid} + H_2O_2$$

The concentration of hydrogen peroxide can be directly detected by the conductive electrodes of the electrochemical sensor, by measuring the current produced during the redox reaction. Using this information, the glucose concentration can be indirectly calculated through measuring the generation of peroxide in the solution.

Based on this concept, the printed glucose sensor consisted of graphene as the working electrode and a combined Ag/AgCl electrode as the counter and reference. This straightforward sensor served as an ideal setup to design the individual aspects of the microfluidic device without introducing actual glucose or simulated sweat into the

device. Instead, a PBS buffer solution with varying concentration of hydrogen peroxide was used to optimize the microfluidic substrate materials, channel dimensions, electrode pad sizes, adhesive layers, and CAD design.

First, the graphene working electrode was measured in a beaker setup to characterize its performance for a simple peroxide sensor. A standard Ag/AgCl reference electrode and Pt counter electrode were used to demonstrate the printed graphene electrode would function as a stable working electrode. As shown in Figure 54, the printed graphene detected injection of hydrogen peroxide into the solution at increasing concentrations, which can be reduced at a -0.5 V potential.

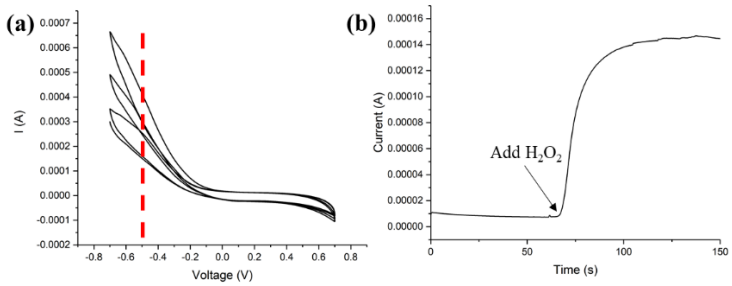

Figure 54. Hydrogen peroxide sensing within beaker. (a) CV curve of graphene working electrode for 1 mM, 2 mM, and 3 mM hydrogen peroxide. (b) Hydrogen peroxide sensing using standard three electrode system at -0.5 V.

The reference and counter electrodes were then printed using silver ink and tested for adhesion, stability, and performance. For commercial glucose test strips, these two electrodes are commonly combined together to decrease cost and fabrication time. However, the printed Ag/AgCl electrode demonstrated degradation under voltage conditions required to detect peroxide. As shown in Figure 55b, there is a noticeable color change on the Ag/AgCl electrode from grey to black after the application of voltage, due to the oxidation of silver. This instability can also be verified by a sudden decrease in current over time on Figure 55b. However, this damage was not apparent at

the lower voltage of -0.05, demonstrated by the constant measured current over time in Figure 55a. Therefore, a working electrode was modified with a mediator layer to detect peroxide at a lower voltage and prevent damage to the inkjet-printed sensor.

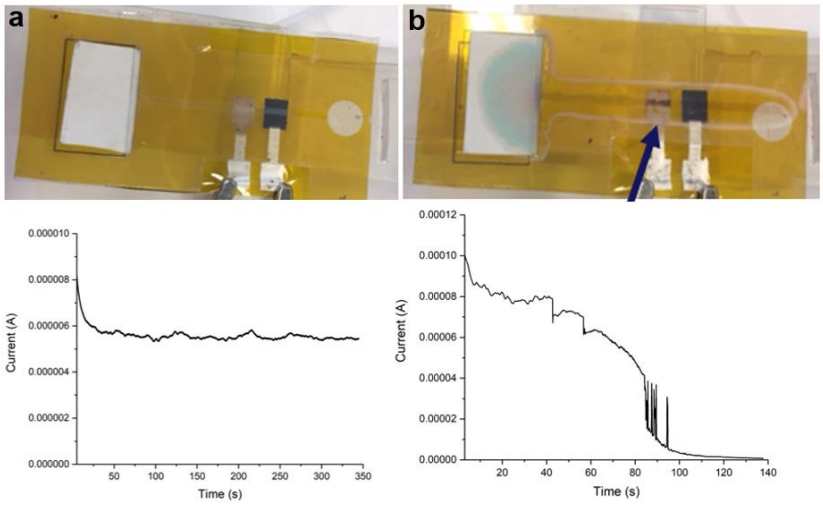

Figure 55. Damage to reference/counter electrode at high voltage. (a) Image of microfluidic device with response curve with an applied potential of -0.05 V. (b) Image of device with degradation evident on Ag/AgCl electrode due to high applied voltage of 0.5 V.

A common mediator layer used for electrochemical sensors over the past decade is Prussian Blue. A thin film of this material is coated onto the working electrode to act as a catalyst for hydrogen peroxide reduction. This occurs by causing a redox reaction converting Prussian Blue to Prussian White that is dependent on the oxidation of glucose by GOx, as shown in Figure 56. Prussian Blue can be electrodeposited onto the surface of the electrode, allowing for solution-processable coating of this mediator layer. In particular, the deposition thickness of the mediator layer affects the sensor response time, where a thicker layer will require additional time to pass electrons to the electrode. The lower reduction potential for Prussian blue also serves to limit possible side reactions during sensing with undesired biomolecules, such as uric acid or ascorbic acid, and

improves the sensor selectivity. Finally, this electrocatalyst is known to be highly stable for long periods of time.[37]

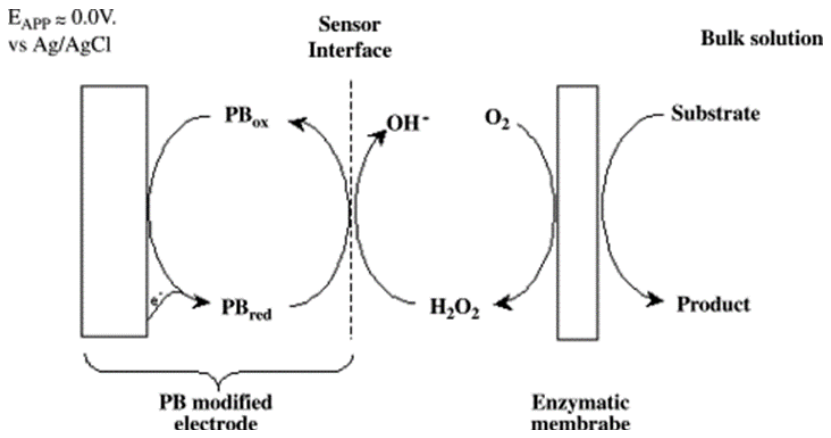

Figure 56. Illustration of Prussian Blue mediator layer for enzymatic sensor.[37]

To improve the microfluidic device system for low voltage testing, a thin layer of Prussian Blue was electrodeposited onto the surface of the printed graphene electrode. To deposit exclusively onto the printed graphene pad, the silver connectors were printed to the side of the device to prevent contact with the electrodeposition solution. The electrolyte used for deposition was composed of 2.5 mM $FeCl_3$, 2.5 mM $K_3Fe(CN)_6$, 0.1 M KCl, and 0.1 M HCl with an applied voltage of 0.4 V for 60 s. Following the deposition, a blue coating was visible on the surface of the graphene. Cyclic voltammetry demonstrated oxidation and reduction peaks of hydrogen peroxide close to 0 V for the modified working electrode. The Prussian Blue-modified graphene electrode was tested within a beaker using standard electrodes at a voltage of -0.05 V as shown in Figure 57b. This modified Prussian Blue/graphene working electrode demonstrated the capability to detect injections of increasing levels of hydrogen peroxide into the buffer solution.

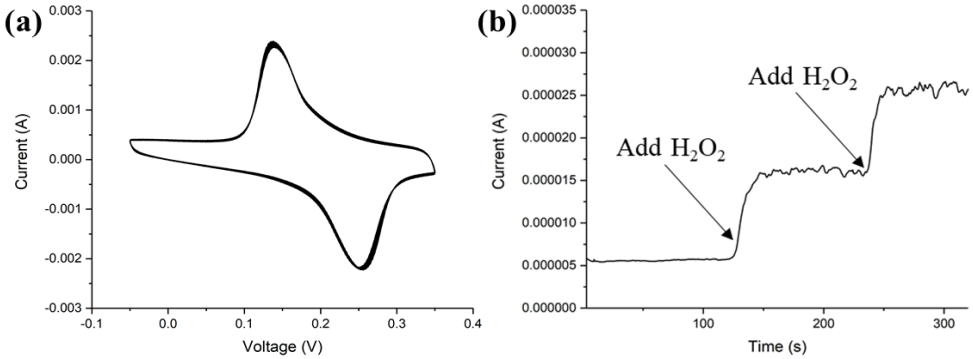

Figure 57. Hydrogen peroxide sensing. (a) Cyclic voltammetry of PB-modified electrode in buffer solution after 50 cycles. (b) Amperometric response curve of the PB-modified graphene electrode with successive H_2O_2 injection in a beaker system. The potential is applied at -0.05 V.

The Prussian Blue-modified graphene electrode was also examined by high-resolution SEM and EDS to understand the surface structure and composition of the material. As shown in Figure 58, the Prussian Blue forms a continuous coating over the surface of the graphene flakes, which are no longer visible from the surface. The EDS spectrum of the composite working electrode shows elemental peaks of nitrogen and iron, which are within the chemical structure of Prussian Blue.

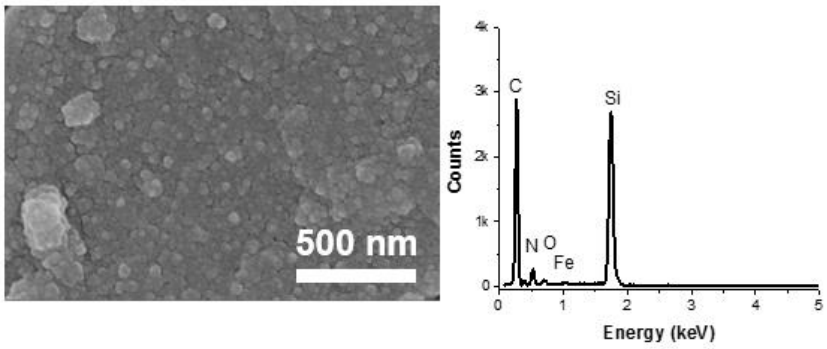

Figure 58. SEM and EDS of Prussian Blue. (Left) High-resolution SEM image of electrodeposited Prussian Blue on the inkjet-printed graphene electrode on a polyimide substrate. (Right) EDS spectrum revealing carbon from the graphene electrode and nitrogen, oxygen, and iron from the Prussian Blue, and silicon from the silicon wafer used for imaging.

3.11 Continuous Glucose Measurements

As the final step, glucose oxidase was immobilized on the surface of the Prussian Blue/graphene working electrode to measure the concentration of glucose in simulated sweat. The glucose oxidase enzyme was immobilized within a later of chitosan and glutaraldehyde drop-casted onto the Prussian Blue-modified graphene electrode. Once drop-casted, the solution was allowed to air dry overnight and then stored in a freezer at 4°C prior to testing to prevent enzyme degradation. The GOx/Prussian Blue/graphene working electrode was characterized using standard electrodes within a beaker to understand the cyclic voltammetry at various scan rates and calibration curve as shown in Figure 59. The cyclic voltammetric curve was measured at five scan rates to demonstrate stability of the working electrode. A glucose calibration curve was measured, indicating a linear response curve between 0.2 mM to 1 mM with a limit of detection of 10 µM. This range is of particular importance as it falls within the expected concentration of glucose in sweat for diabetic patients.

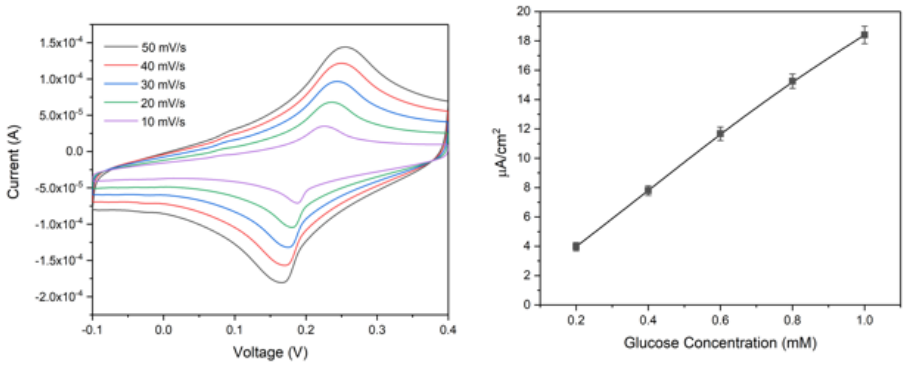

Figure 59. Cyclic voltammetric and calibration curves of glucose sensor. (Left) Measured cyclic voltammetric curves at increasing scan rates, (Right) Calibration curve of glucose sensor demonstrating linear detection relationship between 0.2 to 1.0 µA/cm^2.

The glucose sensor was integrated with the synthetic skin and tested in a constant flow system for repeatability and flow rate dependence. As shown in Figure 60, the

sensor demonstrates good performance and reproducible results over multiple injections of a low concentration of glucose within simulated sweat. For continuous monitoring of human sweat, one important concern is the flow rate of sweat which will vary depending on the physiological or emotional state of the individual. Therefore, five different flow rates of sweat were considered for the same microfluidic device, including 1 to 5 µL/min. For high flow rates between 2 µL/min to 5 µL/min, the current response reached the same saturation level, demonstrating good sensing capability and contact of the sweat solution with the electrodes. In comparison, for a flow rate of 1 µL/min, the fluid within the channel was unable to maintain complete contact with the electrodes, resulting in a lower than expected current response. Secondly, the faster flow rates demonstrate a faster response compared with lower flow rates. This result is due to the diffusion of glucose at various flow rates within the synthetic skin, the PDMS strip, and the microfluidic device to arrive at the sensor.

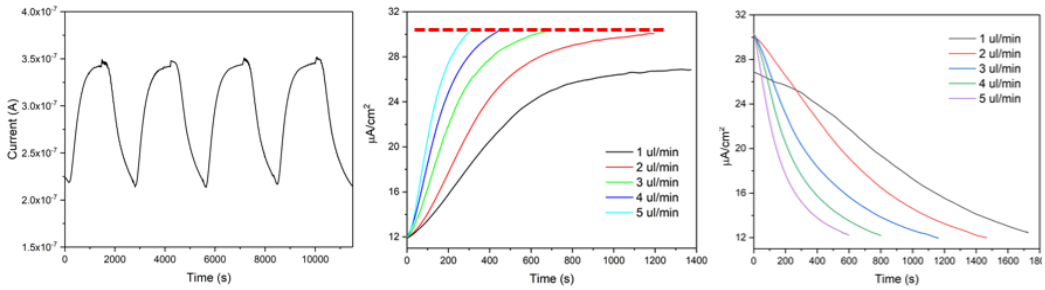

Figure 60. Microfluidic glucose sensor. (a) Repeatability of response curve for multiple injections of glucose in artificial sweat. (b,c) Response curves indicating detection of glucose using different flow rates of sweat.

The microfluidic glucose sensor also demonstrated the ability to detect different concentrations of glucose in a continuous manner, as shown in Figure 62. Here, the same microfluidic device was used to measure three different glucose concentrations: 0.2 mM, 0.35 mM, and 0.5 mM, indicated by the increasing current saturation of the sensor.

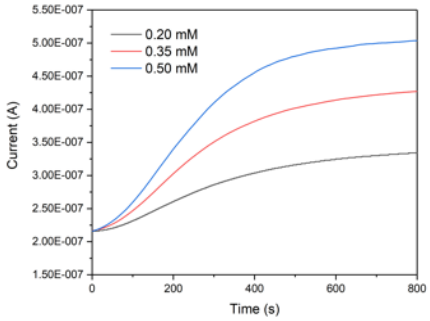

Figure 61. Continuous glucose monitoring. Current versus time plot of 0.2 mM, 0.35 mM, and 0.5 mM glucose within simulated sweat measured through the same microfluidic device.

3.12 Conclusions

In summary, we have demonstrated a low-cost, solution-processable microfluidic platform for the direct sensing of biomarkers from sweat. A synthetic skin was fabricated to mimic the size and distribution of skin pores on the human body, which allowed for the testing of different sweat flow rates between 1 μL/min to 5 μL/min. Solution-based graphene ink and silver ink served as conductive base layers for the electrochemical electrodes. The graphene working electrode was successfully modified with Prussian Blue to reduce the necessary voltage to reduce hydrogen peroxide, and the silver electrode was converted to a combined Ag/AgCl counter and reference electrode. In particular, these electrodes can be customized for different electrode size, shape, and thickness depending on the final application. The completed microfluidic device was adhered to the synthetic skin and tested for repeatability and response time. This sweat-based microfluidic biosensor device allows for a straightforward setup to test microfluidic sweat sensors and offers guidelines on bubble prevention, sensor fabrication, and flow rate adaptability. Furthermore, this microfluidic strip is compatible with scalable manufacturing for point-of-case diagnostics.

3.13 References

(1) Gao, B.; Elbaz, A.; He, Z.; Xie, Z.; Xu, H.; Liu, S.; Su, E.; Liu, H.; Gu, Z. Bioinspired Kirigami Fish-Based Highly Stretched Wearable Biosensor for Human Biochemical–Physiological Hybrid Monitoring. *Adv. Mater. Technol.* **2018**, *3* (4), 1–8.

(2) Martín, A.; Kim, J.; Kurniawan, J. F.; Sempionatto, J. R.; Moreto, J. R.; Tang, G.; Campbell, A. S.; Shin, A.; Lee, M. Y.; Liu, X.; Wang, J. Epidermal Microfluidic Electrochemical Detection System: Enhanced Sweat Sampling and Metabolite Detection. *ACS Sensors* **2017**, *2* (12), 1860–1868.

(3) Gao, W.; Emaminejad, S.; Nyein, H. Y. Y.; Challa, S.; Chen, K.; Peck, A.; Fahad, H. M.; Ota, H.; Shiraki, H.; Kiriya, D.; Lien, D.-H.; Brooks, G. A.; Davis, R. W.; Javey, A. Fully Integrated Wearable Sensor Arrays for Multiplexed in Situ Perspiration Analysis. *Nature* **2016**, *529* (7587), 509–514.

(4) Koh, A.; Kang, D.; Xue, Y.; Lee, S.; Pielak, R. M.; Kim, J.; Hwang, T.; Min, S.; Banks, A.; Manco, M. C.; Wang, L.; Ammann, K. R.; Jang, K.; Han, S.; Ghaffari, R.; Paik, U.; Slepian, M. J.; Huang, Y.; Rogers, J. A. A Soft, Wearable Microfluidic Device for the Capture, Storage, and Colorimetric Sensing of Sweat. *Sci Transl Med* **2017**, *8* (366), 1–14.

(5) Heikenfeld, J. Bioanalytical Devices: Technological Leap for Sweat Sensing. *Nature* **2016**, *529* (7587), 475–476.

(6) Heikenfeld, J. Non-Invasive Analyte Access and Sensing through Eccrine Sweat: Challenges and Outlook circa 2016. *Electroanalysis* **2016**, n/a-n/a.

(7) Sim, J. K.; Yoon, S.; Cho, Y. H. Wearable Sweat Rate Sensors for Human Thermal Comfort Monitoring. *Sci. Rep.* **2018**, *8* (1), 1–11.

(8) Oh, S. Y.; Hong, S. Y.; Jeong, Y. R.; Yun, J.; Park, H.; Jin, S. W.; Lee, G.; Oh, J. H.; Lee, H.; Lee, S. S.; Ha, J. S. Skin-Attachable, Stretchable Electrochemical Sweat Sensor for Glucose and pH Detection. *ACS Appl. Mater. Interfaces* **2018**, *10* (16), 13729–13740.

(9) Coyle, S.; Morris, D.; Lau, K. T.; Diamond, D.; Di Francesco, F.; Taccini, N.; Trivella, M. G.; Costanzo, D.; Salvo, P.; Porchet, J. A.; Luprano, J. Textile Sensors to Measure Sweat pH and Sweat-Rate during Exercise. *Pervasive Comput. Technol. Heal. 2009. PervasiveHealth 2009. 3rd Int. Conf.* **2009**, 4–9.

(10) Rose, D. P.; Ratterman, M. E.; Griffin, D. K.; Hou, L.; Kelley-Loughnane, N.; Naik, R. R.; Hagen, J. A.; Papautsky, I.; Heikenfeld, J. C. Adhesive RFID Sensor Patch for Monitoring of Sweat Electrolytes. *IEEE Trans. Biomed. Eng.* **2015**, *62* (6), 1457–1465.

(11) Emaminejad, S.; Gao, W.; Wu, E.; Davies, Z. A.; Yin Yin Nyein, H.; Challa, S.; Ryan, S. P.; Fahad, H. M.; Chen, K.; Shahpar, Z.; Talebi, S.; Milla, C.; Javey, A.; Davis, R. W. Autonomous Sweat Extraction and Analysis Applied to Cystic Fibrosis and Glucose Monitoring Using a Fully Integrated Wearable Platform. *Proc. Natl. Acad. Sci.* **2017**, *114* (18), 4625–4630.

(12) Twine, N. B.; Norton, R. M.; Brothers, M. C.; Hauke, A.; Gomez, E. F.; Heikenfeld, J. Open Nanofluidic Films with Rapid Transport and No Analyte Exchange for Ultra-Low Sample Volumes. *Lab Chip* **2018**.

(13) Kaushik, A.; Vasudev, A.; Arya, S. K.; Pasha, S. K.; Bhansali, S. Recent Advances in Cortisol Sensing Technologies for Point-of-Care Application. *Biosens. Bioelectron.* **2014**, *53* (October), 499–512.

(14) Singh, A.; Kaushik, A.; Kumar, R.; Nair, M.; Bhansali, S. Electrochemical Sensing of Cortisol: A Recent Update. *Appl. Biochem. Biotechnol.* **2014**, *174* (3), 1115–1126.

(15) Kim, K. S.; Lim, S. R.; Kim, S. E.; Lee, J. Y.; Chung, C. H.; Choe, W. S.; Yoo, P. J. Highly Sensitive and Selective Electrochemical Cortisol Sensor Using Bifunctional Protein Interlayer-Modified Graphene Electrodes. *Sensors Actuators, B Chem.* **2017**, *242*, 1121–1128.

(16) Lee, H.; Song, C.; Hong, Y. S.; Kim, M. S.; Cho, H. R.; Kang, T.; Shin, K.; Choi, S. H.; Hyeon, T.; Kim, D.-H. Wearable/disposable Sweat-Based Glucose Monitoring Device with Multistage Transdermal Drug Delivery Module. *Sci. Adv.* **2017**, *3* (3), e1601314.

(17) Lee, H.; Hong, Y. J.; Baik, S.; Hyeon, T.; Kim, D. H. Enzyme-Based Glucose Sensor: From Invasive to Wearable Device. *Adv. Healthc. Mater.* **2018**, *7* (8), 1–14.

(18) Kim, J.; Campbell, A. S.; Wang, J. Wearable Non-Invasive Epidermal Glucose Sensors: A Review. *Talanta* **2018**, *177* (July 2017), 163–170.

(19) Nyein, H. Y. Y.; Tai, L. C.; Ngo, Q. P.; Chao, M.; Zhang, G. B.; Gao, W.; Bariya, M.; Bullock, J.; Kim, H.; Fahad, H. M.; Javey, A. A Wearable Microfluidic Sensing Patch for Dynamic Sweat Secretion Analysis. *ACS Sensors* **2018**, *3* (5), 944–952.

(20) Anastasova, S.; Crewther, B.; Bembnowicz, P.; Curto, V.; Ip, H. M.; Rosa, B.; Zhong-Yang, G. A Wearable Multisensing Patch for Continuous Sweat Monitoring. *Biosens. Bioelectron.* **2016**, *93* (September), 0–1.

(21) Walsh, D. I.; Kong, D. S.; Murthy, S. K.; Carr, P. A. Enabling Microfluidics: From Clean Rooms to Makerspaces. *Trends Biotechnol.* **2017**, *35* (5), 383–392.

(22) Yamada, K.; Henares, T. G.; Suzuki, K.; Citterio, D. Paper-Based Inkjet-Printed Microfluidic Analytical Devices. *Angew. Chemie - Int. Ed.* **2015**, *54* (18), 5294–5310.

(23) Bandodkar, A. J.; Wang, J. Non-Invasive Wearable Electrochemical Sensors: A Review. *Trends Biotechnol.* **2014**, *32* (7), 363–371.

(24) Wan, Y.; Su, Y.; Zhu, X.; Liu, G.; Fan, C. Development of Electrochemical Immunosensors towards Point of Care Diagnostics. *Biosens. Bioelectron.* **2013**, *47*, 1–11.

(25) Merian, T.; He, F.; Yan, H.; Chu, D.; Talbert, J. N.; Goddard, J. M.; Nugen, S. R. Development and Surface Characterization of an Electrowetting Valve for Capillary-Driven Microfluidics. *Colloids Surfaces A Physicochem. Eng. Asp.* **2012**, *414*, 251–258.

(26) He, F.; Nugen, S. R. Automating Fluid Delivery in a Capillary Microfluidic Device Using Low-Voltage Electrowetting Valves. *Microfluid. Nanofluidics* **2014**, *16* (5), 879–886.

(27) Koo, C. K. W.; He, F.; Nugen, S. R. An Inkjet-Printed Electrowetting Valve for Paper-Fluidic Sensors. *Analyst* **2013**, *138* (17), 4998–5004.

(28) Chen, J.; Zhou, Y.; Wang, D.; He, F.; Rotello, V. M.; Carter, K. R.; Watkins, J. J.; Nugen, S. R. UV-Nanoimprint Lithography as a Tool to Develop Flexible Microfluidic Devices for Electrochemical Detection. *Lab Chip* **2015**, *15*, 3086–3094.

(29) Ferrell, N.; Woodard, J.; Hansford, D. Fabrication of Polymer Microstructures for MEMS: Sacrificial Layer Micromolding and Patterned Substrate Micromolding. *Biomed. Microdevices* **2007**, *9* (6), 815–821.

(30) Secor, E. B.; Gao, T. Z.; Islam, A. E.; Rao, R.; Wallace, S. G.; Zhu, J.; Putz, K. W.; Maruyama, B.; Hersam, M. C. Enhanced Conductivity, Adhesion, and Environmental Stability of Printed Graphene Inks with Nitrocellulose. *Chem. Mater.* **2017**, *29* (5), 2332–2340.

(31) Liang, Y. T.; Hersam, M. C. Highly Concentrated Graphene Solutions via Polymer Enhanced Solvent Exfoliation and Iterative Solvent Exchange. *J. Am. Chem. Soc.* **2010**, *132* (50), 17661–17663.

(32) Prissanaroon-Ouajai, W.; James Pigram, P.; Sirivat, A. Simple Solid-State Ag/AgCl Reference Electrode and Its Integration with Conducting Polypyrrole Electrode for the Production of All-Solid-State pH Sensor. *KMUTNB Int. J. Appl. Sci. Technol.* **2016**, *9* (3), 1–9.

(33) Khullar, P.; Badilla, J. V.; Kelly, R. G. The Use of a Sintered Ag/AgCl Electrode

as Both Reference and Counter Electrode for Electrochemical Measurements in Thin Film Electrolytes. *ECS Electrochem. Lett.* **2015**, *4* (10), C31–C33.

(34) Bello, M. S.; Rezzonico, R.; Righetti, P. G. Use of Taylor-Aris Dispersion for Measurement of a Solute Diffusion Coefficient in Thin Capillaries Published by : American Association for the Advancement of Science Stable URL : http://www.jstor.org/stable/2885543. **2008**, *266* (5186), 773–776.

(35) Sung, J. H.; Shuler, M. L. Prevention of Air Bubble Formation in a Microfluidic Perfusion Cell Culture System Using a Microscale Bubble Trap. *Biomed. Microdevices* **2009**, *11* (4), 731–738.

(36) Nakayama, T.; Hiep, H. M.; Furui, S.; Yonezawa, Y.; Saito, M.; Takamura, Y.; Tamiya, E. An Optimal Design Method for Preventing Air Bubbles in High-Temperature Microfluidic Devices. *Anal. Bioanal. Chem.* **2010**, *396* (1), 457–464.

(37) Ricci, F.; Palleschi, G. Sensor and Biosensor Preparation, Optimisation and Applications of Prussian Blue Modified Electrodes. *Biosens. Bioelectron.* **2005**, *21* (3), 389–407.

BIBLIOGRAPHY

(1) Das, R.; Ghaffarzadeh, K.; He, X. Printed, Organic & Flexible Electronics Forecasts, Players & Opportunities 2017-2027. *IDTechEx Res.* **2017**, 1–329.

(2) Søndergaard, R. R.; Hösel, M.; Krebs, F. C. Roll-to-Roll Fabrication of Large Area Functional Organic Materials. *J. Polym. Sci. Part B Polym. Phys.* **2013**, *51* (1), 16–34.

(3) Schwartz, E. Roll to Roll Processing for Flexible Electronics. *Roll to Roll Process. Flex. Electron.* **2006**, 1–24.

(4) Koidis, C.; Logothetidis, S.; Ioakeimidis, A.; Laskarakis, A.; Kapnopoulos, C. Key Factors to Improve the Efficiency of Roll-to-Roll Printed Organic Photovoltaics. *Org. Electron. physics, Mater. Appl.* **2013**, *14* (7), 1744–1748.

(5) Ross, I. M. The Invention of the Transistor. *Proc. IEEE* **1998**, *86* (1), 7–28.

(6) Samsung. Samsung Starts Industry's First Mass Production of System-on-Chip with 10-Nanometer FinFET Technology. **2016**, Oct-16.

(7) Ferain, I.; Colinge, C. a.; Colinge, J.-P. Multigate Transistors as the Future of Classical Metal–oxide–semiconductor Field-Effect Transistors. *Nature* **2011**, *479* (7373), 310–316.

(8) Yan, H.; Chen, Z.; Zheng, Y.; Newman, C.; Quinn, J. R.; Dötz, F.; Kastler, M.; Facchetti, A. A High-Mobility Electron-Transporting Polymer for Printed Transistors. *Nature* **2009**, *457* (7230), 679–686.

(9) Beaulieu, M. R.; Baral, J. K.; Hendricks, N. R.; Tang, Y.; Briseno, A. L.; Watkins, J. J. Solution Processable High Dielectric Constant Nanocomposites Based on zro2 Nanoparticles for Flexible Organic Transistors. *ACS Appl. Mater. Interfaces* **2013**, *5* (24), 13096–13103.

(10) Wang, Z.; Cook, A. P.; Yang, X.; Liu, Z.; Yu, Q.; Chen, M. Y. Graphene-Based Flexible Field Effect Transistor with Inkjet Printed Silver Electrodes. **2013**, 635–637.

(11) Sirringhaus, H. 25th Anniversary Article: Organic Field-Effect Transistors: The Path beyond Amorphous Silicon. *Adv. Mater.* **2014**, *26* (9), 1319–1335.

(12) Gomes, H. L. Organic Field Effect Transistors. *Org. Print. Electron. - Fundam. Appl.* **2016**, No. i, 1–26.

(13) Gao, Y.; Shao, Y.; Yan, L.; Li, H.; Su, Y.; Meng, H.; Wang, X. Efficient Charge Injection in Organic Field-Effect Transistors Enabled by Low-Temperature Atomic Layer Deposition of Ultrathin VOxInterlayer. *Adv. Funct. Mater.* **2016**, *26*

(25), 4456–4463.

(14) Facchetti, A.; Yoon, M.-H.; Marks, T. J. Gate Dielectrics for Organic Field-Effect Transistors: New Opportunities for Organic Electronics. *Adv. Mater.* **2005**, *17* (14), 1705–1725.

(15) Campos, A.; Riera-Galindo, S.; Puigdollers, J.; Mas-Torrent, M. Reduction of Charge Traps and Stability Enhancement in Solution-Processed Organic Field-Effect Transistors Based on a Blended N-Type Semiconductor. *ACS Appl. Mater. Interfaces* **2018**, *10* (18), 15952–15961.

(16) Bao, Z.; Locklin, J. Organic Field Effect Transistors. **2007**, 1–33.

(17) Wu, Y.; Li, Y.; Ong, B. S.; Liu, P.; Gardner, S.; Chiang, B. High-Performance Organic Thin-Film Transistors with Solution-Printed Gold Contacts. *Adv. Mater.* **2005**, *17* (2), 184–187.

(18) Yi, S. M.; Jin, S. H.; Lee, J. D.; Chu, C. N. Fabrication of a High-Aspect-Ratio Stainless Steel Shadow Mask and Its Application to Pentacene Thin-Film Transistors. *J. Micromechanics Microengineering* **2005**, *15* (2), 263–269.

(19) Kim, S.; Sojoudi, H.; Zhao, H.; Mariappan, D.; McKinley, G. H.; Gleason, K. K.; Hart, A. J. Ultrathin High-Resolution Flexographic Printing Using Nanoporous Stamps. *Sci. Adv.* **2016**, *2*, 1–11.

(20) Traub, M. C.; Longsine, W.; Truskett, V. N. Advances in Nanoimprint Lithography. *Annu. Rev. Chem. Biomol. Eng.* **2016**, *7* (1), 583–604.

(21) Park, S. M.; Liang, X.; Harteneck, B. D.; Pick, T. E.; Hiroshiba, N.; Wu, Y.; Helms, B. A.; Olynick, D. L. Sub-10 Nm Nanofabrication via Nanoimprint Directed Self-Assembly of Block Copolymers. *ACS Nano* **2011**, *5* (11), 8523–8531.

(22) Chou, S. Y.; Krauss, P. R.; Renstrom, P. J. Imprint Lithography with 25 Nm Resolution. *Science (80-.).* **1996**, *272* (5258), 85–87.

(23) Tabatabai, A.; Fassler, A.; Usiak, C.; Majidi, C. Liquid-Phase Gallium − Indium Alloy Electronics with Microcontact Printing. **2013**.

(24) Blümel, A.; Klug, A.; Eder, S.; Scherf, U.; Moderegger, E.; List, E. J. W. Micromolding in Capillaries and Microtransfer Printing of Silver Nanoparticles as Soft-Lithographic Approach for the Fabrication of Source/drain Electrodes in Organic Field-Effect Transistors. *Org. Electron. physics, Mater. Appl.* **2007**, *8* (4), 389–395.

(25) Hwang, J. K.; Cho, S.; Dang, J. M.; Kwak, E. B.; Song, K.; Moon, J.; Sung, M. M. Direct Nanoprinting by Liquid-Bridge-Mediated Nanotransfer Moulding. *Nat. Nanotechnol.* **2010**, *5* (10), 742–748.

(26) Cho, B.; Park, K. S.; Baek, J.; Oh, H. S.; Koo Lee, Y. E.; Sung, M. M. Single-Crystal poly(3,4-Ethylenedioxythiophene) Nanowires with Ultrahigh Conductivity. *Nano Lett.* **2014**, *14* (6), 3321–3327.

(27) Kumar, S. Liquid Transfer in Printing Processes: Liquid Bridges with Moving Contact Lines. *Annu. Rev. Fluid Mech.* **2015**, *47* (1), 67–94.

(28) Weiss, N. O.; Zhou, H.; Liao, L.; Liu, Y.; Jiang, S.; Huang, Y.; Duan, X. Graphene: An Emerging Electronic Material. *Adv. Mater.* **2012**, *24* (43), 5782–5825.

(29) Zeng, M.; Xiao, Y.; Liu, J.; Lu, W.; Fu, L. Controllable Fabrication of Nanostructured Graphene Towards Electronics. *Adv. Electron. Mater.* **2016**, *2* (4), 1500456.

(30) Field-effect, O. S. C.; Liu, W.; Jackson, B. L.; Zhu, J.; Miao, C.; Park, Y.; Sun, K.; Woo, J.; Xie, Y. Large Scale Pattern Graphene Electrode for High Performance in Transparent. **2010**, *4* (7), 3927–3932.

(31) Dua, V.; Surwade, S. P.; Ammu, S.; Agnihotra, S. R.; Jain, S.; Roberts, K. E.; Park, S.; Ruoff, R. S.; Manohar, S. K. All-Organic Vapor Sensor Using Inkjet-Printed Reduced Graphene Oxide. *Angew. Chemie - Int. Ed.* **2010**, *49* (12), 2154–2157.

(32) Yi, M.; Shen, Z. A Review on Mechanical Exfoliation for the Scalable Production of Graphene. *J. Mater. Chem. A* **2015**, *3* (22), 11700–11715.

(33) Lin, J.; Peng, Z.; Liu, Y.; Ruiz-Zepeda, F.; Ye, R.; Samuel, E. L. G.; Yacaman, M. J.; Yakobson, B. I.; Tour, J. M. Laser-Induced Porous Graphene Films from Commercial Polymers. *Nat. Commun.* **2014**, *5* (5714), 1–8.

(34) Liang, Y. T.; Hersam, M. C. Highly Concentrated Graphene Solutions via Polymer Enhanced Solvent Exfoliation and Iterative Solvent Exchange. *J. Am. Chem. Soc.* **2010**, *132* (50), 17661–17663.

(35) Hyun, W. J.; Secor, E. B.; Rojas, G. A.; Hersam, M. C.; Francis, L. F.; Frisbie, C. D. All-Printed, Foldable Organic Thin-Film Transistors on Glassine Paper. *Adv. Mater.* **2015**, *27* (44), 7058–7064.

(36) Li, L.; Secor, E. B.; Chen, K. S.; Zhu, J.; Liu, X.; Gao, T. Z.; Seo, J. W. T.; Zhao, Y.; Hersam, M. C. High-Performance Solid-State Supercapacitors and Microsupercapacitors Derived from Printable Graphene Inks. *Adv. Energy Mater.* **2016**, *6* (20), 1–8.

(37) Gonzalez Arellano, D. L.; Lee, H.; Secor, E. B.; Burnett, E. K.; Hersam, M. C.; Watkins, J. J.; Briseno, A. L. Graphene Ink as a Conductive Templating Interlayer for Enhanced Charge Transport of C60-Based Devices. *ACS Appl. Mater.*

Interfaces **2016**, *8* (43), 29594–29599.

(38) Jakus, A. E.; Secor, E. B.; Rutz, A. L.; Jordan, S. W.; Hersam, M. C.; Shah, R. N. Three-Dimensional Printing of High-Content Graphene Sca Ff Olds for Electronic and Biomedical Applications. *ACS Nano* **2015**, *9* (4), 4636–4648.

(39) Secor, E. B.; Prabhumirashi, P. L.; Puntambekar, K.; Geier, M. L.; Hersam, M. C. Inkjet Printing of High Conductivity , Flexible Graphene Patterns. *J. Phys. Chem. Lett.* **2013**, *4*, 1347–1351.

(40) Secor, E. B.; Lim, S.; Zhang, H.; Frisbie, C. D.; Francis, L. F.; Hersam, M. C. Gravure Printing of Graphene for Large-Area Flexible Electronics. *Adv. Mater.* **2014**, *26*, 4533–4538.

(41) Hyun, W. J.; Secor, E. B.; Hersam, M. C.; Frisbie, C. D.; Francis, L. F. High-Resolution Patterning of Graphene by Screen Printing with a Silicon Stencil for Highly Flexible Printed Electronics. *Adv. Mater.* **2015**, *27* (1), 109–115.

(42) Song, D.; Mahajan, A.; Secor, E. B.; Hersam, M. C.; Francis, L. F.; Frisbie, C. D. High-Resolution Transfer Printing of Graphene Lines for Fully Printed, Flexible Electronics. *ACS Nano* **2017**, *11* (7), 7431.

(43) Kang, S. J.; Lee, G.-H.; Yu, Y.-J.; Zhao, Y.; Kim, B.; Watanabe, K.; Taniguchi, T.; Hone, J.; Kim, P.; Nuckolls, C. Organic Field Effect Transistors Based on Graphene and Hexagonal Boron Nitride Heterostructures. *Adv. Funct. Mater.* **2014**, *24*, 5157–5163.

(44) Pak, Y.; Jeong, H.; Lee, K. H.; Song, H.; Kwon, T.; Park, J.; Park, W.; Jeong, M. S.; Lee, T.; Seo, S.; Jung, G. Y. Large-Area Fabrication of Periodic Sub-15 Nm-Width Single-Layer Graphene Nanorings. *Adv. Mater.* **2013**, *25* (2), 199–204.

(45) Chao, W.; Keith, J. M.; Zengli, F.; Wen-Di, L.; Stephen, Y. C. Printing of Sub-20 Nm Wide Graphene Ribbon Arrays Using Nanoimprinted Graphite Stamps and Electrostatic Force Assisted Bonding. *Nanotechnology* **2011**, *22* (44), 445301.

(46) Liang, X.; Jung, Y. S.; Wu, S.; Ismach, A.; Olynick, D. L.; Cabrini, S.; Bokor, J. Formation of Bandgap and Subbands in Graphene Nanomeshes with Sub-10 Nm Ribbon Width Fabricated via Nanoimprint Lithography. *Nano Lett.* **2010**, *10* (7), 2454–2460.

(47) Zhang, J.; Hu, P.; Zhang, R.; Wang, X.; Yang, B.; Cao, W.; Li, Y.; He, X.; Wang, Z.; O'Neill, W. Soft-Lithographic Processed Soluble Micropatterns of Reduced Graphene Oxide for Wafer-Scale Thin Film Transistors and Gas Sensors. *J. Mater. Chem.* **2012**, *22*, 714.

(48) Liu, S.; Wang, W. M.; Briseno, A. L.; Mannsfeld, S. C. B.; Bao, Z. Controlled Deposition of Crystalline Organic Semiconductors for Field-Effect-Transistor

Applications. *Adv. Mater.* **2009**, *21* (12), 1217–1232.

(49) Jackman, R. J.; Duffy, D. C.; Ostuni, E.; Willmore, N. D.; Whitesides, G. M. Fabricating Large Arrays of Microwells with Arbitrary Dimensions and Filling Them Using Discontinuous Dewetting. *Anal. Chem.* **1998**, *70* (11), 2280–2287.

(50) Park, K. S.; Cho, B.; Baek, J.; Hwang, J. K.; Lee, H.; Sung, M. M. Single-Crystal Organic Nanowire Electronics by Direct Printing from Molecular Solutions. *Adv. Funct. Mater.* **2013**, *23* (38), 4776–4784.

(51) Lee, B. H.; Cho, Y. H.; Lee, H.; Lee, K. D.; Kim, S. H.; Sung, M. M. High-Resolution Patterning of Aluminum Thin Films with a Water-Mediated Transfer Process. *Adv. Mater.* **2007**, *19* (13), 1714–1718.

(52) *Table of Dielectric Constants of Pure Liquids*; 1994.

(53) Khattab, I. S.; Bandarkar, F.; Fakhree, M. A. A.; Jouyban, A. Density, Viscosity, and Surface Tension of Water+ethanol Mixtures from 293 to 323K. *Korean J. Chem. Eng.* **2012**, *29* (6), 812–817.

(54) Vargaftik, N. B.; Volkov, B. N.; Voljak, L. D. International Tables of the Surface Tension of Water. *J. Phys. Chem. Ref. Data* **1983**, *12* (3), 817–820.

(55) Chen, X.; Weibel, J. A.; Garimella, S. V. Water and Ethanol Droplet Wetting Transition during Evaporation on Omniphobic Surfaces. *Sci. Rep.* **2015**, *5* (October), 1–11.

(56) Tsetseris, L.; Pantelides, S. T. Oxygen and Water-Related Impurities in C60 Crystals: A Density-Functional Theory Study. *Phys. Rev. B - Condens. Matter Mater. Phys.* **2010**, *82* (4), 1–5.

(57) Capello, C.; Fischer, U.; Hungerbühler, K. What Is a Green Solvent? A Comprehensive Framework for the Environmental Assessment of Solvents. *Green Chem.* **2007**, *9* (9), 927.

(58) Yin, Z.; Huang, Y.; Bu, N.; Wang, X.; Xiong, Y. Inkjet Printing for Flexible Electronics: Materials, Processes and Equipments. *Chinese Sci. Bull.* **2010**, *55* (30), 3383–3407.

(59) Janssen, D.; De Palma, R.; Verlaak, S.; Heremans, P.; Dehaen, W. Static Solvent Contact Angle Measurements, Surface Free Energy and Wettability Determination of Various Self-Assembled Monolayers on Silicon Dioxide. *Thin Solid Films* **2006**, *515* (4), 1433–1438.

(60) Shafrin, E. G.; Zisman, W. A. Effect of Adsorbed Water on the Spreading of Organic Liquids on Soda-Lime Glass. *J. Am. Ceram. Soc.* **1967**, *50* (9), 478–484.

(61) van Osch, T. H. J.; Perelaer, J.; de Laat, A. W. M.; Schubert, U. S. Inkjet Printing

of Narrow Conductive Tracks on Untreated Polymeric Substrates. *Adv. Mater.* **2008**, *20* (2), 343–345.

(62) Secor, E. B.; Ahn, B. Y.; Gao, T. Z.; Lewis, J. A.; Hersam, M. C. Rapid and Versatile Photonic Annealing of Graphene Inks for Flexible Printed Electronics. *Adv. Mater.* **2015**, *27* (42), 6683–6688.

(63) Molinari, A. S.; Alves, H.; Chen, Z.; Facchetti, A.; Morpurgo, A. F. High Electron Mobility in Vacuum and Ambient for PDIF-CN $_2$ Single-Crystal Transistors. *J. Am. Chem. Soc.* **2009**, *131* (7), 2462–2463.

(64) Podzorov, V.; Sysoev, S. E.; Loginova, E.; Pudalov, V. M.; Gershenson, M. E. Single-Crystal Organic Field Effect Transistors with the Hole Mobility ~8 cm2/V S. *Appl. Phys. Lett.* **2003**, *83* (17), 3504.

(65) Briseno, A. L.; Tseng, R. J.; Ling, M. M.; Falcao, E. H. L.; Yang, Y.; Wudl, F.; Bao, Z. High-Performance Organic Single-Crystal Transistors on Flexible Substrates. *Adv. Mater.* **2006**, *18* (17), 2320–2324.

(66) Stassen, A. F.; De Boer, R. W. I.; Losad, N. N.; Morpurgo, A. F. Influence of the Gate Dielectric on the Mobility of Rubrene Single-Crystal Field-Effect Transistors. *Appl. Phys. Lett.* **2004**, *85* (17), 3899–3901.

(67) Kiron Prabha Rajeev, Charles Opoku, Vlad Stolojan, Marios Constantinou, M. S. Effect of Nanowire-Dielectric Interface on the Hysteresis of Solution Processed Silicon Nanowire FETs. *Nanosci. Nanoeng.* **2017**, *5* (2), 17–24.

(68) Chianese, F.; Chiarella, F.; Barra, M.; Carella, A.; Cassinese, A. Scanning Kelvin Probe Microscopy Investigation of the Contact Resistances and Charge Mobility in N-Type PDIF-CN2thin-Film Transistors. *Org. Electron. physics, Mater. Appl.* **2018**, *52* (August 2017), 206–212.

(69) Pathipati, S. R.; Pavlica, E.; Schlierf, A.; El Gemayel, M.; Samorì, P.; Palermo, V.; Bratina, G. Graphene-Induced Enhancement of N-Type Mobility in Perylenediimide Thin Films. *J. Phys. Chem. C* **2014**, *118* (43), 24819–24826.

(70) Secor, E. B.; Smith, J.; Marks, T. J.; Hersam, M. C. High-Performance Inkjet-Printed Indium-Gallium-Zinc-Oxide Transistors Enabled by Embedded, Chemically Stable Graphene Electrodes. *ACS Appl. Mater. Interfaces* **2016**, *8* (27), 17428–17434.

(71) Acevedo-Cartagena, D. E.; Zhu, J.; Trabanino, E.; Pentzer, E.; Emrick, T.; Nonnenmann, S. S.; Briseno, A. L.; Hayward, R. C. Selective Nucleation of poly(3-Hexyl Thiophene) Nanofibers on Multilayer Graphene Substrates. *ACS Macro Lett.* **2015**, *4* (5), 483–487.

(72) Koh, A.; Kang, D.; Xue, Y.; Lee, S.; Pielak, R. M.; Kim, J.; Hwang, T.; Min, S.;

Banks, A.; Bastien, P.; Manco, M. C.; Wang, L.; Ammann, K. R.; Jang, K.-I.; Won, P.; Han, S.; Ghaffari, R.; Paik, U.; Slepian, M. J.; Balooch, G.; Huang, Y.; Rogers, J. A. A Soft, Wearable Microfluidic Device for the Capture, Storage, and Colorimetric Sensing of Sweat. *Sci. Transl. Med.* **2016**, *8* (366), 366ra165-366ra165.

(73) Elvira, K. S.; i Solvas, X. C.; Wootton, R. C. R.; deMello, A. J. The Past, Present and Potential for Microfluidic Reactor Technology in Chemical Synthesis. *Nat. Chem.* **2013**, *5* (11), 905–915.

(74) Guha, S.; Perry, S. L.; Pawate, A. S.; Kenis, P. J. A. Fabrication of X-Ray Compatible Microfluidic Platforms for Protein Crystallization. *Sensors Actuators, B Chem.* **2012**, *174*, 1–9.

(75) Leyrat, A. A.; Pirone, D. M.; Chen, C. S.; Quake, S. R. Versatile , Fully Automated , Microfluidic Cell. *Anal. Chem.* **2007**, *79* (22), 8557–8563.

(76) Stone, H. A.; Stroock, A. D.; Ajdari, A. Engineering Flows in Small Devices. *Annu. Rev. Fluid Mech.* **2004**, *36* (1), 381–411.

(77) Byrnes, S.; Thiessen, G.; Fu, E. Progress in the Development of Paper-Based Diagnostics for Low-Resource Point-of-Care Settings. *Bioanalysis* **2013**, *5* (22), 2821–2836.

(78) Oh, K. W.; Ahn, C. H. A Review of Microvalves. *J. Micromechanics Microengineering* **2006**, *16* (5), R13–R39.

(79) Zhang, C.; Xing, D.; Li, Y. Micropumps, Microvalves, and Micromixers within PCR Microfluidic Chips: Advances and Trends. *Biotechnol. Adv.* **2007**, *25* (5), 483–514.

(80) Tice, J. D.; Desai, a V; Bassett, T. a; Apblett, C. a; Kenis, P. J. a. Electrostatic Microvalves for Integrated Microchemical Systems. *uTAS* **2011**, 1813–1815.

(81) Khoshmanesh, K.; Almansouri, A.; Albloushi, H.; Yi, P.; Soffe, R.; Kalantar-zadeh, K. A Multi-Functional Bubble-Based Microfluidic System. *Sci. Rep.* **2015**, *5*, 9942.

(82) Cho, H.; Kim, H. Y.; Kang, J. Y.; Kim, T. S. How the Capillary Burst Microvalve Works. *J. Colloid Interface Sci.* **2007**, *306* (2), 379–385.

(83) Toley, B. J.; McKenzie, B.; Liang, T.; Buser, J. R.; Yager, P.; Fu, E. Tunable-Delay Shunts for Paper Micro Fl Uidic Devices. *Anal. Chem.* **2013**, *85* (23), 11545–11552.

(84) Thorsen, T.; Maerkl, S. J.; Quake, S. R. Microfluidic Large-Scale Integration. *Science (80-.).* **2002**, *298* (5593), 580–584.

(85) Merian, T.; He, F.; Yan, H.; Chu, D.; Talbert, J. N.; Goddard, J. M.; Nugen, S. R. Development and Surface Characterization of an Electrowetting Valve for Capillary-Driven Microfluidics. *Colloids Surfaces A Physicochem. Eng. Asp.* **2012**, *414*, 251–258.

(86) Erickson, D.; Li, D. Integrated Microfluidic Devices. *Anal. Chim. Acta* **2004**, *507* (1), 11–26.

(87) Whitesides, G. M. The Origins and the Future of Microfluidics. *Nature* **2006**, *442* (7101), 368–373.

(88) Zhao, B.; Moore, J. S.; Beebe, D. J. Surface-Directed Liquid Flow inside Microchannels. *Science* **2001**, *291* (5506), 1023–1026.

(89) Hasselbrink, E. F.; Shepodd, T. J.; Rehm, J. E. High-Pressure Microfluidic Control in Lab-on-a-Chip Devices Using Mobile Polymer Monoliths. *Anal. Chem.* **2002**, *74* (19), 4913–4918.

(90) Unger, M. A. Monolithic Microfabricated Valves and Pumps by Multilayer Soft Lithography. *Science (80-.).* **2000**, *288* (5463), 113–116.

(91) Desai, A. V.; Tice, J. D.; Apblett, C. a.; Kenis, P. J. a. Design Considerations for Electrostatic Microvalves with Applications in Poly(dimethylsiloxane)-Based Microfluidics. *Lab Chip* **2012**, *12* (6), 1078.

(92) MacH, P.; Krupenkin, T.; Yang, S.; Rogers, J. A. Dynamic Tuning of Optical Waveguides with Electrowetting Pumps and Recirculating Fluid Channels. *Appl. Phys. Lett.* **2002**, *81* (2), 202–204.

(93) Moon, I.; Kim, J. Using EWOD (Electrowetting-on-Dielectric) Actuation in a Micro Conveyor System. *Sensors Actuators, A Phys.* **2006**, *130–131* (SPEC. ISS.), 537–544.

(94) Hendriks, B. H. W.; Kuiper, S.; Van As, M. A. J.; Renders, C. A.; Tukker, T. W. Electrowetting-Based Variable-Focus Lens for Miniature Systems. *Opt. Rev.* **2005**, *12* (3), 255–259.

(95) Di, Q. T.; Zhang, H.; Liang, X. L.; Li, A. D.; Xiao, C. S.; Wu, D.; Xu, Q. Y. Electrowetting Display Pixels Fabricated by Nanoimprint Lithography. **2015**, No. Asei, 495–501.

(96) Shamai, R.; Andelman, D.; Berge, B.; Hayes, R. Water, Electricity, and Between… On Electrowetting and Its Applications. *Soft Matter* **2008**, *4* (1), 38–45.

(97) Chen, J.; Zhou, Y.; Wang, D.; He, F.; Rotello, V. M.; Carter, K. R.; Watkins, J. J.; Nugen, S. R. UV-Nanoimprint Lithography as a Tool to Develop Flexible Microfluidic Devices for Electrochemical Detection. *Lab Chip* **2015**, *15*, 3086–

3094.

(98) Koo, C. K. W.; He, F.; Nugen, S. R. An Inkjet-Printed Electrowetting Valve for Paper-Fluidic Sensors. *Analyst* **2013**, *138* (17), 4998–5004.

(99) He, F.; Grimes, J.; Alcaine, S. D.; Nugen, S. R. A Hybrid Paper and Microfluidic Chip with Electrowetting Valves and Colorimetric Detection. *Analyst* **2014**, *139* (12), 3002–3008.

(100) Jadoon, S.; Karim, S.; Akram, M. R.; Kalsoom Khan, A.; Zia, M. A.; Siddiqi, A. R.; Murtaza, G.; Jadoon, S.; Karim, S.; Akram, M. R.; Kalsoom Khan, A.; Zia, M. A.; Siddiqi, A. R.; Murtaza, G. Recent Developments in Sweat Analysis and Its Applications. *Int. J. Anal. Chem.* **2015**, *2015*, 1–7.

(101) Bandodkar, A. J.; Wang, J. Non-Invasive Wearable Electrochemical Sensors: A Review. *Trends Biotechnol.* **2014**, *32* (7), 363–371.

(102) Koh, A.; Kang, D.; Xue, Y.; Lee, S.; Pielak, R. M.; Kim, J.; Hwang, T.; Min, S.; Banks, A.; Manco, M. C.; Wang, L.; Ammann, K. R.; Jang, K.; Han, S.; Ghaffari, R.; Paik, U.; Slepian, M. J.; Huang, Y.; Rogers, J. A. A Soft, Wearable Microfluidic Device for the Capture, Storage, and Colorimetric Sensing of Sweat. *Sci Transl Med* **2017**, *8* (366), 1–14.

(103) Gao, W.; Emaminejad, S.; Nyein, H. Y. Y.; Challa, S.; Chen, K.; Peck, A.; Fahad, H. M.; Ota, H.; Shiraki, H.; Kiriya, D.; Lien, D.-H.; Brooks, G. A.; Davis, R. W.; Javey, A. Fully Integrated Wearable Sensor Arrays for Multiplexed in Situ Perspiration Analysis. *Nature* **2016**, *529* (7587), 509–514.

(104) Munje, R. D.; Muthukumar, S.; Panneer Selvam, A.; Prasad, S. Flexible Nanoporous Tunable Electrical Double Layer Biosensors for Sweat Diagnostics. *Sci. Rep.* **2015**, *5*, 14586.

(105) Choi, J.; Kang, D.; Han, S.; Kim, S. B.; Rogers, J. A. Thin, Soft, Skin-Mounted Microfluidic Networks with Capillary Bursting Valves for Chrono-Sampling of Sweat. *Adv. Healthc. Mater.* **2017**, *6* (5), 1–10.

(106) Kim, S. B.; Zhang, Y.; Won, S. M.; Bandodkar, A. J.; Sekine, Y.; Xue, Y.; Koo, J.; Harshman, S. W.; Martin, J. A.; Park, J. M.; Ray, T. R.; Crawford, K. E.; Lee, K. T.; Choi, J.; Pitsch, R. L.; Grigsby, C. C.; Strang, A. J.; Chen, Y. Y.; Xu, S.; Kim, J.; Koh, A.; Ha, J. S.; Huang, Y.; Kim, S. W.; Rogers, J. A. Super-Absorbent Polymer Valves and Colorimetric Chemistries for Time-Sequenced Discrete Sampling and Chloride Analysis of Sweat via Skin-Mounted Soft Microfluidics. *Small* **2018**, *14* (12), 1–11.

(107) He, F.; Nugen, S. R. Automating Fluid Delivery in a Capillary Microfluidic Device Using Low-Voltage Electrowetting Valves. *Microfluid. Nanofluidics* **2014**, *16* (5), 879–886.

(108) Brueck, A.; Iftekhar, T.; Stannard, A.; Yelamarthi, K.; Kaya, T. A Real-Time Wireless Sweat Rate Measurement System for Physical Activity Monitoring. *Sensors* **2018**, *18* (2), 533.

(109) Chandekar, A.; Sengupta, S. K.; Whitten, J. E. Thermal Stability of Thiol and Silane Monolayers : A Comparative Study. *Appl. Surf. Sci.* **2010**, *256*, 2742–2749.

(110) Love, J. C.; Estroff, L. A.; Kriebel, J. K.; Nuzzo, R. G.; Whitesides, G. M. *Self-Assembled Monolayers of Thiolates on Metals as a Form of Nanotechnology*; 2005; Vol. 105.

(111) Rossmeisl, J.; Logadottir, A.; Nørskov, J. K. Electrolysis of Water on (Oxidized) Metal Surfaces. *Chem. Phys.* **2005**, *319*, 178–184.

(112) Gao, B.; Elbaz, A.; He, Z.; Xie, Z.; Xu, H.; Liu, S.; Su, E.; Liu, H.; Gu, Z. Bioinspired Kirigami Fish-Based Highly Stretched Wearable Biosensor for Human Biochemical–Physiological Hybrid Monitoring. *Adv. Mater. Technol.* **2018**, *3* (4), 1–8.

(113) Martín, A.; Kim, J.; Kurniawan, J. F.; Sempionatto, J. R.; Moreto, J. R.; Tang, G.; Campbell, A. S.; Shin, A.; Lee, M. Y.; Liu, X.; Wang, J. Epidermal Microfluidic Electrochemical Detection System: Enhanced Sweat Sampling and Metabolite Detection. *ACS Sensors* **2017**, *2* (12), 1860–1868.

(114) Heikenfeld, J. Bioanalytical Devices: Technological Leap for Sweat Sensing. *Nature* **2016**, *529* (7587), 475–476.

(115) Heikenfeld, J. Non-Invasive Analyte Access and Sensing through Eccrine Sweat: Challenges and Outlook circa 2016. *Electroanalysis* **2016**, n/a-n/a.

(116) Sim, J. K.; Yoon, S.; Cho, Y. H. Wearable Sweat Rate Sensors for Human Thermal Comfort Monitoring. *Sci. Rep.* **2018**, *8* (1), 1–11.

(117) Oh, S. Y.; Hong, S. Y.; Jeong, Y. R.; Yun, J.; Park, H.; Jin, S. W.; Lee, G.; Oh, J. H.; Lee, H.; Lee, S. S.; Ha, J. S. Skin-Attachable, Stretchable Electrochemical Sweat Sensor for Glucose and pH Detection. *ACS Appl. Mater. Interfaces* **2018**, *10* (16), 13729–13740.

(118) Coyle, S.; Morris, D.; Lau, K. T.; Diamond, D.; Di Francesco, F.; Taccini, N.; Trivella, M. G.; Costanzo, D.; Salvo, P.; Porchet, J. A.; Luprano, J. Textile Sensors to Measure Sweat pH and Sweat-Rate during Exercise. *Pervasive Comput. Technol. Heal. 2009. PervasiveHealth 2009. 3rd Int. Conf.* **2009**, 4–9.

(119) Rose, D. P.; Ratterman, M. E.; Griffin, D. K.; Hou, L.; Kelley-Loughnane, N.; Naik, R. R.; Hagen, J. A.; Papautsky, I.; Heikenfeld, J. C. Adhesive RFID Sensor Patch for Monitoring of Sweat Electrolytes. *IEEE Trans. Biomed. Eng.* **2015**, *62* (6), 1457–1465.

(120) Emaminejad, S.; Gao, W.; Wu, E.; Davies, Z. A.; Yin Yin Nyein, H.; Challa, S.; Ryan, S. P.; Fahad, H. M.; Chen, K.; Shahpar, Z.; Talebi, S.; Milla, C.; Javey, A.; Davis, R. W. Autonomous Sweat Extraction and Analysis Applied to Cystic Fibrosis and Glucose Monitoring Using a Fully Integrated Wearable Platform. *Proc. Natl. Acad. Sci.* **2017**, *114* (18), 4625–4630.

(121) Twine, N. B.; Norton, R. M.; Brothers, M. C.; Hauke, A.; Gomez, E. F.; Heikenfeld, J. Open Nanofluidic Films with Rapid Transport and No Analyte Exchange for Ultra-Low Sample Volumes. *Lab Chip* **2018**.

(122) Kaushik, A.; Vasudev, A.; Arya, S. K.; Pasha, S. K.; Bhansali, S. Recent Advances in Cortisol Sensing Technologies for Point-of-Care Application. *Biosens. Bioelectron.* **2014**, *53* (October), 499–512.

(123) Singh, A.; Kaushik, A.; Kumar, R.; Nair, M.; Bhansali, S. Electrochemical Sensing of Cortisol: A Recent Update. *Appl. Biochem. Biotechnol.* **2014**, *174* (3), 1115–1126.

(124) Kim, K. S.; Lim, S. R.; Kim, S. E.; Lee, J. Y.; Chung, C. H.; Choe, W. S.; Yoo, P. J. Highly Sensitive and Selective Electrochemical Cortisol Sensor Using Bifunctional Protein Interlayer-Modified Graphene Electrodes. *Sensors Actuators, B Chem.* **2017**, *242*, 1121–1128.

(125) Lee, H.; Song, C.; Hong, Y. S.; Kim, M. S.; Cho, H. R.; Kang, T.; Shin, K.; Choi, S. H.; Hyeon, T.; Kim, D.-H. Wearable/disposable Sweat-Based Glucose Monitoring Device with Multistage Transdermal Drug Delivery Module. *Sci. Adv.* **2017**, *3* (3), e1601314.

(126) Lee, H.; Hong, Y. J.; Baik, S.; Hyeon, T.; Kim, D. H. Enzyme-Based Glucose Sensor: From Invasive to Wearable Device. *Adv. Healthc. Mater.* **2018**, *7* (8), 1–14.

(127) Kim, J.; Campbell, A. S.; Wang, J. Wearable Non-Invasive Epidermal Glucose Sensors: A Review. *Talanta* **2018**, *177* (July 2017), 163–170.

(128) Nyein, H. Y. Y.; Tai, L. C.; Ngo, Q. P.; Chao, M.; Zhang, G. B.; Gao, W.; Bariya, M.; Bullock, J.; Kim, H.; Fahad, H. M.; Javey, A. A Wearable Microfluidic Sensing Patch for Dynamic Sweat Secretion Analysis. *ACS Sensors* **2018**, *3* (5), 944–952.

(129) Anastasova, S.; Crewther, B.; Bembnowicz, P.; Curto, V.; Ip, H. M.; Rosa, B.; Zhong-Yang, G. A Wearable Multisensing Patch for Continuous Sweat Monitoring. *Biosens. Bioelectron.* **2016**, *93* (September), 0–1.

(130) Walsh, D. I.; Kong, D. S.; Murthy, S. K.; Carr, P. A. Enabling Microfluidics: From Clean Rooms to Makerspaces. *Trends Biotechnol.* **2017**, *35* (5), 383–392.

(131) Yamada, K.; Henares, T. G.; Suzuki, K.; Citterio, D. Paper-Based Inkjet-Printed Microfluidic Analytical Devices. *Angew. Chemie - Int. Ed.* **2015**, *54* (18), 5294–5310.

(132) Wan, Y.; Su, Y.; Zhu, X.; Liu, G.; Fan, C. Development of Electrochemical Immunosensors towards Point of Care Diagnostics. *Biosens. Bioelectron.* **2013**, *47*, 1–11.

(133) Ferrell, N.; Woodard, J.; Hansford, D. Fabrication of Polymer Microstructures for MEMS: Sacrificial Layer Micromolding and Patterned Substrate Micromolding. *Biomed. Microdevices* **2007**, *9* (6), 815–821.

(134) Secor, E. B.; Gao, T. Z.; Islam, A. E.; Rao, R.; Wallace, S. G.; Zhu, J.; Putz, K. W.; Maruyama, B.; Hersam, M. C. Enhanced Conductivity, Adhesion, and Environmental Stability of Printed Graphene Inks with Nitrocellulose. *Chem. Mater.* **2017**, *29* (5), 2332–2340.

(135) Prissanaroon-Ouajai, W.; James Pigram, P.; Sirivat, A. Simple Solid-State Ag/AgCl Reference Electrode and Its Integration with Conducting Polypyrrole Electrode for the Production of All-Solid-State pH Sensor. *KMUTNB Int. J. Appl. Sci. Technol.* **2016**, *9* (3), 1–9.

(136) Khullar, P.; Badilla, J. V.; Kelly, R. G. The Use of a Sintered Ag/AgCl Electrode as Both Reference and Counter Electrode for Electrochemical Measurements in Thin Film Electrolytes. *ECS Electrochem. Lett.* **2015**, *4* (10), C31–C33.

(137) Bello, M. S.; Rezzonico, R.; Righetti, P. G. Use of Taylor-Aris Dispersion for Measurement of a Solute Diffusion Coefficient in Thin Capillaries Published by : American Association for the Advancement of Science Stable URL : http://www.jstor.org/stable/2885543. **2008**, *266* (5186), 773–776.

(138) Sung, J. H.; Shuler, M. L. Prevention of Air Bubble Formation in a Microfluidic Perfusion Cell Culture System Using a Microscale Bubble Trap. *Biomed. Microdevices* **2009**, *11* (4), 731–738.

(139) Nakayama, T.; Hiep, H. M.; Furui, S.; Yonezawa, Y.; Saito, M.; Takamura, Y.; Tamiya, E. An Optimal Design Method for Preventing Air Bubbles in High-Temperature Microfluidic Devices. *Anal. Bioanal. Chem.* **2010**, *396* (1), 457–464.

(140) Ricci, F.; Palleschi, G. Sensor and Biosensor Preparation, Optimisation and Applications of Prussian Blue Modified Electrodes. *Biosens. Bioelectron.* **2005**, *21* (3), 389–407.